Reactive oxygen species in Alzheimer's disease: studies of amyloid beta-copper and apolipoprotein E

A thesis submitted for the degree of

Doctor of Philosopy

By

Paul Girvan

Department of Chemistry,
Imperial College London

September 2018

Acknowledgements

I would like to thank my supervisors for giving me the opportunity for this PhD, for their time, support and guidance given thought out. I would like to especially thank Dr Liming Ying, whose training has helped shape how I view the molecular world.

I would also like to thank my family. To my mother, for her support; my father, for teaching me to pursue my interests; and my aunt, for her endless cups of tea -without which this thesis would remain unfinished.

Finally, thank you to all my friends and colleagues who have assisted me with my research, and helped make this experience as enjoyable as possible. With a special thanks to David, Raquel and Yasin, for their meticulous proofreading of this document.

Declaration

I declare that this thesis, submitted to fufill the requirements for the degree of Doctor of Philosopy at Imperial College London, titled "Reactive oxygen species in Alzheimer's disease: studies of amyloid beta-copper and apolipoprotein E" represents my own work, unless otherwise stated.

Paul Girvan
September 2018

Copyright Declaration

The copyright of this thesis rests with the author and is made available under a Creative Commons Attribution Non-Commercial No Derivatives licence. Researchers are free to copy, distribute or transmit the thesis on the condition that they attribute it, that they do not use it for commercial purposes and that they do not alter, transform or build upon it. For any reuse or redistribution, researchers must make clear to others the licence terms of this work.

Abstract

There are many hypotheses for the cause of Alzheimer's disease. This thesis explores one such hypothesis, the metals hypothesis, and attempts to do so from a kinetic point of view. The metals hypothesis posits that Amyloid-β (Aβ) can bind intrinsic metals within the brain, causing increased Aβ oligomerisation, and (in the case of binding copper or iron) is able to be a source of reactive oxygen species (ROS), via redox cycling of the Aβ-metal complex.

In the first part of this thesis I draw comparisons between wild-type Aβ and disease prone mutants, providing evidence that the disease mutants have ∼50 % higher copper assisted dimerisation rate constants, compared to the wild-type Aβ. In doing so I try to highlight the beneficial insights that a kinetic understand can afford. I explore the kinetic mechanism of AβCu redox cycling, attempting to address on what timescale the process occurs. I show that the reduction step is fairly rapid (tens of millisecond timescale), and follows a conformational selection mechanism. But that redox cycling is ultimately limited by the relatively slow oxidation.

Looking further at the role of AβCu in ROS generation, I shown that AβCu is almost twice as efficient at causing lipid membrane peroxidation than uncomplexed Cu. This increased efficiency is surprising considering uncomplexed Cu can generate ROS much more rapidly than AβCu.

Finally, this thesis moves on to look at apolipoprotein E (apoE), which is the biggest genetic risk factor for developing late onset AD. I explore the role of apoE as a lipoprotein and show that it displays antioxidant effects, protecting against lipid peroxidation.

Contents

Contents **5**

List of Figures **9**

Glossary **11**

1 Introduction **15**
1.1 Alzheimer's Disease . . . 15
1.1.1 Hypotheses for the disease . . . 15
1.2 Amyloid-β . . . 19
1.2.1 Production of Aβ . . . 19
1.2.2 Clearance of Aβ . . . 21
1.3 Risk Factors . . . 21
1.3.1 Familial Alzheimer's disease . . . 22
1.3.2 Apolipoprotein E . . . 23
1.4 The Drugs Don't Work . . . 23
1.5 Thesis Outline . . . 25
1.6 Publications From This Work . . . 25

2 Methods and Materials **27**
2.1 Fluorescence - an introduction . . . 27
2.2 Experimental Methods . . . 28
2.2.1 Fluorometry . . . 28
2.2.2 Ultraviolet-Visible Spectroscopy . . . 29
2.2.3 Stopped Flow . . . 30
2.2.4 Confocal Microscopy . . . 31
2.2.5 Circular Dichroism . . . 36
2.2.6 Gel Imaging . . . 37
2.3 Materials . . . 38

2.3.1 Amyloid beta peptides . . . 38
2.3.2 Buffers . . . 39
2.3.3 Lipids . . . 39
2.3.4 Other reagents . . . 39

3 Interactions of Aβ & Metal Ions 41
3.1 A brief introduction . . . 41
3.1.1 Metals and aggregation . . . 41
3.1.2 Coordination of copper to Aβ . . . 43
3.1.3 From where does the copper come? . . . 43
3.2 Activation energy of interconversion . . . 46
3.3 $A\beta Cu^{2+}$ kinetics for Familial Alzheimer's disease mutations . . . 51
3.4 Summary . . . 55

4 Redox of the Amyloid-β Copper Complex 59
4.1 Reactive oxygen species generation of the AβCu complex . . . 59
4.2 Measuring redox by directly monitoring the oxidation state of the metal ion . . . 61
4.3 Titration of ascorbate to $A\beta Cu^{2+}$ complex . . . 62
4.3.1 Collisional quenching of the dye at high concentrations of ascorbate . . . 63
4.4 Reduction kinetics of $A\beta Cu^{2+}$ by ascorbate . . . 65
4.4.1 Comparison between HEPES and MOPS buffers . . . 66
4.4.2 Reduction goes via Component I . . . 67
4.5 Comparisons between the wild-type and mutant Aβ peptides . . . 68
4.5.1 The murine Aβ peptide . . . 68
4.5.2 Comparisons with H6R Aβ peptide . . . 70
4.6 The kinetic mechanism of reduction . . . 71
4.7 Oxidation of $A\beta Cu^{+}$ . . . 74
4.7.1 'In situ' produced $A\beta Cu^{+}$ . . . 76
4.8 Summary . . . 78

5 Lipid Peroxidation by the AβCu Complex 81
5.1 Methods for measuring ROS . . . 81
5.2 Measuring lipid peroxidation using BODIPY™581/591 C11 . . . 84
5.2.1 GM1 micellar system . . . 84
5.2.2 DLPC vesicle system . . . 88
5.3 Fluorescent correlation spectroscopy of Aβ40 binding to vesicles . . . 89

5.4 Summary 93

6 Apolipoprotein E -expression, purification and labelling 95
6.1 A Brief Overview of Apolipoprotein E 95
6.1.1 Structure and Function 95
6.1.2 Apoliporotein E & Amyloid-β Interactions 97
6.1.3 Apolipoprotein E: if not Aβ, then what? 98
6.2 Purification strategies - a history 98
6.3 Current purification strategy 99
6.3.1 Recombinant production of 3C protease 102
6.4 Fluorescent labelling strategies 103
6.4.1 Intrinsic fluorophores 103
6.4.2 Covalent Small molecule fluorophores 104
6.4.3 Sortase A labelling 105
6.5 Fluorescent labelling of the N-terminus of apolipoprotein E 106
6.5.1 Recombinant production of Sortase $A_{\Delta 59}$ 106
6.5.2 Labelling trial with fluorescein 108
6.5.3 Purification of the labelled apoE 109
6.5.4 Labelling with Atto-488 111
6.5.5 Improving the labelling efficiency 111
6.6 Summary 116

7 Apolipoprotein E Lipid Interactions 117
7.1 Circular dichroism 117
7.2 FCS of apoE with lipids 119
7.3 Lipid peroxidation of apoE-lipid particles 124
7.4 Summary 129

8 Conclusions & Further Work 131

Bibliography 135

Appendices 147

A Copyright Permission Documents 149

Contents

List of Figures

1.1 Amyloid cascade hypothesis schematic 16
1.2 Metals hypothesis schematic 18
1.3 Tau hypothesis 19
1.4 Representation of the transmembrane APP 20
1.5 Genetic risk factos in Alzheimer's disease 22

2.1 Jablonski diagram 27
2.2 Stopped flow schematic 30
2.3 Confocal schematic 32
2.4 Confocal microscope schematic 33
2.5 Example FCS trace 34

3.1 The fibrilisation of Aβ 42
3.2 AβCu^{2+} coordination 44
3.3 Metal release within a synapse 45
3.4 Interconversion of AβCu^{2+} probed by double mixing 46
3.5 Murine AβCu^{2+} coordination 48
3.6 Interconversion of murine AβCu^{2+} probed by double mixing 49
3.7 Thermodynamics of AβCu^{2+} interconversion 50
3.8 Familial Alzheimer's disease mutations within the amyloid precursor protein 52
3.9 H6RAβCu^{2+} coordination 53
3.10 Association and dissociation rate of Cu^{2+} with Aβ bearing the H6R or D7N familial Alzheimer's disease mutation 54
3.11 Ternary complex kinetics of FAD Aβ 55

4.1 Redox cycling of AβCu 60
4.2 Coordination of the AβCu^{+} complex 60

4.3 Fluorescence of AβCu^{2+} is recovered upon reduction 63
4.4 Quenching of labelled Aβ by ascorbate 64
4.5 Kinetics of AβCu^{2+} reduction by ascorbate 65
4.6 Reduction of AβCu^{2+} by ascorbate in MOPS buffer 67
4.7 Reduction of AβCu^{2+} probed by double mixing stopped flow 68
4.8 Kinetics of murine AβCu^{2+} reduction 69
4.9 Kinetics of H6RAβCu^{2+} reduction 70
4.10 Proposed 'redox active' AβCu coordinations 72
4.11 Kinetic mechanism of AβCu^{2+} reduction 73
4.12 UV-Vis spectra of [Cu(MeCN)$_4$]BF$_4$ in MQ 74
4.13 UV-Vis spectra of [Cu(MeCN)$_4$]BF$_4$ in buffer 75
4.14 Kinetics of Aβ [Cu(MeCN)$_4$]BF$_4$ association 76
4.15 'In situ' formation of AβCu^{+} by double mixing 77
4.16 Kinetics of AβCu^{+} oxidation 77

5.1 3-CCA and its major hydroxylation product 7-OHC 82
5.2 C$_{11}$-BODIPY$^{581/591}$ peroxidation probe 83
5.3 Peroxidation of GM1 micelles by AβCu^{2+} 85
5.4 Peroxidation of GM1 micelles by Cu^{2+} 85
5.5 Auto-peroxidation of GM1 micells is low and is inhibited in the presence of EDTA 86
5.6 Peroxidation of GM1 micelles is more efficient by AβCu^{2+} than Cu^{2+} alone 87
5.7 Peroxidation of DLPC SUVs by AβCu^{2+} 88
5.8 FCS of labelled Aβ monomers 89
5.9 FCS of DLPC SUVs 90
5.10 FCS of labelled Aβ binding to DLPC SUVs 91
5.11 FCS of labelled Aβ binding to mixed DLPC/GM1 SUVs 92
5.12 FCS of Aβ binding to GM1 micelles 93

6.1 Schematic of apoE 96
6.2 Purification of trx-apoE fusion protein by Ni^{2+} affinity column . . . 101
6.3 Purification of apoE protein by 'inverse' Ni^{2+} affinity column 102
6.4 Schematic of labelling via sortase enzyme 106
6.5 Purification of sortase A (SrtA) 107
6.6 Labelling of apoE by sortase 108
6.7 Purification of labelled apoE 109

6.8 Optimised purification of labelled apoE 111
6.9 Making apoE a better nucleophile 113
6.10 Depsispeptide substrate 115
6.11 Making the side product a worse nucleophile 115

7.1 Circular dichroism of apoE 118
7.2 apoE refolds following thermal denaturation and cooling 118
7.3 Thermal denaturation of apoE 120
7.4 apoE4 dissociation upon dilution 120
7.5 apoE4 binds to GM1 micelles 121
7.6 apoE4 binds to DMPC SUVs 123
7.7 apoE3 binds to DMPC SUVs 124
7.8 Peroxidation of DMPC:apoE particles 126
7.9 Peroxidation of DMPC:apoE particles by AβCu 126
7.10 apoE reduces apparent rate of lipid peroxidation in an isoform dependant manner 127
7.11 apoE reduces hydroxyl radical production in solution 128

List of Figures

Acronyms

3-CCA	coumarin-3-carboxylic acid.
7-OHC	7-hydroxycoumarin.
Aβ	Amyloid-β.
AICD	APP intracellular domain.
apoE	apolipoprotein E.
APP	amyloid precursor protein.
asc	ascorbate.
CD	circular dichroism.
FAD	familial Alzheimer's disease.
FCS	fluorescence correlation spectroscopy.
hAβ	human Aβ.
HT	high tension.
LRP	lipoprotein receptor-related protein.
mAβ	murine Aβ.
NFT	neurofibrilary tangles.
PHF	paired helical filaments.
PMT	photon multiplier tube.

ROS	reactive oxygen species.
SrtA	sortase A.
SUV	small unilamellar vesicles.
UV-Vis	ultraviolet-visible.
wt-Aβ	wild-type Aβ.

Chapter 1

Introduction

1.1 Alzheimer's Disease

In 1907 the German psychiatrist Alois Alzheimer published a paper describing a patient who had a peculiar disease of the cerebral cortex, a disease which would later be coined Alzheimer's disease.[1,2] Over a century later, what initially was the disease of one 51 year old woman suffering from severe dementia has transformed into the second most prevalent disease contributing to death of the older population, and a huge field of scientific study.[3]

Alzheimer's disease (AD) is the leading cause of dementia, accounting for between 50-80 % of all dementias.[4] It is characterised by the formation of extracellular amyloid plaques and intracellular neurofibrillary tangles which lead to the gradual decline in multiple areas of cognition, including memory, language, praxis and attention.[5] Worldwide there were an estimated 46.8 million people living with dementia in 2015 and due to the increasing life expectancy of the global population, incidences of dementia are expected to exceed 130 million by 2050.[6] The nature of dementia as a disease results in a huge economic burden. In the United States the cost of care in 2017 was valued at $232 billion.[7] As such, effective treatments (of which there are currently none) are highly sought after.

1.1.1 Hypotheses for the disease

The clinical symptoms of Alzheimer's disease are clearly caused by severe atrophy of the brain. However, the molecular cause of this atrophy is unknown. Several hypotheses have been formed which try and elucidate the molecular mechanism for the development of AD.

Amyloid Cascade Hypothesis

By far the most famous hypothesis for the development of Alzheimer's disease is the amyloid cascade hypothesis, written in 1992 by Hardy and Higgens.[8] This was the first paper to succinctly state that deposition of the Amyloid-β (Aβ) peptide is the causative agent in Alzheimer's disease, and that other pathologies occur downstream of this event (Fig. 1.1). This hypothesis continues to be the bedrock on which AD research is founded, and has had numerous "critical appraisals" defending and deriding it in the intervening years.[5,9] While the hypothesis manages to marry together several different genetic and environmental observations, the level of Aβ deposition in the brain as plaques was found to not correlate well with cognitive decline. Rather than signal the end of the cascade hypothesis, the hypothesis adjusted its focus from Amyloid-β plaques to smaller oligomers of Aβ as being the causative species in AD.[10] The amyloid cascade lives on, continuing to inform research and be used to generate ideas, even the alleged fraudulent analysis by Higgens could not mar it.[11,12]

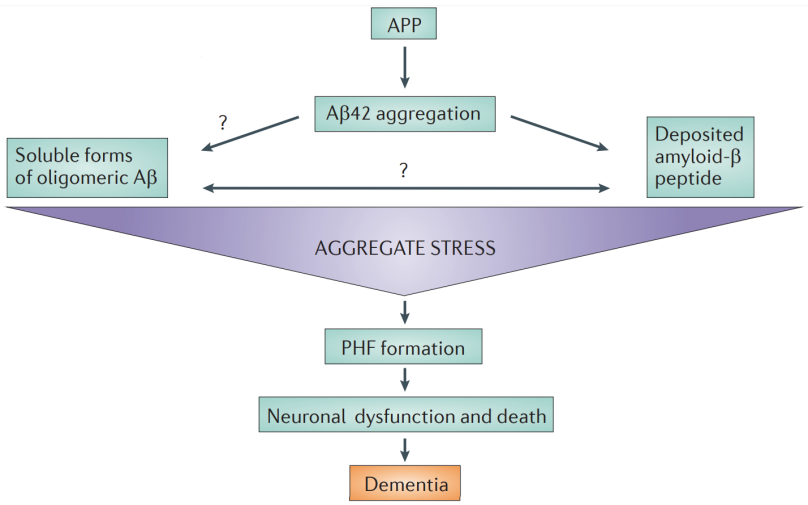


Figure 1.1 – Amyloid cascade hypothesis. The central tenet of this hypothesis is the deposition of Aβ. Exactly what the species that causes aggregate stress is unclear, but it lies somewhere on the equilibrium between small soluble oligomers and deposited Aβ plaques. Downstream of the aggregate stress is the formation of paired helical filaments (PHFs) of tau aggregates leading to neuronal dysfunction and dementia. Adapted with permission from Springer Nature. Copyright (2011)[5]

Channel Hypothesis

If small oligomers are the toxic species in Alzheimer's disease as the (revised) cascade hypothesis suggests, the question logically turns to where these Aβ oligomers exert their toxic effect. One proposal is that Aβ oligomers interact with the plasma membrane and disrupt its integrity by increasing membrane permeability and perhaps even forming Aβ pores. It is argued that by permeabilising the plasma membrane, ion homeostasis (in particular calcium homeostasis) is disrupted. This hypothesis therefore neatly explains the implication that calcium signalling is dysregulated in AD.[13] It has been shown that pores are formed upon the incorporation of Aβ into a planar bilayer and that the pores were ion-specific.[14] It has also been shown that only oligomers of Aβ (as opposed to monomers or fibrils) are able to cause lipid bilayer permeabilisation; however this report also challenged the formation of specific channels and reported that membrane permeabilisation was not ion specific.[15] The idea that oligomers and not monomeric Aβ can cause membrane permeabilisation is strengthened by the observation that oligomers preferentially interact with cell membranes relative to monomers.[16] It has also been shown that membrane permeabilization by Aβ can lead to phosphorylation of tau, resulting in neuron death.[17] And that following the release of calcium, increased reactive oxygen species are generated causing further damage to cells.[18]

Metals Hypothesis

The metals hypothesis is based on several observations including, dysregulation of metals ions, (which has been observed in AD) that Aβ plaques in AD are found enriched in metal ions, and that Aβ has been reported to be able to bind to a variety of metal ions. A comprehensive review of the current research surrounding Aβ and metals has been provided by Cheignon et al, 2018.[19] Support for the metals hypothesis has come from experiments showing that interactions with metals can increase the rate of oligomerisation of Aβ. It has been suggested that complexes of Aβ and redox active metals such as copper and iron can be a source of reactive oxygen species via redox cycling of the Aβ-metal complex. Prior in vitro work has shown that, in the presence of reducing and oxidising agents, the Aβ-Cu complex is able to generate reactive oxygen species (ROS), while work in cells has shown that administration of Aβ-Cu to cultured cells causes oxidative damage. Coupled with the observation that large amount of oxidative damage is found within the AD brain, the evidence for the metal hypothesis is convincing. The metals hypothesis is

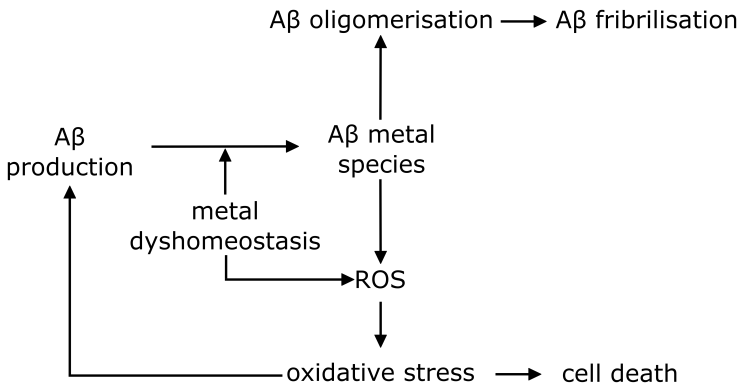


Figure 1.2 – Metal hypothesis. The metals hypothesis centers on the formation of an Aβ-metal complex, which has been shown to increase Aβ oligomerisation as well as cause oxidative stress.

summarised in Fig. 1.2 and will be explored in more detail in Chapters 3 & 4.

What About Tau?

So far all of the hypothesis mentioned focus on Amyloid-β as the errant species, but what about the neurofibrillary tangles that are equally a marker for AD as Aβ plaques? Intracellular neurofibrillary tangles are composed of hyperphosphorylated versions of tau proteins. In a healthy neuron, tau proteins help to stabilise microtubules, particularly the microtubules involved in the stability of the axon of the neuron. Phosphorylation of tau however results in a reduced affinity for microtubules, with neurotoxicity thought to be due to compromised axonal transport. Alterations in tau phosphorylation have been suggested to be due to alterations in tau kinases/phosphatases or possibly also indirectly caused by Aβ toxicity or oxidative damage.[20] Whether tau hyperoperation is upstream or downstream of Aβ pathologies is not clear, however evidence also exists that Aβ and tau act in concert.[21] While it is still probably true that Aβ receives more research attention than tau, this balance is slowly shifting. Through advancements such as obtaining cryo-EM structures of tau filaments[22], by understanding how tau aggregates and forms fibrils[23] and how these fibrils can spread like prions through the brain[24], the information surrounding tau and neurofibrillary tangles is slowly being unlocked. A schematic summarising some of the main points of the tau hypothesis is shown in Fig. 1.3.

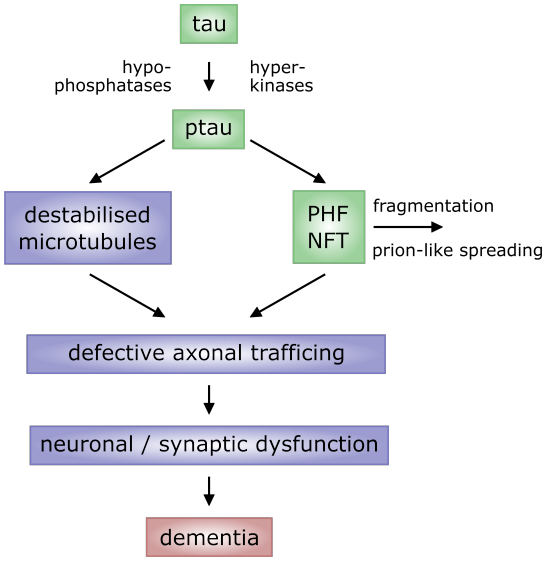


Figure 1.3 – Tau hypothesis. Through some process tau becomes hyper-phosphorylated (ptau) which decreases its affinity for microtubules. This destabilises microtubules as well as allowing increased ptau aggregation into paired helical filaments (PHF) and neurofibrilary tangles (NFT). Fragmentation of ptau aggregates can lead to prion-like spreading. Eventually axonal traffic is disrupted leading to neuronal dysfunction and dementia. But where (if at all) does Aβ exert its effect on this flow diagram?

1.2 Amyloid-β

Amyloid-β (Aβ) is a 36 - 43 amino acid peptide that is the main component of the amyloid plaques that are found in the brains of Alzheimer's disease patients. Although the Aβ plaques are localised to the brain, the Aβ peptide can be found throughout the body, and has been shown to be produced by a variety of different cells.[25] While the Aβ peptide is most associated with disease, it is present even under healthy conditions, which raises the question of this peptides' function- a question that has yet to be resolved.

1.2.1 Production of Aβ

How Amyloid-β is produced has been the focus of a lot of research and is generally well understood. Aβ is derived from the cleavage of the amyloid precursor protein (APP). APP is a transmembrane protein, of unknown function and is depicted in Fig. 1.4. To try and elucidate the role of APP, APP knock-out mice were generated.[26] The APP knock-out mice were shown to be viable and fertile but were of a lower weight than age matched controls and displayed decreased locomotor activity and forelimb

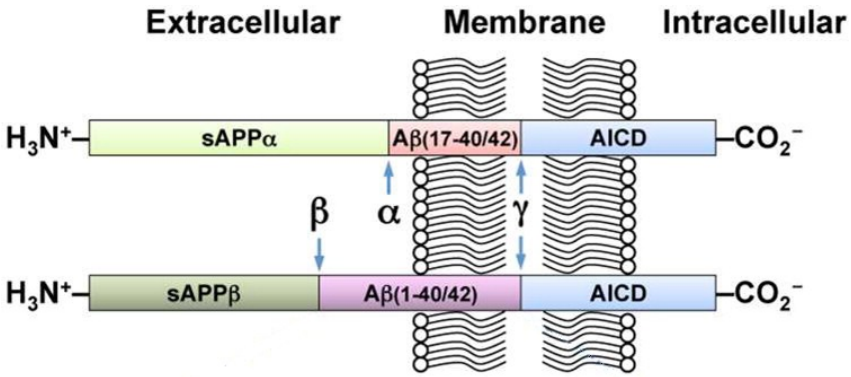


Figure 1.4 – Representation of the transmembrane APP. The positions at which each secretase cleaves are shown, leading to either nonamyloidogenic (top) or amyloidogenic (bottom) outcomes. Cleavage by α-secretase leads to the formation of a soluble (sAPPα) fragment outside the cell, subsequent cleavage by γ-secretase produces either $A\beta_{(17-40)}$ or $A\beta_{(17-42)}$ and a APP intracellular domain (AICD); alternatively initial cleavage by β-secretase gives rise to a soluble (sAPPβ) fragment and subsequent cleavage by γ-secretase produces $A\beta_{(1-40)}$ or $A\beta_{(1-42)}$ and similarly an AICD fragment. Adapted with permission from *ACS Chem. Biol.* 8, 5, 856-865. Copyright (2013) American Chemical Society.[31]

grip strength. Later research using APP knock-out mice led to suggestions that APP might play a role in long-term memory,[27] or that APP is important under hypoxic and ischemic conditions.[28] There is also evidence that APP (or more specifically its fragments) have various roles in gene regulation, nicely reviewed by Nalivaeva & Turner (2013).[29]

Three enzymes have been shown to act on APP and can give rise to either amyloidogenic or non-amyloidogenic peptides. Cleavage by α-secretase followed by γ-secretase releases the non-amyloidogenic $A\beta_{17-40/42}$. Conversely, cleavage by β-secretase followed by γ-secretase releases the amyloidogenic $A\beta_{1-40/42}$ peptide. Approximately 90 % of APP is said to go down the non-amyloidogenic pathway and be cleaved by α-sectretase.[29,30]

What factors govern whether processing of APP goes down the non- or amyloidogenic pathway remain elusive. One hypothesis that has received a fair amount of study is the differential localisation of α- and β-secretases into lipid microdomains, areas of the plasma membrane that are enriched in cholesterol and sphingolipids. The general hypothesis is that amyloidogenic processing occurs in lipid microdomains while non-amyloidogenic processing occurs elsewhere on the membrane, (for a selection of reviews see,[32,33,34]). Experiments supporting this hypothesis have shown that β-secretase is more active when in the presence of sphingolipids or cholesterol or

when the secretase is modified so that it localises within lipid microdomains.[35,36] Furthermore, evidence exists suggesting that β- and γ-secretases can undergo post-translational modification which aids their preclusion into microdomains.[37,38]

1.2.2 Clearance of Aβ

The level of Aβ in the brain depends on the balance of production verses clearance. If AD is characterised by the increased accumulation and deposition of Aβ, as the amyloid cascade suggests, this accumulation could arise from either increased Aβ production, or decreased clearance. There is a small subset of AD patients that have inheritable mutations that cause increased Aβ production (this is known as Familial Alzheimer's disease and is discussed in more detail in the following section). However, for the vast majority of AD patients these mutations are not present so increased production of Aβ cannot be the reason behind its accumulation. This has led some to propose that it is a dysfunction in Aβ clearance that is responsible for the build-up of Aβ in the AD brain.[39,40]

One route of clearance from the brain is through the blood brain barrier. The lipoprotein receptor-related protein (LRP) has been shown to mediate transport of Aβ from the brain into the blood stream.[41] P-glycoprotein has also been shown to be able to transport Aβ out of the brain. The efflux of Aβ out through the blood brain barrier is opposed by the receptor for advanced glycation end products, which transports Aβ back into the brain. Some have even suggested that breakdown or dysfunction of the blood brain barrier itself might contribute to the development of AD.[42]

There are also proteolytic degradation routes through which Aβ can be removed from the brain. Two enzymes that have been shown to be important in this regard are neprilysin and insulin-degrading enzyme. A decrease in neprilysin in AD brains has been noted, and shown to be correlated with increased Aβ deposition,[43] while insulin-degrading enzyme knockout mice are noted to have increased cerebral accumulation of Aβ.[44]

1.3 Risk Factors

By far the largest risk factor for developing Alzheimer's disease is age. Approximately 98 % of incidences of dementia occur in people over 65. As a person ages, the risk of developing AD increases exponentially.[45] Age however is not the most viable place for therapeutic intervention, and so we turn to genetic risk factors for the

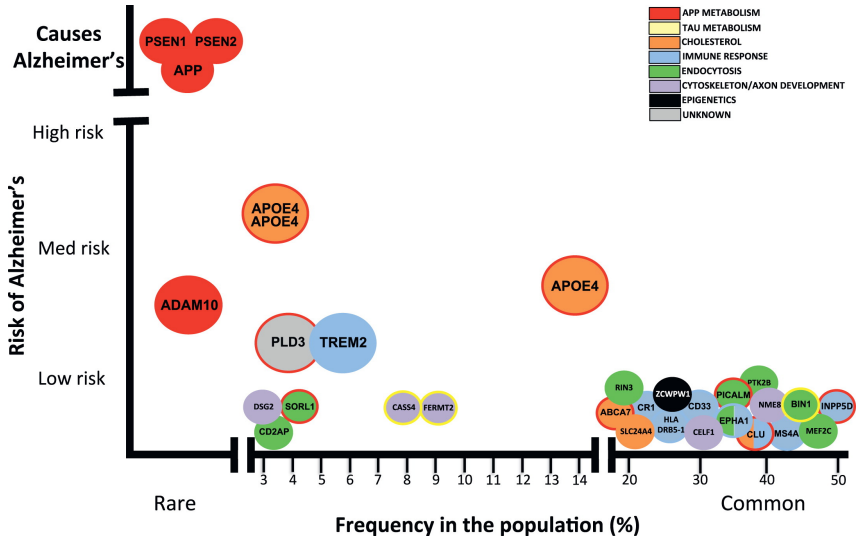


Figure 1.5 – Genertic risk factos in Alzheimer's disease. Associated risk against population frequency based on genome-wide associated studies. Reprinted from *Biol. Psychiatry* 77, 1, 43-51, Copyright (2015), with permission from Elsevier. [46]

disease. Some genetic risk factors are displayed in Fig. 1.5. This figure plots the risk of developing AD for a certain gene against that gene's frequency in the general population, and groups the genes by function.

1.3.1 Familial Alzheimer's disease

In the top left of Fig. 1.5 are a group of genes which, while rare, have a certainty to developing Alzheimer's disease. This subset of AD is referred to as familial Alzheimer's disease (FAD), and is where an individual has an autosomally dominant mutation that causes the onset of clinical symptoms earlier in life (under the age of 65). The three genes are all related to Aβ production: presenilin-1 & -2 (PSEN1 & 2), and amyloid precursor protein (APP). APP has already been discussed in Section 1.2; preseniln-1 & 2 are proteins that form part of the γ-secretase that cleaves APP. These mutations are therefore occurring in the machinery that forms Aβ, and generally increasing the formation of Aβ results in patients developing AD earlier. While FAD only accounts for a small proportion of Alzheimer's disease (AD) cases, it is regarded as a useful system to study, in order to help better understand the disease as a whole. [47] Familial Alzheimer's disease will be explored further in Chapter 3 where two APP mutations recognised as causing FAD will be studied.

1.3.2 Apolipoprotein E

Moving down Fig. 1.5 from high to low risk we come across the APOE4 gene which encodes a protein known as apolipoprotein E4 (apoE4). Apolipoprotein E4 was the first identified and remains the highest genetic risk factor for developing sporadic AD. Apolipoprotein E is a lipoprotein and is involved in the transport of cholesterol and lipids. In humans there are three isoforms of apoE differing at amino acid residues 112 and 158. The most common isoform of apoE is the apoE3 isoform which contains cysteine at position 112, and arginine at position 158. ApoE3 is not considered to be associated with a risk for developing AD. ApoE4 contains arginine residues at both positions 112 and 158, and therefore differs with the E3 isoform at only one position in its 299 total amino acid residues. The final, and most infrequent isoform is apoE2, which contains cysteine at both resides 112 and 158.

Individuals with one APOE4 allele ($\sim 15\,\%$ of the population) are between three and four times more likely to develop AD than individuals who do not possess any APOE4 alleles.[48] ApoE4 not only increases the risk of developing AD, but also reduces the age of symptom onset. Due to the strong evidence that apoE4 increases the risk of developing Alzheimer's disease and because of its high prevalence in the population it has been the target of a lot of research. The association between apoE4 and AD was made in the early 1990's and yet, even with the decades of ensuing research, how one Cys112Arg mutation causes such effects remains elusive. Apolipoprotein E will be revisited in Chapters 6 & 7.

1.4 The Drugs Don't Work

Currently there are no drugs to cure or prevent Alzheimer's disease. The only drugs available to patients help to (temporarily) alleviate some of the symptoms. These drugs all act by altering neurotransmission, such as increasing the lifetime of the neurotransmitter acetylcholine, or by protecting NMDA (N-methyl-D-aspartate) receptors from over activation.

So where are all the drugs? The answer to this question is certainly not because of a lack of trying. As of January 2018, there are 112 drugs being used in 133 different clinical trials across phases I to III. A comprehensive (annual) review is provided by Cummings et al (2018).[49] Many of the drugs currently undergoing trials have their mechanism of action originating from the amyloid cascade hypothesis. That is, the drugs aim to modify Aβ for example by, reducing the production of Aβ through inhibiting β-secretase, and increasing degradation or reducing aggregation though

use of small molecules or monoclonal antibodies.

While many drugs are being trailed for a cure to Alzheimer's disease, not one drug has made it past phase III, whereas some large failures have made headline news. News such as, that in the beginning of 2018, while Merck was discontinuing its β-secretase inhibitor, Verubecestat (MK-8931), which had made it all the way to Phase III , simultaneously Pfizer was announcing that it was withdrawing from dementia research entirely.

The drug situation looks less than hopeful, and coupled with the fact that no drug based on the amyloid cascade hypothesis has yielded positive results, some have been encouraged to question the cascade hypothesis and more generally the role of Amyloid-β in Alzheimer's disease.[50] Some researchers have gone as far as suggesting that the Alzheimer's disease research field should move away from Aβ and start to focus on tau protein.[51] And while tau protein is still yet to receive the same level of attention as Aβ, recently there has been an increase in the number of drugs being trialled that try to target tau protein.[49] As for AD hypotheses other than the amyloid cascade, they have also not remained out of the firing line. In regards to the metals hypothesis, Drew (2017) has argued to abandon copper chelation as a therapeutic,[52] which swiftly drew criticism by Squitti et al (2017).[53]

There are many reasons why drugs fail clinical trials, and incorrect hypothesis are certainly one of them. But perhaps a more nuanced reason would be to do with the insidious nature of Alzheimer's disease and a failure of clinical trials to properly account for this. Alzheimer's disease takes decades to develop, and so by the time a person starts to display mild clinical symptoms, damage has already been occurring to their brain for some time. Logically, it is unreasonable to expect a therapeutic designed to target the underlying cause of AD to reverse neuronal damage and result in improved cognitive function. If this is true, early intervention is key. Biomarkers for AD are useful in this regard, and their use is becoming more and more common in identifying candidates for trials and trial outcomes.

Another interesting opportunity for improving clinical trials lies with Familial Alzheimer's disease (FAD). As the age of onset for patients with FAD is more predictable than sporadic AD, patients can be given drugs earlier to see if they delay the age of onset. While such studies would inevitably take a long time, trials of this kind are currently being conducted. Some researchers however warn against conflating the aetiologies of FAD and sporadic AD, arguing that the overreliance of viewing FAD as an accelerated version of sporadic AD is what has been hampering success in the field.[50] Regardless, the outcomes of such trials are eagerly awaited, wherein decades of Aβ heavy focused research may be vindicated, or rapidly side-lined.

1.5 Thesis Outline

This thesis explores the 'metal hypothesis' of Alzheimer's disease (AD). It begins by looking at the interaction of Aβ with copper and tries to draw conclusions by comparing the interactions of wild-type and mutant Aβ. The thesis then moves on to explore redox cycling of the AβCu complex as a source of reactive oxygen species. Many studies have shown that AβCu cycling *can* produce reactive oxygen species, while little attention been directed towards *how fast* reactive oxygen species can be produced. This thesis explores the kinetics of the proposed AβCu redox cycling, asking the question- How fast does redox cycling occur? And knowing how fast redox cycling occurs, would the process occur on a biologically meaningful timescale?

Having obtained the kinetics of redox cycling, this thesis then moves on to study lipid peroxidation, catalysed by redox cycling of the AβCu complex. Finally, this thesis looks at the lipoprotein apolipoprotein E (apoE), which is the biggest genetic risk factor for developing late onset AD. How apoE restructures lipids into a lipoprotein particle is explored, including the affects this restructuring has on lipid peroxidation.

1.6 Publications From This Work

Results presented in Chapter 3 are included as part of two publications:

T. Branch, P. Girvan, M. Barahona and L. Ying, Introduction of a Fluoresce Probe to Amyloid-β to Reveal Kinetic Insights into Its Interactions wit Copper(II), *Angew. Chem. Int. Ed.*, 54, (4), 1227-1230, 2015.

P. Girvan, T. Miyake, X. Teng, T. Branch and L. Ying, Kinetics of the Interactions between Copper and Amyloid-β with FAD Mutations and Phosphorylation at the N terminus, *ChemBioChem*, 17, (18), 1732-1737, 2016.

Results presented in Chapter 4 have been published as:

P. Girvan, N. J. Brooks, G. S. Baldwin and L. Ying, Redox Kinetics of the Amyloid-β-Cu Complex and Its Biological Implications, *Biochemistry*, 57, (43), 6228-6233, 2018.

Chapter 2

Methods and Materials

2.1 Fluorescence - an introduction

* Due to its speed and sensitivity, the use of fluorescence as a technique has become ubiquitous within the life sciences. Fluorescence is a property of certain molecules, known as fluorophores, which are able to emit light following absorption of electromagnetic radiation. Fluorescence is often described with the use of a Jablonski diagram, illustrated in Fig. 2.1.

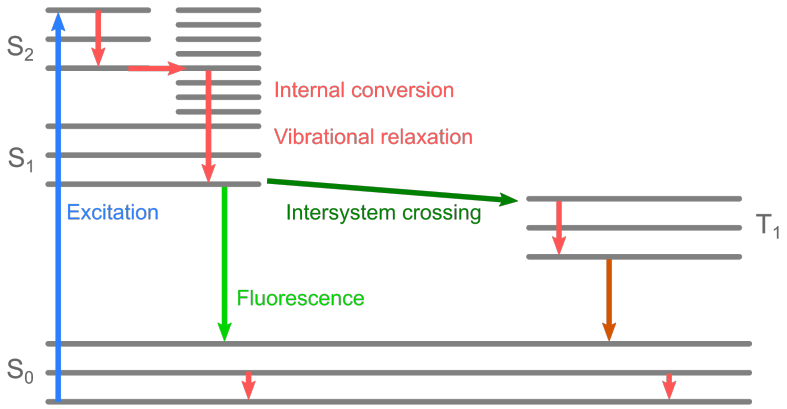


Figure 2.1 – Jablonski diagram.

The Jablonski diagram shows the singlet ground (S_0), first (S_1) and second (S_2) electronic states. Upon absorption of a photon of energy $h\nu_A$, an electron is promoted from the ground state to a higher electronic state (in this case S2). Transitions obey

*The following introduction is based mainly off of Lakowicz's *Principles of Fluorescence Spectroscopy* [54]

the Frank-Condon principal, which roughly states that because transitions occur so fast ($\sim 10^{-15}$ s), they can be considered to be instantaneous when compared with the (much slower) motion of nuclei. Following excitation of an electron to a higher electronic state, the electron will relax to the lowest vibrational level of the first excited state (S1) by a process known as internal conversion. This internal conversion typically occurs within $\sim 10^{-12}$ s, and is a consequence of Kasha's rule, which states that photon emission occurs most likely from the lowest excited state. Finally the electron can return to the ground state, emitting a photon ($h\nu_F$), typically occurring on the $\sim 10^{-8}$ s timescale. The transition back to the ground state can return to any of the vibrational levels within S_0 and so $h\nu_F$ is typically of a lower energy (longer wavelength) than $h\nu_A$. This shift is known as the Stokes shift, and is effectively exploited in fluorescence spectroscopy to sperate excitation and emission radiation through the use of optical filters.

The final aspect of the Jablonski diagram concerns the process of phosphorescence. In contrast to fluorescence (where transitions occur to and from singlet states), phosphorescence occurs as a transition from a triplet state to a singlet state. It is therefore spin forbidden and occurs much more slowly than fluorescence ($10^{-3}\,s^{-1}$ to $1\,s^{-1}$). Before phosphorescence can occur the system must undergo intersystem crossing ($S_1 \rightarrow T_1$). upon relaxation back to the ground singlet state a photon ($h\nu_P$) is emitted. Phosphorescence typically occurs at longer wavelengths than fluorescence. When in the triplet state a molecule can no longer fluoresce. Due to the long-lived nature of phosphorescence, transitions to the triplet state can give rise to fluorophore blinking, as the molecule is essentially dark when in this state.

2.2 Experimental Methods

2.2.1 Fluorometry

Steady state fluorescence measurements were made with a FluoroMax®-4 (HORIBA) spectrofluorometer controlled via FluorEssence™ (HORIBA) software. The fluorimeter uses a xenon arc lamp to produce UV and visible light, which is passed through an excitation monochromator to allow the selection of the excitation wavelength. A further monochromator is located on the emission side to allow the selection of the emission wavelength. Both the excitation and emission light is also passed through slits to select the bandwidth of light allowed to pass. Excitation and emission slit widths were chosen such that the fluorescent intensity was ca. 10^4-10^6 counts per second to remain well within the linear range of the instrument. The fluorescence

emission is detected using a photon multiplier tube (PMT), which allows the number of photons to be counted over a set integration time. Quartz micro cuvettes (Hellma Analytics) with a light path of 10 mm × 2 mm were used which allowed low volumes of at least 100 µL to be used.

2.2.2 Ultraviolet-Visible Spectroscopy

Absorption measurements were made using an ultraviolet-visible (UV-Vis) spectrophotometer (Lambda 25, PerkinElmer). Incident light is provided by either a deuterium bulb (providing UV light) or a tungsten bulb (providing visible light). A diffraction grating is used to separate out the light into a spectrum and then passed through slits limiting the bandwidth to 1 nm. The light path is split into two paths, one being used as a reference for fluctuations in lamp intensity while the other is passed across a sample in a quartz cuvette with a path length of 1 cm. The absorbance (A) of a sample is calculated from the amount of light that is transmitted (T) through the sample relevant to the reference by,

$$A = -\log T \tag{2.1}$$

If the extinction coefficient (ε) of a absorbing species at a particular wavelength is known, the concentration (c) of the absorbing species can be determined from the absorbance via the Beer-Lambert law,

$$A = c\varepsilon l \tag{2.2}$$

where (l) is the path length of the light through the sample.

Determining protein labelling efficiency

The concentration of proteins that had been labelled with a fluorescent tag were determined from the peak absorbance of the dye using the manufacturer stated extinction coefficient for that dye. The proportion of proteins in a sample that had been labelled was determined by comparing the concentration calculated by using the dye peak absorbance with the concentration determined from the absorbance of the protein amino acids at 280 nm. A correction factor (γ) for the amino acid absorbance at 280 nm must be made to account for the contribution of the dye absorbance.

$$c_{280\,\mathrm{nm}} = \frac{A_{280\,\mathrm{nm}} - \gamma A_{\mathrm{dye}}}{\varepsilon_{280\,\mathrm{nm}} l} \tag{2.3}$$

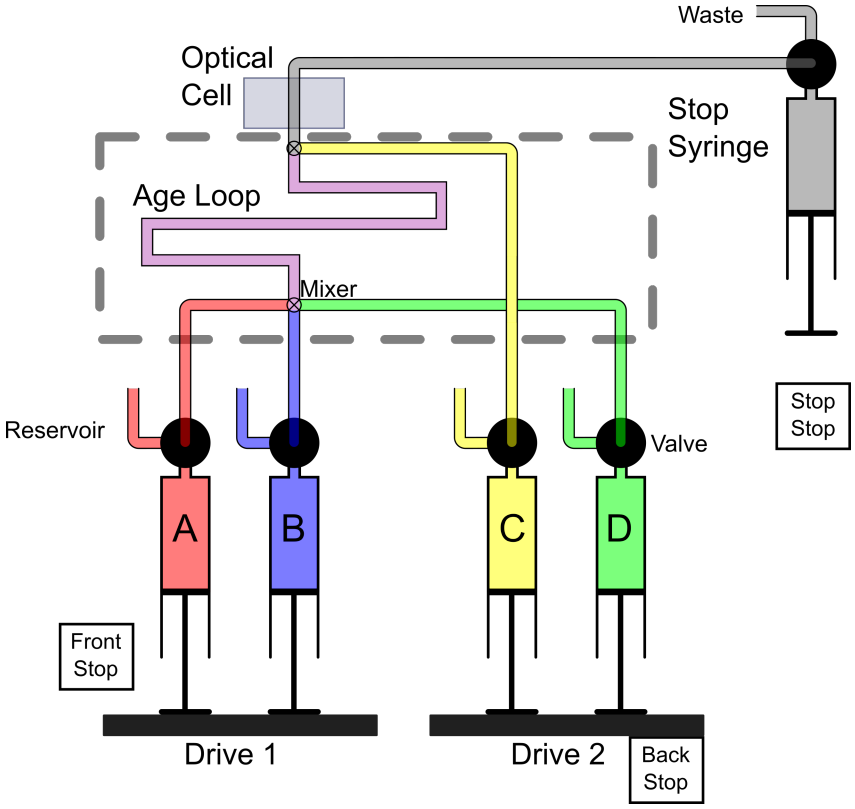


Figure 2.2 – Schematic of the stopped flow instrument.

2.2.3 Stopped Flow

Stopped flow apparatus (KinetAsyst SF-610X2, HI-TECH Scientific) allows the progress of fast chemical reactions to be followed through time. Fast kinetics are able to be followed due to the short dead times (ca 1 ms) that can be achieved by rapidly mixing solutions from various syringes and then suddenly stopping the flow when it has filled the observation chamber. A schematic of a stopped flow instrument is provided in Fig. 2.2 Several spectroscopic techniques can be used to follow the progress of the reaction including UV-Vis or anisotropy but throughout this work fluorescence was employed.

Originally fluorescence excitation was provided by a xenon lamp that was first passed through a monochromator to select the desired wavelength. The intensity of the lamp, combined with the low concentrations of fluorophore used in experiments (ca. 50 nM) resulted in a high amount of noise in the resulting traces. To overcome this the xenon lamp was replaced with a higher intensity fibre coupled laser diode (MCLS1-473-20, Thorlabs) set to 473 nm and using the lowest power setting (∼8.9 mW).

Due to the laser diode's digital feedback system, occasional step changes in the intensity were observed. These step changes could be corrected for by splitting the excitation beam before it reached the sample using a beam splitter which redirected approximately 20% of the light to be used as a reference signal. However it was also noted that if you left the laser diode running for ∼1 h prior to making measurements, the intensity had stabilised and there was no need to use the beam splitter.

Fluorescence emission was filtered using a 515 nm long pass filter (515GY, Comar) before being detected by a photon multiplier tube. Data points were taken using a log time-scale sampling scheme. For each data point, a minimum of 7 traces were averaged. Time points below 2 ms were excluded due to the instrument dead time (ca. 1 ms).

Single mixing mode

In single mixing mode two solutions are placed into syringes C & D while the valves for syringes A & B are left open, thereby disconnecting them from the flow path. Drive 2 is pushed up pneumatically, simultaneously pushing the solutions from syringes C & D through the flow circuit where they are mixed immediately prior to entering the optical cell. After ca. 90 µl of solution has filled the stop syringe it hits the 'stop' stop the flow is halted and data recording begins.

Double mixing mode

In double mixing mode two solutions (in syringes A & B) are first mixed together allowing a reaction to occur, then after a defined delay, mixed with a third solution (in syringe C). Before any mixing occurs, the 'front' stop is moved above drive 1, to allow ca. 150 µl of solution to be passed into the flow circuit, while the 'back' stop is moved behind drive 2 to prevent solution being pushed into syringes C & D. Drive 1 is first pushed up, mixing the solutions in syringes A & B and filling the age loop. Once the 'front' stop is hit, the delay timer is started. After a set time has passed drive 2 is pushed up using the buffer in syringe D to push the 'aged' solution from the age loop and mix it with the contents of syringe C. After ca. 240 µl has entered the stop syringe the 'stop' stop is hit and data recording commences.

2.2.4 Confocal Microscopy

Confocal microscopy is a microscopy technique where a spacial pinhole is used to block out of focus light and thereby increase the optical resolution in the axial direction. The use of this pinhole is illustrated in Fig. 2.3. It can be seen that

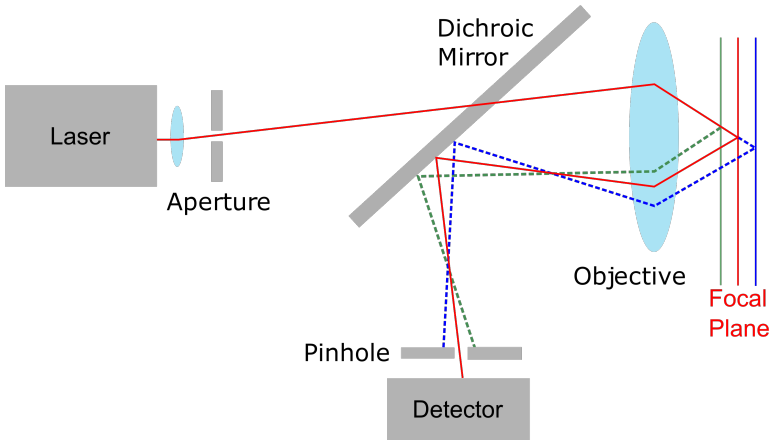


Figure 2.3 – Confocal schematic. The placement of a pinhole in front of the detector in a confocal microscope is used to reject out of focus light and increase axial resolution. Life from either above (blue dashed line) or below (green dashed line) the plane of focus is blocked by the pinhole, while only the in focus (red solid line) reaches the detector.

fluorescence originating from either above or below the focal plane hits the pinhole and does not reach the detector. This provides much greater resolution compared to a typical wide field microscope, but as much of the fluorescence from the sample is discarded higher intensity excitation sources or more sensitive detectors must be employed.

Confocal microscopy is often used in a scanning fashion, so as to produce a fluorescent image as would be observed in traditional wide field microscopy but with much greater resolution in the axial direction. However, in this thesis confocal microscopy is used in a fixed position and not scanned. This allows the fluorescence of femtoliter volumes within solutions to be observed, as fluorescent particles diffuse through the confocal volume due to Brownian motion.

The custom built confocal microscope used in this work is shown in Fig. 2.4. A tuneable argon ion laser (35LAP321-230, Melles Griot, USA) is used as the excitation source. The beam is passed through a dove prism which totally internally reflects the beam and so removes plasma lines from the excitation source. The beam is focused to a point, where a spatial filter removes aberrations, before a lens re-collimates the light. Before entering the inverted microscope (Nikon Eclipse TE2000-U) the beam is passed through an iris which selects the central part of the beam. Inside the microscope a dichroic mirror reflects the excitation light towards the high numerical aperture (60× 1.45 NA oil) objective, while allowing fluorescence from the sample to pass though. Emission filters, consisting of a long pass filter and a bandpass filter allow the majority

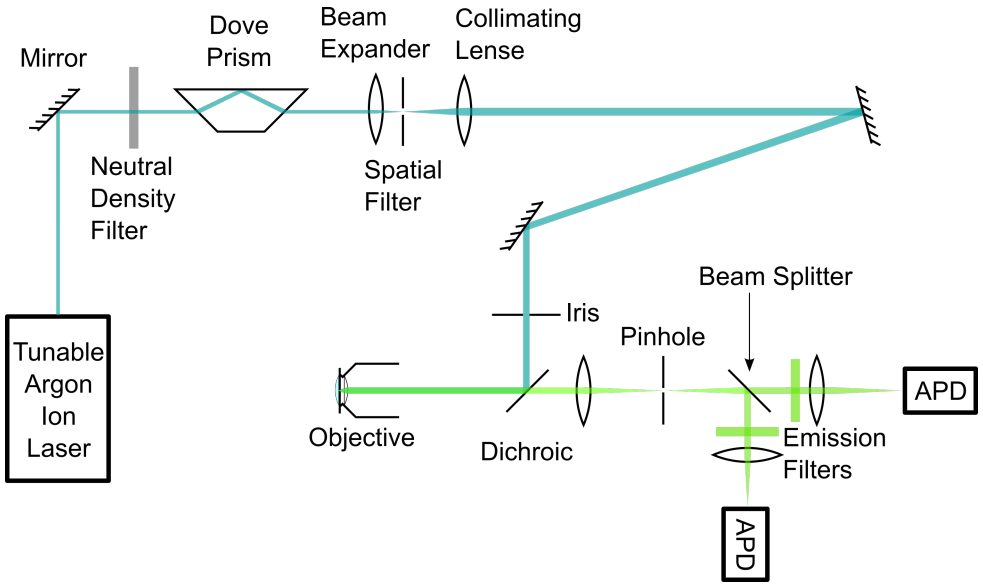


Figure 2.4 – Confocal microscope. Schematic of the main features of the custom built confocal microscope.

of the fluorescence peak to pass towards the avalanche photodiode detectors (single photon counting module SPCM-AQR-14) while preventing misdirected excitation photons or background fluorescence from interfering with the signal. The APDs have a dead time of 50 ns where following detection of a photon, no subsequent photons within this deadtime will be able to be detected. To overcome this the signal is split using a 50/50 beam splitter and detected with two independent APD modules (as shown in Fig. 2.4. The two APD modules are connected to a digital hardware correlator (flex02-01d/c) which has a minimum sample time of 1.5625 ns.

Fluorescence correlation spectroscopy

Fluorescence correlation spectroscopy (FCS) is a methodology which tries to extract useful information from the seemingly noisy and random fluorescent intensity fluctuations that fluorescent species display. As the name suggests, this useful information is obtained by performing an autocorrelation on the fluorescent intensity signal, as it spontaneously fluctuates about its equilibrium value. In essence this autocorrelation function assess how similar the fluorescent signal is at some time t to the same signal at time $t+\tau$, where τ is varied from tens of ns to hundreds of s. Fundamentally FCS can be used to measure any process which gives rise to fluctuations in fluorescence, but most commonly it is used to determine the concentration and diffusion rate of

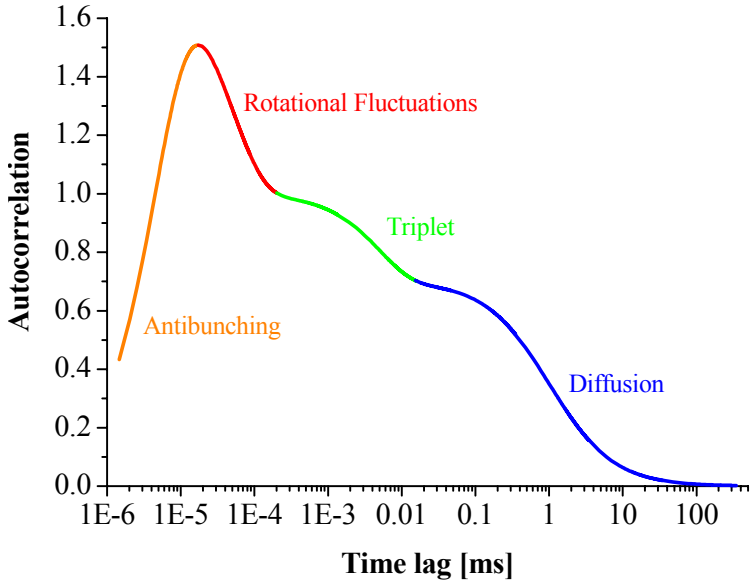


Figure 2.5 – Example FCS trace Timescales of various processes which can be monitered by autocorrelation analysis.[55]

fluorescent species, or the kinetics of intra- or intermolecular processes.

As FCS measures fluorescent intensity fluctuations, unintuitively the best signal to noise is achieved when there are the fewest molecules to observe. In order to achieve this the small excitation volume of the confocal microscope detailed in section 2.2.4 can be combined with nM concentrations of fluorophore. The result of this combination is that, on average there will only ever be one molecule contributing to the fluorescent signal at a time.

The normalised autocorrelation function (G(τ)) can be expressed as,

$$G(\tau) = \frac{\langle \delta I(t) \delta I(t+\tau) \rangle}{\langle I(t) \rangle^2} = \frac{\langle I(t) I(t+\tau) \rangle}{\langle I(t) \rangle^2} - 1 \tag{2.4}$$

where $I(t)$ and $I(t+\tau)$ are the fluorescent intensities at time t and $t+\tau$ respectively. For a typical fluorophore the autocorrelation function would produce a trace as shown in Fig. 2.5. The majority of the amplitude of this trace is made up of a phase relating to the diffusion of the fluorophore (occurring on the ms timescale). A phase due to the fluorophore entering the triplet state can also be identified (occurring on the µs timescale).

In order to be able to accurately resolve fast processes two detectors can be used simultaneously (as shown in Fig. 2.4). The fluorescent signal is split using a beam splitter and detected using two identical APDs. The signals from the APDs are then

pseudo-autocorrelated (cross correlation of the two identical signals from each APD). This removes the correlation due to the dead time of the instrument, which would otherwise appear as a strong correlation in the µs regime. Using two detectors in this way allows FCS traces to be measured down to tens of ns.

In order to extract useful parameters from the autocorrelation traces they must be fit to specific functions. The diffusion of a species can be described as,

$$G(\tau) = \frac{G(0)}{1 + \frac{\tau}{\tau_{\mathrm{D}}}} + C \tag{2.5}$$

Where $G(0)$ is the amplitude of the curve and τ_{D} is the average time taken for a molecule to diffuse though the confocal volume. Equation 2.5 actually describes diffusion in only two dimensions, rather than the three dimensions in which diffusion is actually taking place. This is because the size of the confocal volume in the axial direction is much larger than the size in the radial direction. Because of this larger size in the axial direction, fluctuations in the signal due to diffusion in this direction will be small, and therefore have a minor impact of the FCS autocorrelation trace and so can be ignored.

The fitted parameter $G(0)$ is inversely proportional to the average number of fluorescent species, ($\langle N \rangle$) in the confocal volume.

$$G(0) \propto \frac{1}{\langle N \rangle} \tag{2.6}$$

If the volume, (V) of the confocal spot is known, the bulk concentration, (C) can be estimated using,

$$C = \frac{1}{G(0)} N_{\mathrm{A}} V \tag{2.7}$$

where N_{A} is Avogadro's number. For the confocal system described here, the cofocal volume is ∼1 fl.

The diffusion time (τ_{D}) is instrument dependant and depends on the size of the confocal spot, but can be related to the (instrument independent) diffusion coefficient (D).

$$\tau_{\mathrm{D}} = \frac{r_0^2}{4D} \tag{2.8}$$

where r_0 is the radius of the confocal spot.

Assuming that the diffusing particles are spherical the diffusion coefficient can be used to determine the hydrodynamic radius (R_h) using the Stokes-Einstein equation,

$$D = \frac{kT}{6\pi\eta R_h} \tag{2.9}$$

These equations also allow a system to be calibrated by measuring the instrument dependant τ_{D} for a species with a known diffusion coefficient.

Although diffusion accounts for a large portion of the FCS trace, it is not always the only part. If the laser power is high enough (e.g. >100 µW) the probability of the fluorophore entering the triplet state will become large enough to make an impact on the FCS trace. This triplet state dynamics can be accounted for by introducing a new term into our equation describing 2D diffusion (Eq. 2.5).

$$G(\tau) = \frac{G(0)}{1 + \frac{\tau}{\tau_{\mathrm{D}}}}(1 - F + F\exp\left(-\tau/\tau_{\mathrm{F}}\right)) + C \tag{2.10}$$

Where F is the fraction of fluorophores in the triplet state and τ_{F} is the triplet lifetime.

2.2.5 Circular Dichroism

Circular dichroism (CD) is a powerful tool which (among other uses) has found itself indispensable within the biochemistry field, where it is most often used for the determination of coarse secondary structure of biomolecules such as proteins and DNA. CD makes use of the chiral nature of the repeating units found within biomolecules (helices, β-sheets), and functions by determining the difference in absorbance between left-handed and right-handed circularly polarised light as the light interacts with the chiral units.

CD measurements were made on a Chirascan™ Circular Dichroism Spectrometer (Applied Photophysics) controlled with via the Chirascan (Applied Photophysics) software. The temperature of the cuvette holder was controlled using a thermoelectric temperature controller (MELCOR MTCA-9060) and a circulating water bath (Julabo AWC100).

CD signal is measured in ellipticity (Θ) which has units of millidegrees (mdeg). This unit is concentration dependant and so the majority of CD spectra presented in this thesis are presented in units of molar ellipticity ($[\Theta]$) which has the historical unit of degcm^2/dmol. To convert mdeg to molar ellipticity ($[\Theta]$) the following equation was used,

$$[\Theta] = \frac{\mathrm{mdeg} \times \mathrm{MRW}}{10 \times L \times c} \tag{2.11}$$

where MRW (mean residue weight) is the average molecular weight of the amino acids within the protein (molecular mass of the protein divided by the number of amino acids in the protein) with units of g/mol, L is the pathlength in cm and c is the concentration of the protein in $\mathrm{g\,l^{-1}}$.

In CD spectroscopy sample concentration is an important parameter to optimise in order to obtain the best spectra. The largest difference in ellipticity (CD signal) will be obtained for high sample concentrations. However, as the difference in absorbance is what is measured, higher concentrations will lead to more absorbance and less photons reaching the detector resulting in worse signal to noise.

In addition to the sample contributing to the absorbance, both the cuvette and sample solution will also contribute to higher absorbance and worsening of signal to noise. To minimise unwanted absorbance, highly transparent quartz cuvettes with path lengths of 1 mm or 2 mm (Hellma Analytics) were used. Samples were prepared in 10 mM phosphate buffer, to reduce the absorbance contribution from the solution.

Generally, the best signal to noise in CD spectroscopy is attained when the optical density is $\sim$0.7. It is also beneficial to monitor the high tension (HT) voltage when recording CD spectra. The HT voltage is the voltage applied to the PMT detector within the CD instrument. Unlike the PMTs present in the fluorimeter or stopped flow described above which are kept at a constant gain across a measurement, the PMT in a CD instrument constantly adjusts the level of gain in order to try and maintain a constant light level. Generally it is considered best to maintain a HT voltage $<$700 V. HT voltages above this suggest that not enough photons are reaching the detector and the increased gain results in worse signal to noise, and unreliable spectra.

2.2.6 Gel Imaging

Expressed and purified proteins were analysed by SDS-PAGE. Tris-glycine gels containing either 12 % or 15 % of acrylamide/bis-acrylamide, 19:1 (5 % crosslinker) (BioRad) were hand cast using 1 mm casting plates (BioRad). Gels were stained for total protein using InstantBlue™ (Expedeon) Coomassie protein stain and imaged using a LAS-4000 (Fujifilm) imager.

Fluorescent gels

Gels that contained fluorescently labelled protein were imaged using a Typhoon FLA 9500 (GE-healthcare) laser scanner. In order to be able to visualise the protein molecular weight ladder a fluorescent ladder was used, Precision Plus Protein™ Dual

Xtra Prestained Protein Standards (BioRad). This ladder has bands that can be excited using 635 nm and 532 nm light. 16 bit images were acquired at a resolution of 50 µm using a PMT voltage that gave maximal signal without pixel saturation.

2.3 Materials

2.3.1 Amyloid beta peptides

The amyloid-β peptides used in this work were all purchased from (or custom synthesised by) AnaSpec (CA, USA) via Cambridge Bioscience (UK). The Aβ peptides all consisted of either the first 16 or 40 residues. For much of the metal interaction studies detailed later, the truncated Aβ16 peptide is utilised. This truncated peptide contains the metal binding residues but does not show the propensity of the longer forms of Aβ to aggregate. This truncated version is routinely used as a model peptide when studying the interactions between Aβ and metal as it is much easier to handle than the full length Aβ. The Aβ16 peptides were dissolved in 50 mM HEPES (pH 7.5) buffer containing 100 mM NaCl and stored at −20 °C. For studies involving Aβ binding to lipids the longer Aβ40 peptide is used, as it contains both the metal binging region, and the hydrophobic tail. The Aβ40 peptide was dissolved in 1 % ammonium solution (to prevent it from aggregating) and stored at −20 °C.

All of the Aβ16 peptides were labelled on Lys16 with HiLyte™ Fluor 488. Where noted some of the Aβ40 peptides were also labelled with HiLyte™ Fluor 488 at a cysteine residue that was introduced at position 20. The concentration of stock solutions of peptide was determined using UV/Vis and an extinction coefficient for the peak absorbance of the HiLyte™ Fluor 488 (ε= 70 000 cm^{-1} M^{-1}) when present. Peptides were diluted to required concentrations in 50 mM HEPES (pH 7.5) buffer containing 100 mM NaCl immediately prior to use.

Aβ16	DAEFR	HDSGY	EVHHQ	K*				
mAβ	DAEFG	HDSGF	EVRHQ	K*				
Aβ16(H6R)	DAEFR	RDSGY	EVHHQ	K*				
Aβ16(D7N)	DAEFR	HNSGY	EVHHQ	K*				
Aβ40	DAEFR	HDSGY	EVHHQ	KLVFF	AEDVG	SNKGA	IIGLM	VGGVV
Aβ40	DAEFR	HDSGY	EVHHQ	KLVFC*	AEDVG	SNKGA	IIGLM	VGGVV
Aβ40(H6R)	DAEFR	RDSGY	EVHHQ	KLVFC	AEDVG	SNKGA	IIGLM	VGGVV
Aβ40(D7N)	DAEFR	HNSGY	EVHHQ	KLVFC	AEDVG	SNKGA	IIGLM	VGGVV

* HiLyte 488

2.3.2 Buffers

HEPES (4-(2-Hydroxyethyl)-1-piperazineethanesulfonic acid) purchased from Sigma-Aldrich (UK) as a pH 7.5 buffered solution was used throughout much of this work. Milli-Q™ 'ultrapure' water with a resistivity of 18.2 MΩ cm was used throughout. Sodium chloride (NaCl) (Sigma-Aldrich, UK) at a purity ≥ 99.5 % was dissolved in Milli-Q™ water to create a 2 M stock solution which was stored at 5 °C.

2.3.3 Lipids

GM1 (Monosialoganglioside GM1), DLPC (1,2-dilauroyl-sn-glycero-3-phosphocholine) and DMPC (1,2-dimyristoyl-sn-glycero-3-phosphocholine) were all purchased as lyophilised powders from Sigma-Aldrich (UK).

Fluorescently labelled GM1 (BODIPY™FL C5-Ganglioside GM1) was purchased from ThermoFisher Scientific. The BODIPY fluorophore is present in place of one of the lipid hydrocarbon chains.

The lipid peroxidation probe, C_{11}-BODIPY$^{581/591}$ was purchased from ThermoFisher Scientific.

Lipids were dissolved in methanol (Sigma-Aldrich, UK) and mixed as required, aliquoted and dried under a stream of nitrogen. Lipid films were placed under vacuum overnight. For making small unilamellar vesicles the lipid film was hydrated in buffer for 1 h with agitation. The temperature was maintained above the transition temperature of the lipid. The lipid suspension was extruded eleven times passing it through a polycarbonate membrane containing 100 nm pores.

2.3.4 Other reagents

Copper(II) chloride dihydrate ($CuCl_2$) at a purity > 99 % was purchased from Sigma-Aldrich (UK) and dissolved in water to create a 20 mM stock solution which was stored at 5 °C. Ascorbate solutions were made immediately prior to each experiment (to minimize auto-oxidation) by dissolving (+)-sodium L-ascorbate (Sigma-Aldrich, UK) ≥ 99.0 % in 50 mM HEPES (pH 7.5) buffer containing 100 mM NaCl. Hydrogen peroxide (H_2O_2) solutions were prepared by diluting a 35 wt. % hydrogen peroxide solution (Sigma-Aldrich, UK) in 50 mM HEPES (pH 7.5) buffer containing 100 mM NaCl.

Chapter 3

Interactions of Aβ & Metal Ions

3.1 A brief introduction

The aberrant behaviour of transition metals has been variously linked to many neurodegenerative diseases.[56] In Alzheimer's disease it has been noted that the hallmark plaques, formed mainly of the Amyloid-β (Aβ) peptide, are highly enriched for transition metals. High concentrations of copper (∼0.4 mM), zinc (∼1 mM) and iron (∼1 mM) have been reported in the plaques of Alzheimer's disease brains.[57] Metal ions are highly important for biological life, being at the core of crucial biological processes. Transition metals are highly reactive, and it is this reactivity which is harnessed by many metalloenzymes to make and break chemical bonds. The reactive nature of these transition metals can also be a detriment to life, and so these metals are therefore highly regulated within biological systems. It is therefore not surprising that the observation of transition metal dyshomeostasis in Alzheimer's disease has sparked fervent research into this area.

3.1.1 Metals and aggregation

The aggregation of Aβ monomers to dimers, small oligomers, prefibrils and fibrils lies at the heart of the amyloid cascade hypothesis. But how does this aggregation come about? In vitro the aggregation process can be followed by a variety of techniques. A commonly reported technique is the use of the dye thioflavin T, which has a marked increase in quantum yield when bound to the beta-sheet formation within fibrils.[58,59] The fibrillisation of Aβ shows a characteristic sigmoidal curve (Fig. 3.1). Initially a lag phase occurs where the first templates or 'seeds' are formed, as well as amplification of these seeds through their growth and proliferation.[60] This growth rapidly increases, being exponential in nature, until finally a plateau is reached.

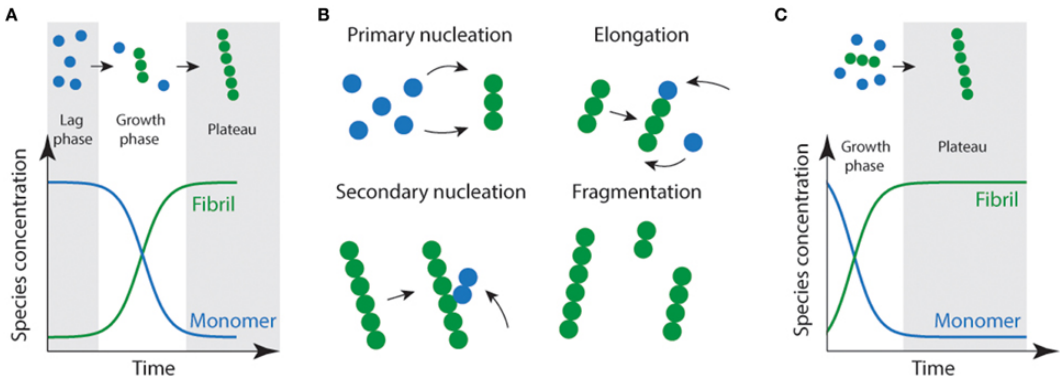


Figure 3.1 – Schematic of Aβ fibrilisation. (A) Typically fibrilisation exhibits a lag phase before a rapid growth phase after which a plateau is reached. (B) Fibril growth occurs via many process including, primary and secondary nucleation, elongation and fragmentation. (C) The lag phase can be reduced by addition of a variety of 'seeds' to the Aβ monomers, removing the need for the Aβ monomers to first undergo primary nucleation. Image reproduced with permission from Zeineddine and Yerbury (2015) under a Creative Commons Attribution License.[62]

This plateau represents a new equilibrium, where fibrils dominate the system over Aβ monomers. The rapid growth of the fibrils can be due to many processes, such as monomer addition to the ends of the fibril (elongation), but can also be due to monomer addition to the middle of the fibril (secondary nucleation). This secondary nucleation in effect creates another 'end' to which elongation can occur, and has been suggested to be the main factor driving protein fibrilisation.[61] Finally fragmentation of fibrils can also occur which, like secondary nucleation, generates more ends for elongation. Indeed, it is fragmentation of fibrils that is used as the rationale behind the common observation that an agitated sample of Aβ will form fibrils much faster than a stationary sample.

The lag phase associated with Aβ fibrilisation can not only be decreased by agitation of the sample (causing fragmentation), but by many other means. For example, addition of a mature 'seed' (i.e. fibrils) to the starting mixture of monomeric Aβ reduces the lag phase considerably. This decrease in the lag phase is due to the system no longer needing to undergo dimerisation or primary nucleation until the system has built up enough fibrils for elongation and secondary nucleation to dominate, as the fibrils have been added and are present from the start.

Metal ions have also been reported to impact the fibrilisation process. While the dimerisation rate in the absence of metals has been measured to be approximately 10^2-$10^3\,\mathrm{M}^{-1}\,\mathrm{s}^{-1}$,[63] it has been estimated that in the presence of Cu^{2+} the dimerisation rate of Aβ is increased by more than two orders of magnitude.[64] However some

studies have reported that metals in fact inhibit aggregation. It has been reported that while metals may enhance the rate of aggregation the aggregates are not fibrillar in nature, but that in some cases these aggregates can go on to produce fibrils. This may explain some of the contradictory findings that have been reported. Studies investigating Aβ aggregation can also be hindered by the Aβ 'sample history' and particular experimental conditions used. Conclusions are further hampered by uncertainties over what exactly constitutes a small or large oligomer, a proto-fibril or mature fibril or 'seed', in what is a highly heterogeneous and dynamic Aβ 'soup'. Whatever their effect may be, it is clear that metals can interact with Aβ and have some effect on the aggregation of Aβ.

3.1.2 Coordination of copper to Aβ

Much research has been directed towards understanding the interaction between Aβ and Cu. It has been reported that Cu^{2+} can form a 1:1 stoichiometry complex with Aβ. A second Cu^{2+} has been shown to bind, but only when concentrations of copper are much higher.

The Aβ peptide is intrinsically disordered, that is to say it doesn't have a defined secondary structure. It has been proposed that binding of metal ions can induce more structure on the Aβ peptide, however several binding modes have been described for the Aβ-metal species and these binding modes are flexible and dynamic in nature. While Aβ can bind metal, it cannot be thought of as a traditional metalloprotein, as these usually have one well defined binding pocket and very high binding affinities (typically considered to be $K_d < 10^{-7}$ M but more commonly $\sim 10^{-12}$ M).[65,66]

EPR study has revealed the presence of two major $A\beta Cu^{2+}$ coordinations at physiological pH, which differ in their protonation state. The two conformations have been named Component I & II for the protonated and deprotonated species respectively. It has also been shown that the $A\beta Cu^{2+}$ complex has a square planar geometry, involving the first two amino acids and a further two histidine residues (Fig. 3.2).[67] It has been shown that Component I & II are in dynamic equilibrium with each other and that they interconvert on the hundreds of millisecond timescale.[64]

3.1.3 From where does the copper come?

While a range of dissociation constants for Cu^{2+} binding to Aβ have been reported (10 pM to 100 nM[68]) more recent reports are converging on a value of ~1 nM.[69] The concentration of free copper in blood plasma has been estimated to be ~300 nM,[70]

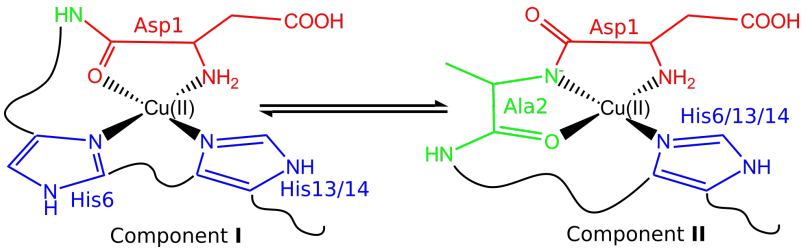


Figure 3.2 – $A\beta Cu^{2+}$ coordination. Square planar coordination environments for the two major species of the Cu^{2+} complex (Components I and II) present at physiological pH.[67]

while intracellular concentrations are considered to be negligible.[71] In the brain, concentrations of copper are expected to be hundreds of times lower than plasma levels,[72] and so, because of this low concentration within the brain, one might imagine that encountering a $A\beta Cu^{2+}$ complex would be unlikely. This unlikelihood of the $A\beta Cu^{2+}$ complex is compounded if we consider the copper dissociation constant of other abundant proteins, such as serum albumins ($\sim 7\,\text{pM}$), or copper transporter proteins such as ceruloplasmin (which can bind multiple copper ions with dissociation constants in the range $100\,\text{nM}$ - $10\,\mu\text{M}$). A question therefore arises: where in the body are copper concentrations high enough to complex with Aβ, and how can Aβ compete with other copper binding proteins that, in most cases, highly outnumber it?

The answer: within the synapse of neurons. During neuronal transmission copper is transiently released within the synaptic cleft. Values for the concentration of copper within the synaptic cleft have been reported to be $\sim 15\,\mu\text{M}$.[73,74] This concentration is well above the basal levels of copper in the brain, and is above the K_d for Aβ and so thermodynamically Aβ could bind Cu^{2+} at these concentrations.

The situation is slightly more complicated due to the transient nature of the copper release. While concentrations can get relatively high, the concentration will rapidly decrease as the copper can diffuse out of the cleft, be re-absorbed by the synapse or be complexed by other proteins present. Therefore, in order for the $A\beta Cu^{2+}$ complex to form, not only must the concentration of Cu^{2+} be higher than the K_d, but the Aβ peptide must be fast enough to bind the Cu^{2+} before another protein can, i.e. Aβ must be able to kinetically compete for Cu^{2+}.

The kinetics of the Aβ and Cu^{2+} interaction has been described in detail. It was found that Aβ binds copper with a very fast rate of binding, k_on $5.0(3) \times 10^8\,\text{M}^{-1}\,\text{s}^{-1}$ (approaching diffusion limited kinetics, $10^9\,\text{M}^{-1}\,\text{s}^{-1}$).[64] The rate of dissociation

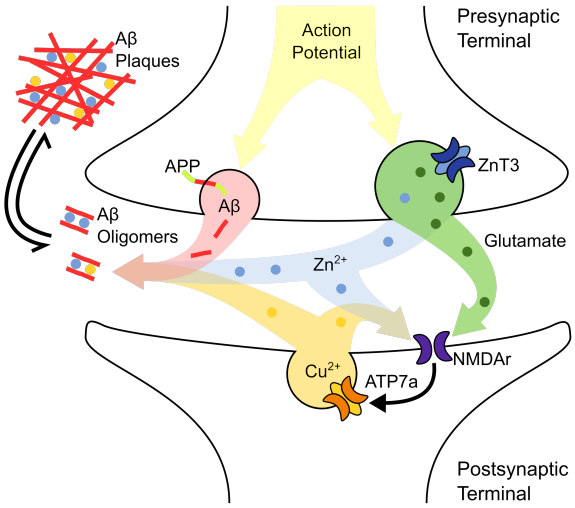


Figure 3.3 – The potential site of Aβ-metal interactions. Zinc and copper are transiently released into the synaptic cleft during neurotransmission. Here metal concentrations reach high enough levels such that that can bind to any Aβ present. Binding of metals may make the formation of Aβ oligomers easier. The oligomers of Aβ, through secondary nucleation and fragmentation, eventually become Aβ plaques, one hallmark of Alzheimer's disease

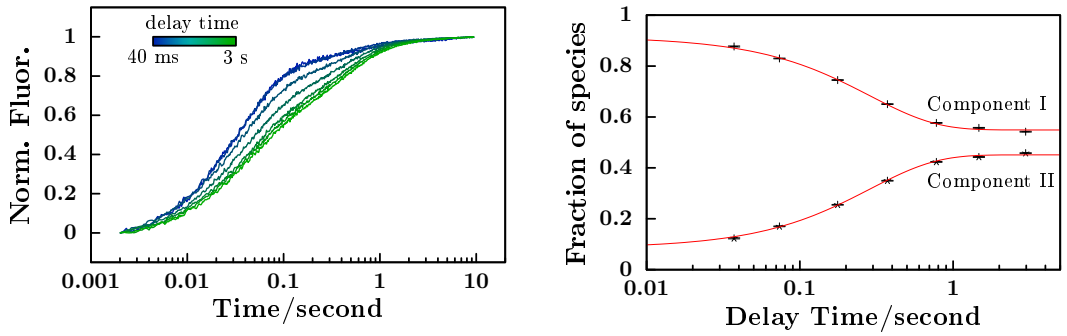
was shown to be, k_{off} $0.6(2)\,\text{s}^{-1}$ resulting in the complex having a lifetime of $1.7(6)$ second.[64] This suggests that Aβ would be successful in kinetically outcompeting serum albumin for copper, although the stronger affinity between serum albumin and copper would eventually result in the sequestering of copper away from the Aβ peptide.

Through kinetic analysis it has also been determined that when Cu^{2+} initially binds to Aβ it binds in a Component I coordination complex (Fig. 3.2), before interconverting to Component II. The two conformations were also shown to not be static, instead the Cu^{2+} could dynamically shuttle between the two conformations on the hundreds of millisecond timescale. Interestingly the Component II conformation was shown to be much more resistant to Cu^{2+} dissociation compared with Component I, and that in general the Component II complex was much more 'inert' to reactions with other species than the Component I complex.

Because of this reported 'inert-ness' of the Component II vs. Component I complex, the interconversion of the two species could be important for the understanding of the peptide's interactions and how they relate to disease. To further understand the kinetics of this interconversion, I set out to build upon what has already been reported by measuring the activation energy of the Component I & II interconversion.

3.2 Activation energy of interconversion

To determine the activation energy of $A\beta Cu^{2+}$ interconversion a double mixing stopped flow approach was employed. First fluorescently labelled Aβ was mixed with Cu^{2+} forming the $A\beta Cu^{2+}$ complex which resulted in a quenching of the fluorescence. The fluorescence is quenched due to the paramagnetic nature of the now nearby Cu^{2+} ion. The copper concentration was chosen such that binding would be completed within the dead time of the instrument. After a variable delay time EDTA was added to chelate the Cu^{2+} from the complex, in essence 'quenching' the interconversion and giving a recovery of fluorescence. Fig. 3.4(a) shows such a double mixing stopped flow trace. Each trace can be seen to be biphasic, with differing amplitudes depending on the delay time between complex formation and addition of EDTA. This changing amplitude is interpreted as the conversion of Component I (which is initially how Cu^{2+} binds to Aβ) to Component II (which is more resistant to chelation by EDTA).



(a) Double mixing stopped flow traces

(b) Fitted relative amplitudes

Figure 3.4 – Kinetics of Aβ/Cu interactions probed by double mixing stopped flow. (a) Aβ (100 nM) was initially mixed with Cu^{2+} (2 µM) (1:1 volume) and then after a variable delay time (given in colourbar) with EDTA (400 µM) (1:1 volume) at 298 K pH 7.5. (b) Time dependent evolution of the fractions of the two Components of $A\beta Cu^{2+}$ after formation, determined from global fitting of the data in (a) with shared rates, and plotting the relative amplitudes of the two phases present. The relaxation rate constant ($k_{1\to2}+k_{2\to1}$) is determined to be 3.5(1) s^{-1}.

By globally fitting the data in Fig. 3.4(a) to the sum of two exponentials while sharing the rates, the changing amplitude across different delay times can be extracted. This is plotted in Fig. 3.4(b). This shows that at very short delay times, just after complex formation, $A\beta Cu^{2+}$ is mostly in the Component I conformation, but this rapidly interconverts to Component II. At longer delay times an equilibrium between Component I & II is reached where ~65 % is Component I.

By fitting Fig. 3.4(b) with an exponential we can determine the observed rate

of relaxation of the system ($k_{\mathrm{r}}^{(\mathrm{obs})}$ 3.5(1) s^{-1}) which corresponds to the sum of the microscopic rate constants of interconversion ($k_{1\to2} + k_{2\to1}$).

The individual microscopic rate constants of interconversion can also be extracted from the data fitting. If we consider that interconversion is the only process occurring we can write it as,

$$[\mathrm{I}] \underset{k_{2\to1}}{\overset{k_{1\to2}}{\rightleftharpoons}} [\mathrm{II}] \tag{3.1}$$

As the system starts entirely as Component I before interconverting to Component II we know that the sum of the two Components at any time must equal the concentration of Component I at t=0 ($[\mathrm{I}]_0$), and therefore at equilibrium we can write the following expression,

$$[\mathrm{I}]_{\mathrm{eq}} + [\mathrm{II}]_{\mathrm{eq}} = [\mathrm{I}]_0 \tag{3.2}$$

where $[\mathrm{I}]_{\mathrm{eq}}$ and $[\mathrm{II}]_{\mathrm{eq}}$ are the equilibrium concentrations of Component I and II respectively. At equilibrium the forward and reverse reactions must equal each other.

$$k_{1\to2}[\mathrm{I}]_{\mathrm{eq}} = k_{2\to1}[\mathrm{II}]_{\mathrm{eq}} \tag{3.3}$$

By substituting Eq. 3.2 into Eq. 3.3 and using the fact that $k_{\mathrm{r}}^{(\mathrm{obs})} = k_{1\to2} + k_{2\to1}$ we can obtain the following expression.

$$k_{\mathrm{r}}^{(\mathrm{obs})}[\mathrm{I}]_{\mathrm{eq}} = k_{2\to1}[\mathrm{I}]_0 \tag{3.4}$$

As we plot the relative amplitudes of the two species, we can set $[\mathrm{I}]_0$ to 1, and from the fitting obtain $k_{\mathrm{r}}^{(\mathrm{obs})}$ and $[\mathrm{I}]_{\mathrm{eq}}$ and thus determine $k_{2\to1}$ and similarly $k_{1\to2}$.

The interconversion of Components I & II of the AβCu^{2+} complex is characterised by a change in protonation state (Eq. 3.5), we can therefore use the Henderson-Hasselbalch equation (Eq. 3.6) along with our newly obtained microscopic rate constants and calculate the pK_{a} of interconversion.

$$(\mathrm{A}\beta\mathrm{Cu}^{2+})_{\mathrm{I}} \underset{k_{2\to1}}{\overset{k_{1\to2}}{\rightleftharpoons}} (\mathrm{A}\beta\mathrm{Cu}^{2+})_{\mathrm{II}} + \mathrm{H}^{+} \tag{3.5}$$

$$\mathrm{pH} = \mathrm{p}K_{\mathrm{a}} + \log_{10}\frac{k_{1\to2}}{k_{2\to1}} \tag{3.6}$$

Taking the values for the interconversion determined from the fitting of Fig. 3.4(b) and using the Henderson-Hasselbalch equation, a value for the pK_{a} of 7.59(3) can be

determined for the interconversion of the AβCu^{2+} complex. This compares well with the reported literature value of 7.7.

Comparisons with a mouse

The murine Aβ (mAβ) peptide contains three mutations compared to the human peptide: Arg5Gly, Tyr10Phe & His13Arg. All of these mutations occur within the first 16 residues of the peptide, that is the region recognised as having the ability to bind metals. The lack of one of the three histidine molecules would lead one to expect that Cu^{2+} binding might be different between the human and murine peptides. Indeed it has been shown that the coordination of the Aβ peptide to Cu^{2+} does differ between the human Aβ (hAβ) and murine variants, and that it is the change from arginine in position 5 to glycine that is the predominant driving force behind these differences. Fig. 3.5 shows the coordination environments for the two Components of the mAβCu^{2+} complex present at physiological pH, (c.f. the hAβCu^{2+} complex Fig. 3.2).[75]

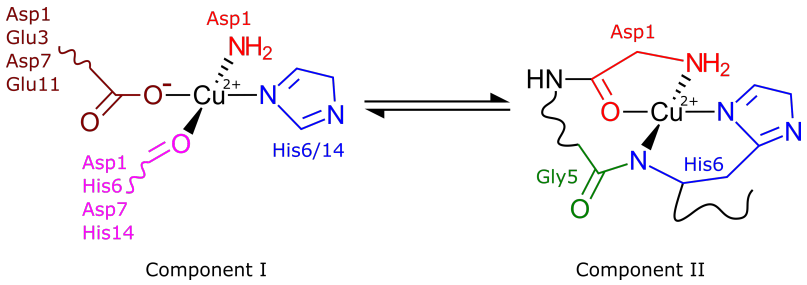
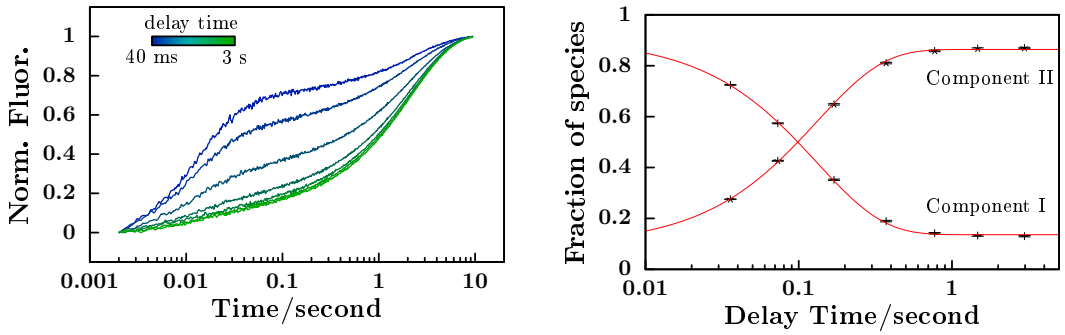


Figure 3.5 – Murine AβCu^{2+} coordination. Square planar coordination environments for the two major species of the mAβCu^{2+} complex (Components I and II).[75]

In addition to the mutations present in the murine Aβ peptide impacting the coordination of the peptide to Cu^{2+}, it also affects the kinetics of the interaction. While the Cu^{2+} association rate constants are fairly similar, the dissociation rate constant for mAβ is slower, resulting in a slightly tighter mAβCu^{2+} complex. However, the main difference between the human and murine Aβ peptides is their pK_a. The murine Aβ peptide has a reported pK_a 6.2, much lower than that of hAβ. As a result, at physiological pH Component II will be the dominant species for the murine peptide, contrasting with the human case. As our double mixing stopped flow approach reports on interconversion, we would expect to observe a difference between the murine and human Aβ peptides.

Fig. 3.6 shows an analogous double mixing experiment as described above, but



(a) Double mixing stopped flow traces

(b) Fitted relative amplitudes

Figure 3.6 – Kinetics of mAβ/Cu interactions probed by double mixing stopped flow. (a) murine Aβ (100 nM) was initially mixed with Cu^{2+} (2 µM) (1:1 volume) and then after a variable delay time with EDTA (400 µM) (1:1 volume) at 298 K pH 7.5. (b) Time dependent evolution of the fractions of the two Components of murine $A\beta Cu^{2+}$ after formation, determined from global fitting of the data in (a) with shared rates, and plotting the relative amplitudes of the two phases present. The relaxation rate constant ($k_{1\rightarrow2}$+$k_{2\rightarrow1}$) was determined to be 7.3(2) s^{-1}.

using the murine Aβ peptide rather than the human. The differences are clearly visible with the slower phase dominating at longer delay times. Fitting of the relative amplitude data in Fig. 3.6 with a single exponential gives the observed rate of relaxation to be, $k_{r(obs)}$ 7.3(2) s^{-1}. From the fitting of Fig. 3.6, the pK_a can be calculated as 6.69(2). While this value is higher than reported literature values, it is still lower than that calculated for hAβ (7.59(3)).

In addition to calculating the pK_a of interconversion, the relaxation experiments also allow us to determine the equilibrium constant (K_{Eq}) for interconversion. From this we can determine thermodynamic properties such as the Gibbs energy by using,

$$\Delta G^o = -RT \ln(K_{Eq}) \tag{3.7}$$

By measuring the rate of relaxation at various temperatures, we can see how the Gibbs energy varies over temperature (Fig. 3.7a). By fitting with a straight line, and using the relation $\Delta G^o = \Delta H^o - T\Delta S^o$, the entropy ($\Delta S$) of interconversion can be estimated to be 31(14) J mol^{-1} K^{-1} for human $A\beta Cu^{2+}$ and 55(12) J mol^{-1} K^{-1} for murine $A\beta Cu^{2+}$.

An Arrhenius plot can also be obtained from measuring the rate of relaxation at various temperatures (Fig. 3.7b). From this the activation energy, E_a, of interconversion can be calculated by,

$$k = A\mathrm{e}^{-E_a/(RT)} \tag{3.8}$$

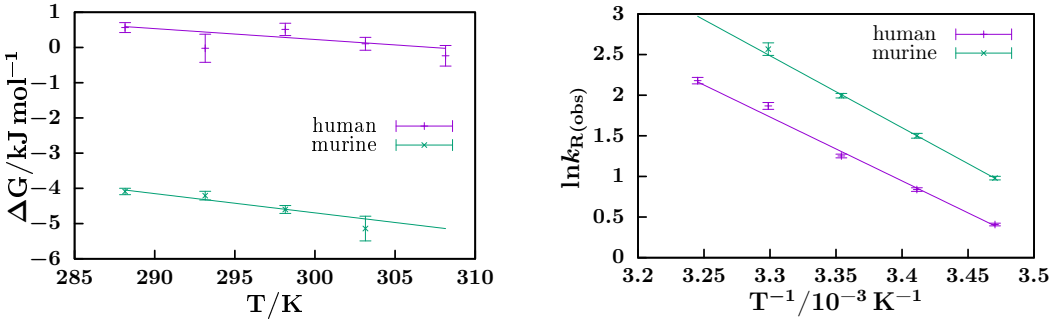
which can be rearranged to give a straight line plot as,

$$\ln(k) = \ln(A) - \frac{E_a}{R}\frac{1}{T} \tag{3.9}$$

where k is the rate, A is the pre-exponential factor, R is the universal gas constant and T is the absolute temperature. While an Arrhenius plot is useful for determining the activation energy for reactions that happen in the gas phase, for reactions in the condensed phase Arrhenius theory can fail to account for the physical properties of the reaction medium. Indeed, activation energies can even vary with temperature for reactions that occur in solution.[76] The experimentally determined activation energies below may be better described as the enthalpy of the reaction.

The temperature dependence of the interconversion reaction does however appear to be linear (Fig. 3.7b), at least over the temperature range studied. Using the gradient and Arrhenius theory, the activation energy for the interconversion of the human and murine peptides can be calculated to be 65(3) kJ mol^{-1} and 73(2) kJ mol^{-1} respectively.

The activation energy for interconversion between AβCu^{2+} Component I & II (for both human and murine) is quite large, suggesting that a sizeable energy penalty is incurred to undergo the coordination rearrangement. The activation energy barrier for interconversion of the murine peptide is slightly larger than that of human,



(a) Gibbs energy of interconversion

(b) Arrhenius plot of interconversion

Figure 3.7 – Thermodynamics of interconversion of human and murine AβCu^{2+} complexes. (a) Gibbs energy varies slightly with temperature. (b) Arrhenius plot for interconversion. Activation energies calculated to be 65(3) kJ mol^{-1} and 73(2) kJ mol^{-1} for the human and murine peptides respectively.

even though the interconversion rate for the murine peptide is faster than the human peptide. This is due to the markedly large difference in the pre-exponential factor, which is much higher in the murine case ($59(1) \times 10^{12}$ vs $1.1(5) \times 10^{12}$). The difference in the pre-exponential factor could possibly be due to the differences in the sequence near the copper binding residues. In particular the human sequence contains an Arg5 beside the copper binding His6, whereas the murine sequence replaces the Arg5 with a Gly5 creating much less steric bulk around the coordinating ligand. Caution must be exercised when ascribing meaning to the pre-exponential factor for reactions that occur in solution, as it will not be the rate of collision usually encountered for gas phase reactions. The values determined here are very large and unphysical for reactions occurring in solution, also suggestive of a problem in applying Arrhenius theory to this reaction. However, comparisons between the values determined for human and murine AβCu^{2+} complexes should still be valid.

It is worth noting that in the activation energy experiments the change in buffer pK_a upon changing temperature was not corrected for. HEPES has a relatively small temperature coefficient, and so over the 15 °C to 35 °C range of the experiment, the pH is expected to deviate by a total of ∼0.3 pH units. As the interconversion of AβCu^{2+} involves protonation, a stable pH is important. The Arrhenius plot in Fig. 3.7 appears linear, and so the slight deviation in pH does not seem to affect the results.

3.3 AβCu^{2+} kinetics for Familial Alzheimer's disease mutations

Familial Alzheimer's disease, (FAD) is a subset of early-onset Alzheimer's disease, where an individual has an inheritable mutation that causes the onset of clinical symptoms earlier in life (under the age of 65). While FAD only accounts for a small proportion of Alzheimer's disease (AD) cases, it is regarded as a useful system to study, in order to help better understand the disease as a whole.[47] The autosomally dominant mutations causative of FAD have been identified in three proteins related to Aβ production: presenilin-1 & -2, and amyloid precursor protein (APP). FAD mutations that have been identified in the amyloid precursor protein are shown in Fig. 3.8. An extensive review of these FAD mutations can be found by Weggen & Beher,[47] but to summarize, most of these mutations cause either an aberrant increase in the production of Aβ or alter the ratio of Aβ40/42. This alteration in Aβ is used as the rationale behind developing AD earlier in life. Many of the

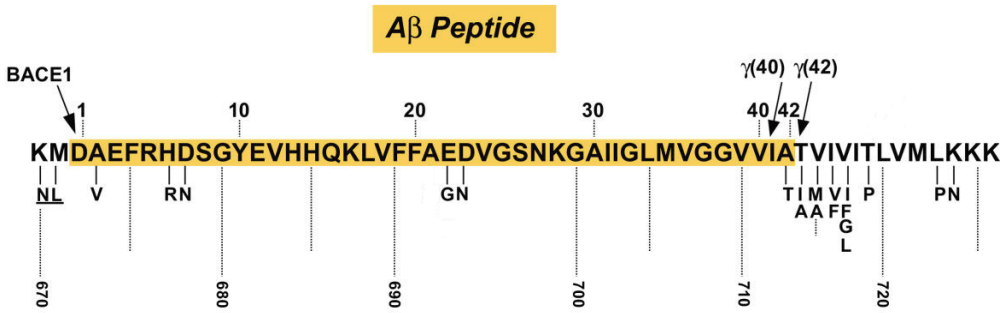


Figure 3.8 – Familial Alzheimer's disease mutations within the amyloid precursor protein. The amino acid sequence of part of the amyloid precursor protein is shown with mutations that have been linked to causing FAD shown below the original amino acid residue. The region highlighted in yellow will form the Aβ peptide after cleavage by β- (BACE1) and γ-secretase (cleavage sites indicated by arrows). Adapted with permision from Weggen & Beher under a Creative Commons Attribution License.[47]

APP mutations occur at or around either the β-secretase or, more commonly, the γ-secretase cleavage sites, and as such an aetiology involving altered cleavage is likely. However some mutations, such as the English (H6R, age of onset 55 years)[77] and Tottori (D7N, age of onset 60 years)[78] substitution mutations lie distal from the cleavage sites, and ultimately end up in the metal binding region of the Aβ peptide. Consequently, a different mechanism, perhaps related to the peptide's interactions with Cu^{2+}, may account for developing AD from these particular FAD mutations.

In vitro studies of Aβ40 and Aβ42 peptides incorporating either the H6R or the D7N mutations have shown that the two mutations do not affect the production of Aβ, but alter Aβ assembly at its earliest stages, as well as monomer folding and oligomerisation processes.[79,80] Experimental work using ion mobility-based mass spectrometry indicated that structural changes present in the monomers are reflected in the oligomers.[81] Molecular dynamics simulations have also shed light on how the mutations affect the peptides' properties. For H6R the reduction in the net charge was found to be a major contributor in enhancing aggregation, but also that the mutation caused an increase in hydrophobicity, compounding the issue.[82] For the D7N peptide, it was shown that this mutation changed the fold and salt bridge network within the peptide.[83] Furthermore, these mutations can significantly increase the solvation free energy and thus enhance the aggregation of Aβ monomers.[84]

As the H6RAβ mutant lacks histidine 6 (one of the amino acids that coordinates to the Cu^{2+} centre in the wild-type peptide), a slightly different binding motif has been described (Fig. 3.9).[85] The D7NAβ mutant has been reported to have the

same coordination as the wild-type Aβ (Fig. 3.2).[85]

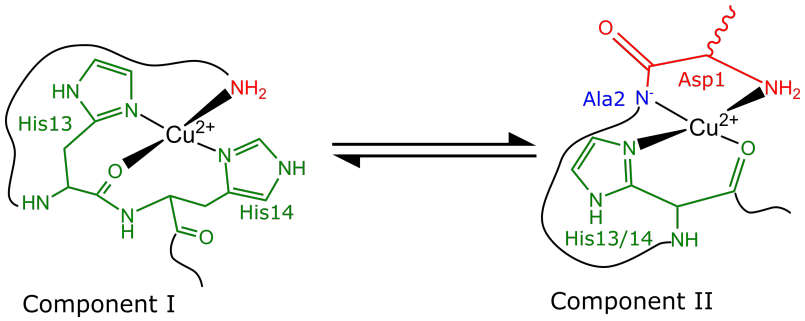


Figure 3.9 – H6RAβCu^{2+} coordination. Square planar coordination environments for the two major species of the H6RAβCu^{2+} complex (Components I and II) at physiological pH.[85]

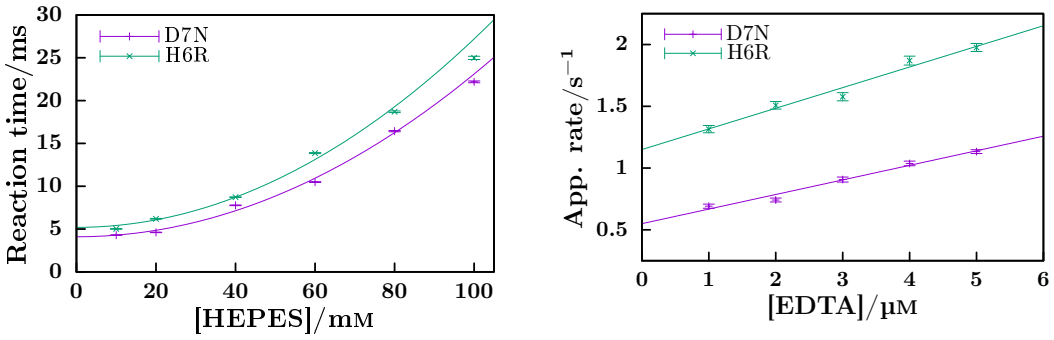
The kinetics of Cu^{2+} Aβ interactions have been solved and described in detail for the wild-type Aβ (wt-Aβ) peptide.[86] Here, this work is extended to include the Aβ H6R and D7N FAD mutants to see if chemical kinetics can shed light on why these mutants predispose one to developing Alzheimer's disease earlier in life.

Binding and dissociation kinetics

* To study the kinetics of the FAD-Aβ Cu^{2+} interaction, the binding and dissociation rate constants were measured. By rapidly mixing fluorescently labelled Aβ with Cu^{2+} we can follow the reaction progress as the Cu^{2+} quenches the fluorescence. HEPES is known to have a weak association with Cu^{2+} and so the rate constant was measured under various HEPES concentrations such that extrapolation to zero could yield the buffer independent Cu^{2+} binding rate constant (Fig. 3.10(a)). Data was empirically fitted with a parabola centred at zero and the intercepts were used to calculate the association rate constants, k_{on} $4.8(3) \times 10^8\,\mathrm{M}^{-1}\,\mathrm{s}^{-1}$ and $6.1(3) \times 10^8\,\mathrm{M}^{-1}\,\mathrm{s}^{-1}$ for H6R and D7N respectively. These values are very close to the association rate constant determined for the wild-type Aβ peptide (k_{on} $5.0(2) \times 10^8\,\mathrm{M}^{-1}\,\mathrm{s}^{-1}$) previously reported. This suggests that the FAD mutations have little impact on the rate of Cu^{2+} binding.

To determine the dissociation rate constant, the FAD-AβCu^{2+} complex was pre-formed and then reacted with EDTA (Fig. 3.10(b)). Extrapolation to zero EDTA concentration reveals the apparent dissociation rates to be, k_{off} $1.15(5)\,\mathrm{s}^{-1}$ and $0.55(3)\,\mathrm{s}^{-1}$ for H6R and D7N respectively. The second order rate constants for

*The association & dissociation data was collected by Toru Miyake, data was analysed by P.G.



(a) association reaction

(b) dissociation reaction

Figure 3.10 – Association and dissociation rate of Cu^{2+} with Aβ bearing the H6R or D7N familial Alzheimer's disease mutation. (a) The timescale for the binding of Cu^{2+} (400 nM) to Aβ (20 nM) at various HEPES concentrations. Empirically fitted with a parabola. (b) Apparent dissociation reaction rate of the AβCu^{2+} complex (50 nM) for various concentration of EDTA. All experiments performed in HEPES pH 7.5 at 298 K.

the reaction with EDTA were calculated from the gradient to be $1.7(2) \times 10^5\,\mathrm{M^{-1}\,s^{-1}}$ and $1.3(2) \times 10^5\,\mathrm{M^{-1}\,s^{-1}}$ respectively. This is more than twice the reported value for the wild-type Aβ ($0.55(3) \times 10^5\,\mathrm{M^{-1}\,s^{-1}}$).

Dimerisation kinetics

* As a measure of dimerisation rate, the effect of the FAD mutations on the formation of a AβCu^{2+}Aβ ternary complex was determined. FAD-AβCu^{2+} complex was pre-formed and then reacted with unlabelled Aβ40 containing the same FAD mutation, (Fig. 3.11). The rate constants determined for this reaction were $1.8(1) \times 10^5\,\mathrm{M^{-1}\,s^{-1}}$ and $1.96(9) \times 10^5\,\mathrm{M^{-1}\,s^{-1}}$ for H6R and D7N respectively. This is ∼50 % faster than that reported for the wild-type Aβ ($1.22(8) \times 10^5\,\mathrm{M^{-1}\,s^{-1}}$).

The fitted lines in Fig. 3.11 can also be extrapolated to zero Aβ40 concentration to get a value for the apparent dissociation rates, in an analogues way to Fig. 3.10(b). However, it can be seen that the intercepts in Fig. 3.11 are ∼25 % greater than in 3.10(b). This alludes to a error in the determination of the ligand concentration (most likely an error in the Aβ40 concentration). The error in concentration will be systematic so while it will have an impact on the intercept, the gradient (i.e. measure of dimerisation rate) will not be impacted.

In this experiment, the ability of a molecule of Aβ to be able to extract the

*The dimerisation data was collected by Toru Miyake, data was analysed by P.G.

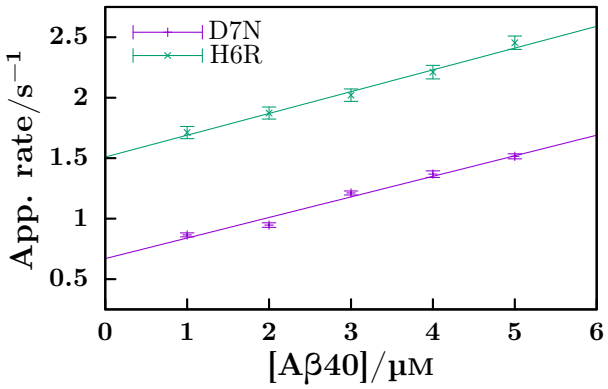


Figure 3.11 – Ternary complex kinetics of FAD Aβ. Kinetics of FAD mutant AβCu^{2+} complex (50 nM) reacting with Aβ40 bearing the same mutation. All experiments performed in HEPES pH 7.5 at 298 K.

Cu^{2+} from the AβCu^{2+} complex is being used as an indicator as to how fast a copper bridged Aβ dimer could form. This is due to the fact that to be able to extract the copper from the complex, the uncomplexed Aβ has to first bind and form a AβCu^{2+}Aβ ternary complex. It should be noted however that, under the pseudo-first order reaction conditions that these experiments are carried out (where the concentration of AβCu^{2+} is in the nM regime and near physiological pH), this copper bridged Aβ dimer does not appear to be well populated as the fluorescence quenching is almost completely recovered. This suggests that the rate of dissociation of the AβCu^{2+}Aβ complex is much faster than its formation. As a result, the rate measured here could be interpreted as the rate of copper exchange between Aβ ligands.

3.4 Summary

Following on from a prior kinetic description of the interactions between Aβ and Cu^{2+},[86] I have built upon this work and further explored these interactions. By measuring the activation energy for the interconversion between Components I & II, I have shown that there is a barrier of ∼26 k_BT between the two major AβCu^{2+} binding motifs present at physiological pH. As well as determining the activation energy for human Aβ, the murine peptide was also studied.

Perhaps counter-intuitively, the murine peptide has a higher activation energy of switching compared to the human peptide, even though switching takes place faster for murine Aβ. This can be ascribed to the marked difference in the pre-exponential term of the Arrhenius equation. The difference in the pre-exponential factor could

be due to differences in the sequence of the murine Aβ near the copper coordinating residues. In particular the human sequence contains and Arg5 beside the coordinating His6, whereas the murine peptide replaces Arg5 with Gly5. This replacement of Arg with Gly would create much less steric bulk around the coordinating residue.

Drawing comparisons between the human and murine Aβ peptides can be of great use to try and understand Alzheimer's disease. It has been noted that mice do not normally present typical signs of AD such as Aβ accumulation as fibrils or plaques, and that they only do so when they are transgenically made to overexpress large amounts of the human Aβ peptide. Of course, some have explained this lack of AD pathology simply due to the fact that mice do not live long enough for AD symptoms to appear in non-transgenic mice. Regardless, others remain sceptical of using transgenic mouse models to study AD where both the human and murine Aβ peptides will both be expressed.[75] It is interesting to note the marked differences in the kinetics of human and murine Aβ with Cu^{2+}, especially regarding the differences in interconversion and the differences in the ratio of the Component I & II forms at physiological pH, and raises the question: could these kinetic differences be the driving factor behind the disease?

This chapter also explored the kinetics between copper and two Amyloid-β mutants linked to familial Alzheimer's disease. Studying FAD mutations and comparing them with sporadic AD can be extremely useful for understanding the disease as a whole, and has been used by others to do so.[87] Of the two mutations studied here, neither appeared to have a strong effect on the rate of copper binding to Aβ, even (surprisingly) in the case of the English mutation which lacks His6, a key coordinating residue in the wild-type Aβ copper binding. In contrast, the dissociation rate does appear to be affected by these two FAD mutations studied. As a result the equilibrium dissociation constants of the $A\beta Cu^{2+}$ complexes are, K_d 2.1(2) nM and 0.58(4) nM for H6R and D7N respectively (cf. wt-Aβ K_d 1.1(1) nM).

Taking the association and dissociation rate constants together, we can make inferences about the way Cu^{2+} binds to Aβ. As the replacement of His6 with Arg does not have an impact on the association rate of Cu^{2+}, this suggests that initial copper binding does not go via this residue. However, the H6R-Aβ mutant does have a higher dissociation constant, suggesting that the presence of His6 is required for tighter binding of the $A\beta Cu^{2+}$ complex.

Perhaps the most interesting finding regarding the interactions of copper with FAD-Aβ is that the second order rate constants for the interaction of the $A\beta Cu^{2+}$ complex with another molecule of Aβ is ∼50 % faster for the FAD mutants than the wt-Aβ peptide. Here I infer that this is a measure of the ability to form a copper

bridged Aβ dimer, however it could also be interpreted at the rate of copper exchange between Aβ ligands. While it is not clear if copper-bridged Aβ dimer formation is the kinetic determinant of Aβ aggregation,[88] it has been proposed that both the copper bound Aβ monomer and the copper bridged Aβ dimer are both on-pathway intermediates towards aggregation.[89,90] Furthermore, through the use of atomic force microscopy, Cu^{2+} has been shown to act as a bridge between Aβ molecules, greatly enhancing the stability of the complex.[91]

Finally it is interesting to note that while the thermodynamic dissociation constants determined for the FAD-AβCu^{2+} complex do not correlate well with the earlier age onset of AD, the kinetic measurements of the copper assisted Aβ dimerisation do. This suggests that in a highly heterogeneous and dynamic system, such as the synapse of a neuron, kinetics could be the determinant for the roles of the Aβ-metal interaction, rather than thermodynamics.

Chapter 4

Redox of the Amyloid-β Copper Complex

4.1 Reactive oxygen species generation of the AβCu complex

In Chapter 3 the kinetics of the interactions of Aβ with Cu^{2+} were explored in relation to the amyloid cascade hypothesis. As was discussed, metals have been shown to have an impact on the aggregation of Aβ and in Chapter 3 I presented data showing that Aβ containing familial Alzheimer's disease mutations showed an increased rate for formation of a ternary AβCu^{2+}Aβ complex compared with wild-type Aβ. If ternary complex formation is on pathway to oligomerisation, this result has potentially highlighted a shared kinetic origin for the oligomerisation of Aβ in familial and sporadic Alzheimer's disease (AD).

However, the amyloid cascade hypothesis, and the oligomerisation of Aβ in general, is not the only place where metals have been observed to have a potential role in Alzheimer's disease. The binding of Aβ to transition metal ions, and in particular redox active ions such as Cu or Fe, has led to the hypothesis that redox cycling of the Aβ-metal complex may be linked to the progression of Alzheimer's disease.

It has been suggested that the redox cycling of the Aβ-metal complex is able to generate reactive oxygen species (ROS), with similarities often drawn between the Aβ-metal complex and the transition metals at the centre of the Fenton and Haber-Weiss mechanisms (Fig. 4.1).[92,93]

Up to now I have mainly discussed the AβCu complex where the Cu is in the 2+ oxidation state. However, to discuss redox cycling of the AβCu complex, the AβCu

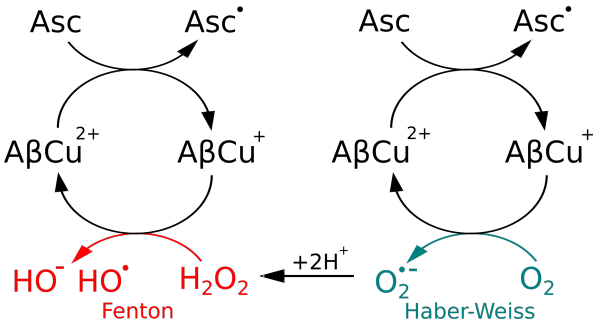


Figure 4.1 – Redox cycling of AβCu. Redox cycling of the AβCu complex can generate damaging reactive oxygen species through mechanisms similar to the Fenton and Haber-Weiss mechanisms. Here ascorbate (Asc) acts as the reducing agent, while molecular oxygen and hydrogen peroxide act as the oxidant.

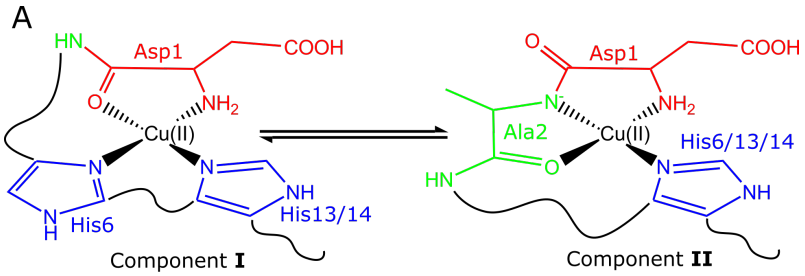


Figure 4.2 – Coordination of the AβCu$^+$ complex. (A) Square planar coordination environments for the two major species of the Cu^{2+} complex (Components I and II). (B) Linear coordination of the AβCu$^+$ complex.[67,94]

complex where the Cu is in the 1+ oxidation state will also need to be considered. To briefly summarise what was disused in Section 3.1.2, Aβ binds to Cu^{2+} with a low nM K_d, the AβCu^{2+} complex adopts a square planar geometry involving a combination of the first two amino acids and up to two histidine ligands, and at physiological pH there are two major AβCu^{2+} coordinations that dynamically interconvert.

By comparison the AβCu$^+$ complex shows a linear geometry, involving mostly coordination from His13 and His14, with minor species involving His6 and either His13/14 (Fig. 4.2).[94] It has also been reported that the AβCu$^+$ complex has a similar K_d to the AβCu^{2+} complex.[95]

Many in vitro studies have shown that the AβCu complex can generate ROS when in the presence of a reducing agent.[96] In the AD brain the plaques formed of Aβ are found in an oxidised form, and in general a large amount of oxidative damage (to proteins, lipids and nucleic acids) is also observed.[97,98,99] These two observations suggest at a strong link between Aβ-metal generated ROS and the large amount of oxidative damage that is found within the AD brain.

Oxidative damage by ROS, potentially catalysed by Aβ, is not the only result of redox cycling of the Aβ-metal complex. This redox cycling may also play a role in oligomerisation of the Aβ molecule itself. Redox cycling of the Aβ-metal complex has been noted to modify the Aβ peptide itself. One of these modifications could be the formation of a tyrosine radical, leading to di-tyrosine crosslinking and the generation of a stable covalently bonded Aβ dimer.[100] Di-tyrosine Aβ dimers have been observed in the AD brain originally by an immunohistochemical approach, and then more recently confirmed via mass spectrometry analysis of AD brain samples.[101,102]

While many suggest that Aβ-metal generated ROS could be a route to AD, there are some suggesting that Aβ is an anti-oxidant, rather than a pro-oxidant. Pedersen et al. note that ROS generation by Cu^{2+} is slower when complexed with Aβ or present in oligomeric/fibrillar Aβ, than 'free' Cu^{2+}.[103] While this observation is perhaps somewhat obvious, it is not necessarily evidence against the importance of AβCu generated ROS. The idea of 'free' copper within the body is also slightly misleading as any 'free' copper will quickly be complexed by proteins or amino acids present. To call Aβ an anti-oxidant also ignores the potential for localised damage that Aβ facilitated redox cycling can do, either to Aβ itself or to nearby membranes, this will be further explored in Chapter 5.

If ROS damage generated from the Aβ-metal complex is involved in the pathogenesis of Alzheimer's disease, we must strive to understand the reduction and oxidation steps involved. In particular, the kinetic mechanism must be known if we are to quantifiably address if the ROS production observed in vitro is happening on a timescale relevant to the disease -something which has received little attention to date. In this Chapter the redox kinetics of the AβCu complex is explored.

4.2 Measuring redox by directly monitoring the oxidation state of the metal ion

To measure redox cycling of the AβCu complex one could measure the rate of disappearance of the reactants (reducing or oxidising agents) or the formation of

products (ROS). Ascorbate (asc) has a strong UV-Vis signal so could be used to monitor the decrease in reducing agent; this has been reported in the literature where it was used to compare how various Aβ N-terminal modifications affected the AβCu turnover.[104] For the formation of reactive oxygen species, these can be detected via various fluorescent probes. Both of these methods however would study multiple turn over conditions of the AβCu complex, and determining a kinetic mechanism from such experiments would be difficult.

To be able to better follow the redox process we can monitor the change in the oxidation state of the metal ion itself. To do this I exploited the fluorescent quenching properties of Cu^{2+} in an analogous but subtly different way to that described in Chapter 3. If a fluorescently labelled Amyloid-β is used, upon binding to Cu^{2+} the fluorescence will be quenched. This quenching is due to the paramagnetic nature of the Cu^{2+} ion having one single unpaired electron. When the Cu^{2+} is reduced (gaining an electron) it no longer has an unpaired electron and the fluorescence of the labelled Aβ is recovered. We should therefore observe a recovery of fluorescence upon reduction of $A\beta Cu^{2+}$ to $A\beta Cu^{+}$, and as such have a system able to report on the oxidation state of the copper centre in the AβCu complex with a fluorescent readout.

In all the work that will follow in this chapter a truncated Aβ peptide that was fluorescently labelled at the C-terminus with HiLyte™Fluor 488 was used. This truncated Aβ consisted of the first 16 residues and is often employed as the model system of choice when studying Aβ metal interactions. The first 16 residues of Aβ contain the metal binding residues but crucially does not contain the hydrophobic C-terminal region which can cause peptide aggregation.

4.3 Titration of ascorbate to $A\beta Cu^{2+}$ complex

To determine if a fluorescence readout can be used to observe the change in oxidation state of the metal centre in the $A\beta Cu^{2+}$ complex, a titration fluorometer experiment was carried out. Labelled Aβ was mixed with Cu^{2+} in a 1:1 ratio before being reduced with ascorbate, (Fig. 4.3). This figure shows that upon reduction of the $A\beta Cu^{2+}$ complex from the paramagnetic Cu^{2+} to non paramagnetic Cu^{+} a recovery of the quenched fluorescence is observed. In this experiment buffers were degassed with N_2 prior to use, in order to minimise any potential for oxygen present in the buffer that might cause the complex to become reoxidised to Cu^{2+}.

From Fig. 4.3 it can also be seen that at higher concentrations of ascorbate the fluorescence begins to decrease again. This quenching was only apparent at higher

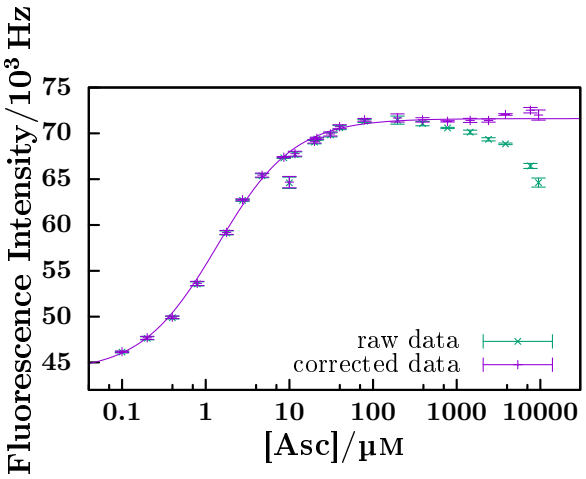


Figure 4.3 – Fluorescence of AβCu^{2+} is recovered upon reduction. Titration of ascorbate into 1 µM labelled AβCu^{2+}, showing data before and after correction due to collisional quenching (see section 4.3.1). Corrected trace is shown fit with a Hill function. Error bars represent standard deviation of three measurements.

concentrations of ascorbate when the concentration approached 1 mM or higher and was ascribed to collisional quenching. The nature of this quenching is explored further in Section 4.3.1.

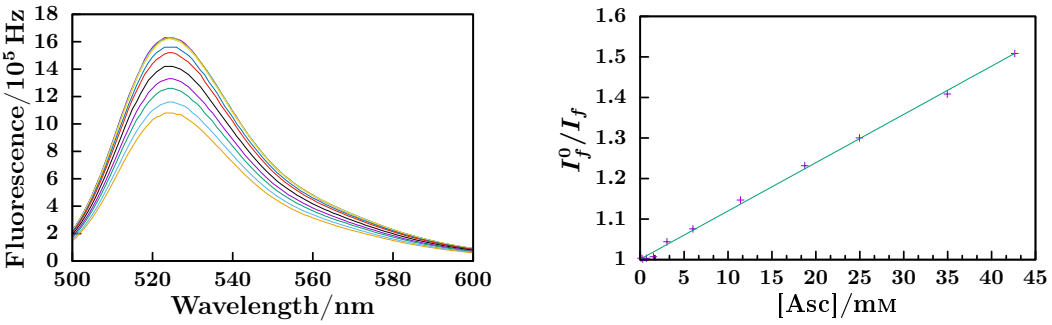
After correction for this ascorbate quenching, the corrected data in Fig. 4.3 was fit with a Hill Function and gave a concentration of 1.4(1) µM ascorbate required to bring about half the recovery of fluorescence.

4.3.1 Collisional quenching of the dye at high concentrations of ascorbate

To explore this quenching effect in more detail, labelled Aβ was mixed with increasing concentrations of ascorbate (asc) and the fluorescence spectra recorded, (Fig 4.4(a)). From this figure it can be seen that the fluorescence emission intensity decreases as a function of increased asc concentration.

Quenching of fluorescence intensity can occur for a number of reasons, but often it is due to a quenching molecule colliding with the fluorophore while the fluorophore is in the excited state, thus providing the excited fluorophore with a route to the ground state that does not involve emission of a photon. This can be represented by the equation:

$$F^* + Q \xrightarrow{k_q} F + Q \tag{4.1}$$



(a) Fluorescence Spectra

(b) Stern-Volmer plot

Figure 4.4 – Quenching of labelled Aβ by ascorbate. (a) Quenching of 500 nM labelled Aβ by ascorbate (0.1-43 mM). (b) Stern-Volmer plot of fluorescence data shown in (a).

where F* is the fluorescent species in the excited state, Q is the quencher, & k_q is the quenching rate constant. If we consider the fluorescence quantum yield, in the absence of quencher, as defined by the rate of excited state decay, which can be expressed as:

$$\Phi_f^0 = \frac{k_f}{k_f + k_{\text{nr}}} = \frac{k_f}{\frac{1}{\tau_0}} \tag{4.2}$$

where k_f is the rate constant of fluorescent emission, k_{nr} is the rate constant of all non-radiative processes, & τ_0 is the lifetime of fluorescence in the absence of quencher. This formula for quantum yield can be modified for when in the presence of quencher to give:

$$\Phi_f = \frac{k_f}{k_f + k_{\text{nr}} + k_q[Q]} = \frac{k_f}{\frac{1}{\tau_0} + k_q[Q]} \tag{4.3}$$

Finally by taking the ratio of quantum yield in the absence and presence of quencher, and substituting (the more easily measured) fluorescence intensity in place of quantum yield, the Stern-Volmer equation can be thus defined:

$$\frac{\Phi_f^0}{\Phi_f} = \frac{I_f^0}{I_f} = 1 + k_q\tau_0 \cdot [Q] \tag{4.4}$$

where I_f^0 is the fluorescence intensity in the absence of quencher, I_f is the intensity in the presence of quencher, k_q is rate constant of the quenching process, τ_0 is the fluorescence lifetime of the dye and [Q] is the concentration of quencher used.

By calculating I_f^0/I_f for the data presented in Fig. 4.4(a) and plotting it against

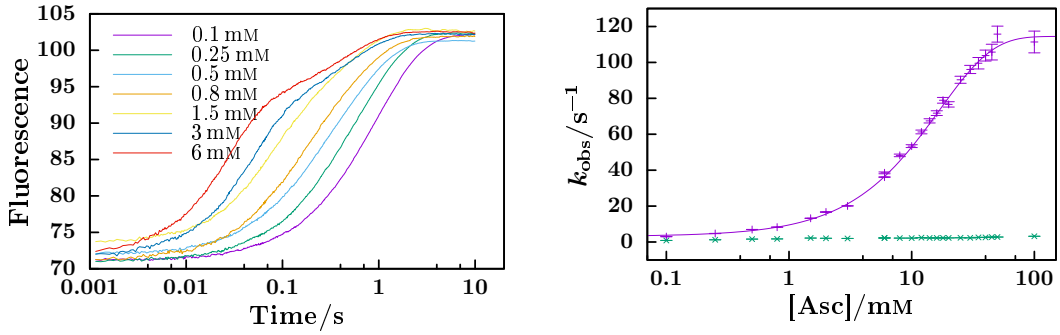
the ascorbate concentration we can obtain a Stern-Volmer plot, shown in Fig. 4.4(b). Fitting this Stern-Volmer analysis with a straight line gives the equation:

$$\frac{I_f^0}{I_f} = 1.001(3) + 11.9(1) \times \text{molar ascorbate concentration} \tag{4.5}$$

This equation is used to correct for quenching of the labelled Aβ fluorescence by ascorbate throughout this work.

4.4 Reduction kinetics of AβCu^{2+} by ascorbate

Having confirmed that the change from the AβCu^{2+} to AβCu^{+} species can be detected by monitoring the recovery of fluorescence, and having determined how to correct for the quenching of the fluorescence when in the presence of high concentrations of asc, I next moved onto studying the kinetics of the reduction step. For this a stopped flow approach was employed. In this experiment the AβCu^{2+} complex was first pre-formed before being rapidly mixed with various concentrations of ascorbate, while the fluorescence recovery was monitored as a function of time. In order to be as physiologically relevant as possible, the concentrations of the AβCu^{2+} complex were kept as low as possible while still remaining within the detection limits of the instrument (50 nM). The concentrations of ascorbate employed where chosen as the minimum concentration that gave a complete recovery of fluorescence, as determined by the titration experiment (see section 4.3), (ca. 100 µM).



(a) Stopped flow data

(b) Fitted rates

Figure 4.5 – Kinetics of AβCu^{2+} reduction by ascorbate. (a) Stopped flow data showing the recovery of fluorescence after mixing 50nM AβCu^{2+} with ascorbate (concentration given in key) in HEPES/NaCl at 298 K. Each trace is the average of seven repeats. (b) Rate of fast and slow phases against ascorbate concentration. Rates determined from exponential fitting of the raw data. Error bars display the uncertainty of the parameters derived from the fit of the raw data.

Typical experimental traces are shown in Fig. 4.5(a). The observed fluorescence recoveries are exponential in shape and get faster as the ascorbate concentration gets higher. When the concentration of ascorbate becomes sufficiently high, two phases become apparent in the fluorescent traces; a fast phase, which appears to continually get faster as higher concentrations of ascorbate are used, and a slow phase, the speed of which does not seem to change much with increasing ascorbate concentration. The fluorescent traces were fit to the sum of two exponentials to account for the two phases and the apparent rates of these exponentials are shown plotted against ascorbate concentration in Fig. 4.5(b). This figure clearly shows that while the rate of the fast phase increases as the ascorbate concentration is increased over three orders of magnitude, the slower phase shows no dependence on ascorbate concentration. Interestingly the fast phase displays an exponential dependence on ascorbate concentration (the data has been fitted with an exponential function to help guide the eye), indicative of a multi-step mechanism. At very high concentrations of ascorbate the reaction proceeds so fast that most of the fluorescence recovery occurs within the dead time of the instrument, making the fitting of these very fast kinetics unreliable, as indicated by the increased uncertainty in the fit.

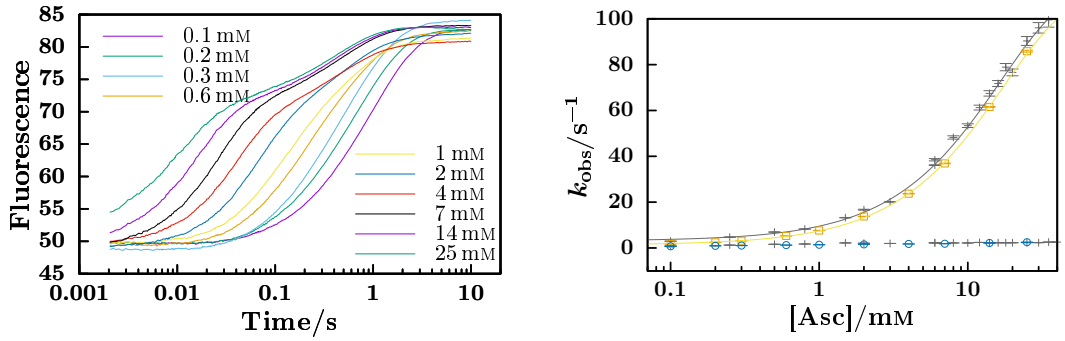
4.4.1 Comparison between HEPES and MOPS buffers

In the experiments that have been presented thus far the buffer system has been comprised of HEPES and NaCl. HEPES is one of the twenty 'Good's Buffers' and provides maximal buffering at physiological pH. Importantly for this research, it does not precipitate in the presence of divalent metal ions, which is not the case with more common buffers such as PBS and Tris. For this reason, experiments involving the use of ions such as Cu^{2+} and Zn^{2+} should avoid the use of PBS or Tris, and use a buffer that is more inert to these divalent metal ions.

Although HEPES is a good buffer choice when using metal ions, it has been noted that this buffer can form radicals, leading some to suggest that it should therefore not be used in the study of redox reactions. An alternative buffer, MOPS, is often employed as it does not form radicals and can still provide adequate buffering at physiological pH (although not as good as HEPES). For this reason I compared the rate of reduction carried out in HEPES buffer with the rate of reduction using MOPS as the buffer.

Fig. 4.6 shows a stopped flow study conducted analogously to that described in Section 4.4 but using MOPS buffer instead of HEPES. As can be seen there is no change in the rate of reduction in MOPS compared with HEPES, suggesting that

(at least on the timescale of our experiments) the formation of HEPES radicals does not have an impact on our measurements.



(a) Stopped flow data

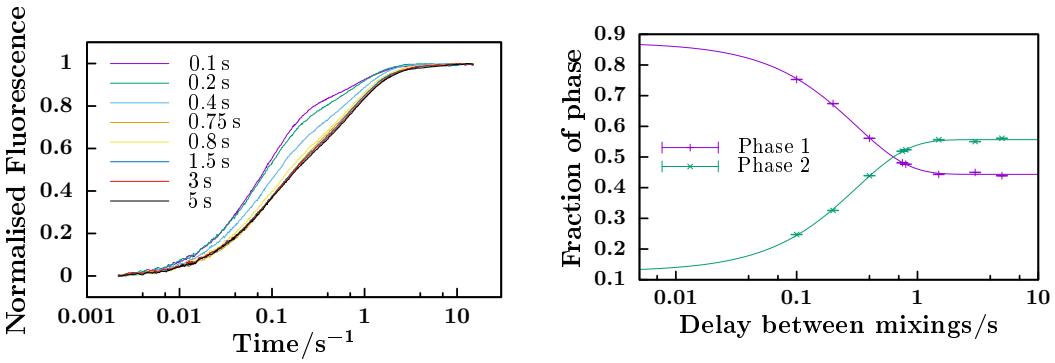
(b) Fitted rates

Figure 4.6 – Reduction of AβCu^{2+} by ascorbate in MOPS buffer. (a) Stopped flow data showing the recovery of fluorescence after mixing 50 nM AβCu^{2+} with ascorbate (concentration given in key) in MOPS/NaCl at 298 K. Each trace is the average of seven repeats. (b) Rate of fast and slow phases against ascorbate concentration. Rates determined from exponential fitting of the raw data in (a). Data from Fig. 4.5 using HEPES/NaCl as the buffer is shown in grey for comparison. Error bars display the uncertainty of the parameters derived from the fit of the raw data.

4.4.2 Reduction goes via Component I

As was described in Section 3.1.2, at physiological pH the AβCu^{2+} complex is not a single species, but instead exists in dynamic equilibrium between two major conformations, referred to as Components I & II. It has been suggested that redox and ROS generation occur via the Component I coordination, however no kinetic data has been presented to back this hypothesis. I set out to address this question using a double-mixing stopped flow approach whereby Aβ and Cu^{2+} were rapidly mixed, then after various delay times, ascorbate was mixed with the freshly formed AβCu^{2+} complex. This approach allowed us to probe the reactivity of each component as the populations of each evolved temporally.

Fig. 4.7(a) shows how the fluorescence recovery changes as the delay time between AβCu^{2+} complex formation and reaction with ascorbate is varied. At short delay times, before the complex has had time to interconvert to Component II, the reaction occurs with the fastest rate. Conversely, when the delay time is long, the reaction occurs more slowly, as indicated by the shift to the right in the position of the fluorescence trace. It can also be noted from Fig. 4.7(a) that the contribution of



(a) Stopped flow data

(b) Relative ampltude of the two phases

Figure 4.7 – Reduction of AβCu^{2+} probed by double mixing stopped flow. (a) Kinetics of reduction probed by double mixing stopped flow. 100 nM Aβ was first mixed with 2 mM Cu^{2+} (1:1 volume) and then after a variable delay (given in the key), with 2 mM ascorbate (1:1 volume). Experiment performed at 298 K. Each trace is the average of seven repeats. (b) Temporal evolutions of the fractions of the fast and slow phases. Error bars represent the uncertainty in the values determined from fitting of the raw data.

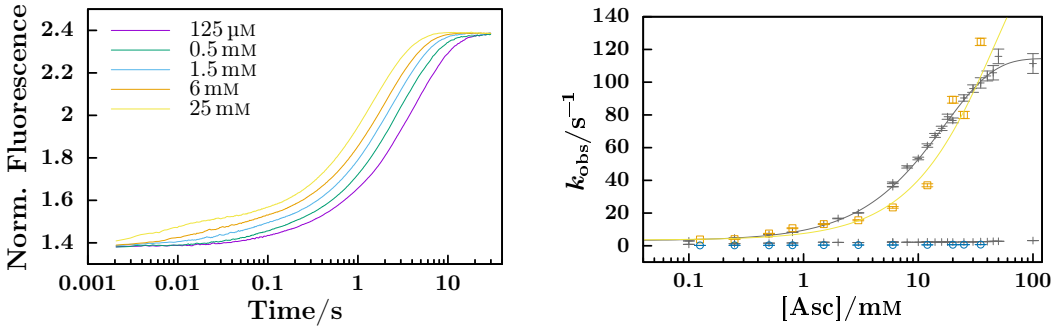
each phase also varies as a function of delay time. This is more easily visualised in Fig. 4.7(b) which shows how the fraction of each phase (determined from the amplitudes of the fitting of each trace) evolves as delay time is increased.

4.5 Comparisons between the wild-type and mutant Aβ peptides

4.5.1 The murine Aβ peptide

The murine Aβ peptide was introduced in Section 3.2 where it was shown that at physiological pH the Component I/II equilibrium for the murine peptide lies much further towards Component II. Compared with the human peptide, which has ∼60 % as component I at equilibrium, the murine peptide is almost 90 % in the Component II conformation at pH 7.5.

As was discussed in Section 4.4.2 and shown in Fig. 4.7 the reduction of the AβCu^{2+} complex goes via the Component I complex and not via Component II. One would therefore expect this to have a major impact on the reduction kinetics of the murine Aβ peptide. Fig. 4.8 shows stopped flow data for the reduction of murine AβCu^{2+} by ascorbate. It can be seen that the slow phase is dominating the reaction, i.e. the conversion of Component II to Component I is limiting the rate of



(a) Stopped flow traces

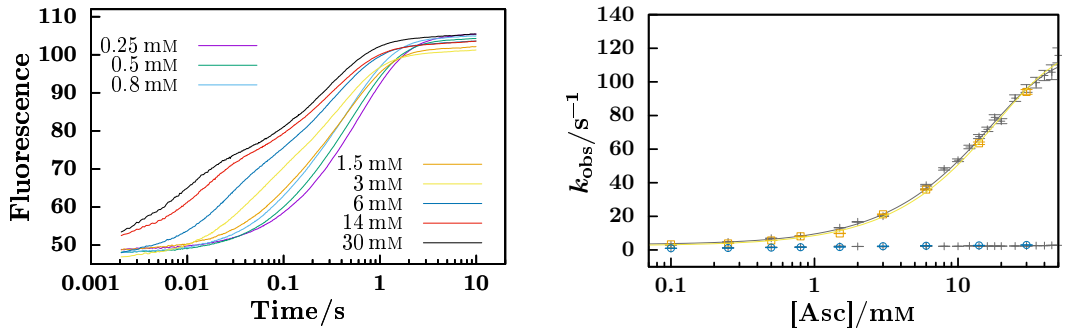
(b) Fitted rates

Figure 4.8 – Kinetics of murine$A\beta Cu^{2+}$ reduction. (a) Stopped flow data showing the recovery of fluorescence after mixing 50 nM murine $A\beta Cu^{2+}$ with ascorbate (concentration given in key) in HEPES/NaCl at 298 K. Each trace is the average of seven repeats. (b) Rate of fast and slow phases determined from the exponential fitting of data in (a). Data from Fig. 4.5 for the human $A\beta Cu^{2+}$ is shown in grey for comparison. Error bars display the uncertainty of the parameters derived from the fit of the raw data.

the reaction. This also provides evidence that the assignment of the fast and slow phases of reduction to the Component I and II species respectively, is correct.

Fig. 4.8b shows how the rates of the fast and slow phases for the reduction of $mA\beta Cu^{2+}$ compare with the reduction of the human $A\beta Cu^{2+}$ complex. It is interesting to note that the change in rate for the fast and slow phases while similar, are not identical for the murine and human $A\beta Cu^{2+}$ complexes. It appears that for the murine peptide the rate of the fast phase does not plateau out at the same concentration of ascorbate as the human wild-type does. Of all of the mutations in the murine peptide, it may be the loss of His13 (a reside that is known to coordinate to the metal centre) that is causing this change in the rate of the fast phase.

It should be noted, however, that even though there may be differences in how the rate of the fast phase varies with changing ascorbate concentration, the major factor governing the overall rate of reduction of the murine peptide is the differences in the ratio of Component I to II, and not differences in the rate of the actual reduction step. Because the murine peptide is mostly in the Component II conformation at neutral pH, and as Component II seems to be 'inert' to reduction, the rate of reduction is limited by first having to interconvert to Component I. This suggests that the overall rate of ROS production for the murine Aβ peptide will be much less compared with the human peptide, which may be linked to why signs of Alzheimer's are not observed in the mouse brain.



(a) Stopped flow traces **(b)** Fitted rates

Figure 4.9 – Kinetics of H6RAβCu^{2+} reduction. (a) Stopped flow data showing the recovery of fluorescence after mixing 50 nM H6RAβCu^{2+} with ascorbate (concentration given in key) in MOPS/NaCl at 298 K. Each trace is the average of seven repeats. (b) Rate of fast and slow phases determined from the exponential fitting of data in (a). Data from Fig. 4.5 for the wild type AβCu^{2+} is shown in grey for comparison. Error bars display the uncertainty of the parameters derived from the fit of the raw data.

4.5.2 Comparisons with H6R Aβ peptide

The H6R substitution (English) mutation, was introduced in Section 3.3 as one of the mutations causative of developing early onset familial Alzheimer's disease. Here the peptide is employed once more to draw comparisons between the wild type-Aβ peptide and a mutant peptide associated with higher risk of AD, this time looking at how the mutation affects the reduction kinetics. As displayed in Fig. 4.2, His6 is one of the key Aβ residues that coordinates to the Cu^{2+} centre at physiological pH. To see if the lack of His6 in this mutant Aβ peptide has an impact in the ability of the peptide to generate ROS we measured the kinetics of reduction, (Fig. 4.9).

Fig. 4.9(b) shows that the fast and slow rates for the H6R mutant are indistinguishable from the wild-type peptide. This shows that, somewhat surprisingly, the removal of one of the coordinating histidine residues does not have an impact on the rate of reduction. This insensitivity to the removal of histidine 6 could indicate that this residue is not involved in the actual kinetic reduction step, even though it is a key residue in the AβCu^{2+} complex at thermodynamic equilibrium. Furthermore, as the rate of reduction of the H6R mutant is indistinguishable from the wild type Aβ peptide, we can hypothesise that it is not a direct increase in ROS that is likely to be the detrimental factor in this version of familial Alzheimer's disease. The detrimental factor for this particular familial Alzheimer's disease mutation is more likely to be the increase in copper assisted dimerisation rate that has been reported.[105]

Taking the information gained from both the H6R and murine mutations we can hypothesise that while His6 is not involved in the reduction step, histidine 13 is.

4.6 The kinetic mechanism of reduction

In Section 4.4 we saw that for the reduction of the $A\beta Cu^{2+}$ complex by ascorbate we observe fluorescent traces consisting of the sum of two exponential phases. One of these phases (labelled as the slow phase) does not show a change in rate upon changing ascorbate concentration. This means that the process governing the slow phase is independent of ascorbate concentration, i.e. it does not depend on ascorbate binding. This process therefore represents an intermolecular step and has tentatively been assigned to the conversion of Component II (which cannot undergo reduction) to Component I and subsequent reduction. Conversely, the rate of the fast phases does show a dependence on the concentration of reducing agent, this must therefore represent the binding and reduction of the $A\beta Cu^{2+}$ Component I complex.

In the most simplest of cases the reduction of the $A\beta Cu^{2+}$ Component I complex must follow a bimolecular reaction of the form,

$$A\beta Cu^{2+} + \text{red} \longrightarrow A\beta Cu^{+} + \text{red}^{+}$$

$$r = k[A\beta Cu^{2+}][\text{red}] \tag{4.6}$$

where the rate (r) will depend on both the concentrations of the $A\beta Cu^{2+}$ complex and the reducing agent (red), with a rate constant, k. If we use a vast excess of one of the reagents, such that we are under pseudo first order conditions this can be simplified to,

$$r = k[A\beta Cu^{2+}][\text{red}] = k'[A\beta Cu^{2+}] \tag{4.7}$$

where the pseudo first order rate constant $k' = k[A\beta Cu^{2+}]$. A plot of k' against concentration of reducing agent should yield a straight line where the slope is the second order rate constant. However, as we can see from Fig. 4.5 for example, the dependence of the rate on the reducing agent concentration is not linear. The rate of the fast phase actually shows an exponential dependence on the concentration of ascorbate used. This indicates that the reaction mechanism must be more complicated than a simple bimolecular reaction process, and likely contains multiple steps.

If we consider going from the four coordinate Cu^{2+} complex to the bidentate Cu^{+} complex (Fig. 4.2) one would imagine that there would be a significant energy

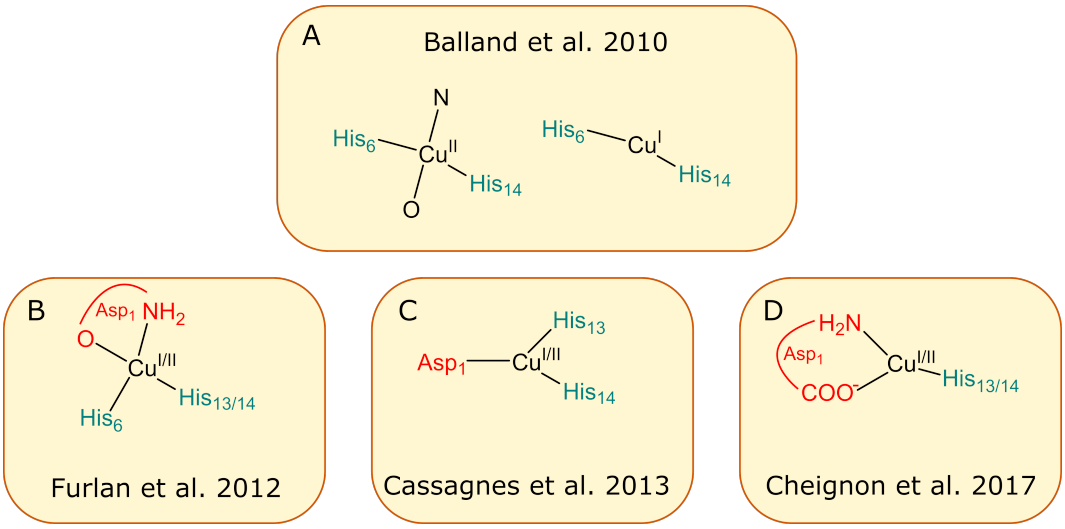


Figure 4.10 – Proposed residues coordinating to the metal centre in the 'redox active' state following pre-organisation. A, adapted from,[106] differs in that it has separate coordination environments for the Cu^{2+} and Cu^{+} oxidation states. B, adapted from,[107] C, adapted from,[108] & D, adapted from,[109] all agree that the Cu^{2+} and Cu^{+} complexes share a common coordination, but disagree on the number of total ligands and number of histidine residues coordinating. It should also be noted that B proposes an oxygen from the amide bond coordinates the metal centre, while D specifies that it is the aspartic acid side chain that is binding.

penalty for directly moving between these two coordinations. However, previous electrochemical study has shown that there is a remarkably small reorganisation energy of 0.3 eV.[106] The authors of this paper hypothesise that to account for this low reorganisation energy the AβCu^{2+} complex must first undergo a pre-organisation step, whereby the ligands are more favourably arranged such that fast electron transfer can take place. Finally, the authors propose a structure for the lowly populated reactive intermediate that is able to undergo fast redox cycling (Fig. 4.10A).

Following the proposal that redox of the AβCu complex actually goes via a sub-population of the complex, attempts were made to try and identify the structure of such a sub-population. Molecular dynamics simulations identified that the Cu^{2+} and Cu^{+} likely share a common coordination (Fig. 4.10B).[107] By observing which residues on the Aβ peptide were most commonly oxidised during redox cycling Cassagnes et al. proposed a new structure for the sub-population, which most notably suggested that His6 was not involved in binding, (Fig. 4.10C).[108] A further potential structure for the redox active sub-population was suggested based on a series of systematic residue mutations, (Fig. 4.10D).[109]

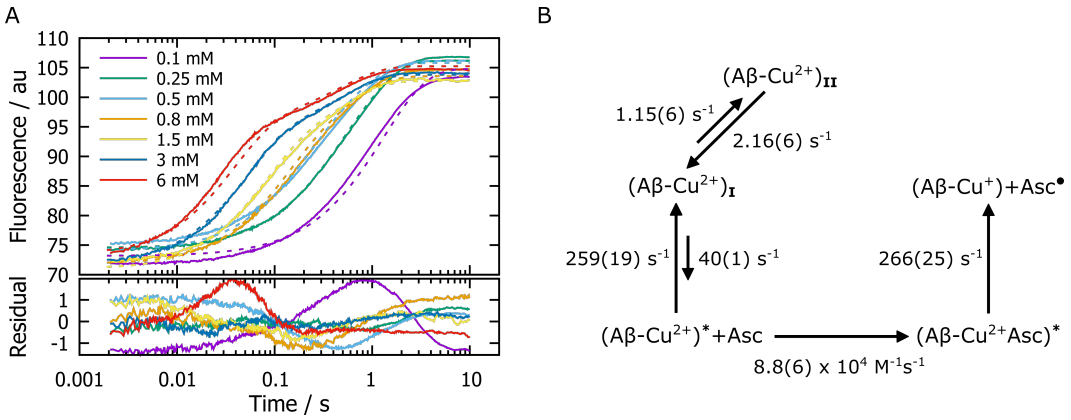


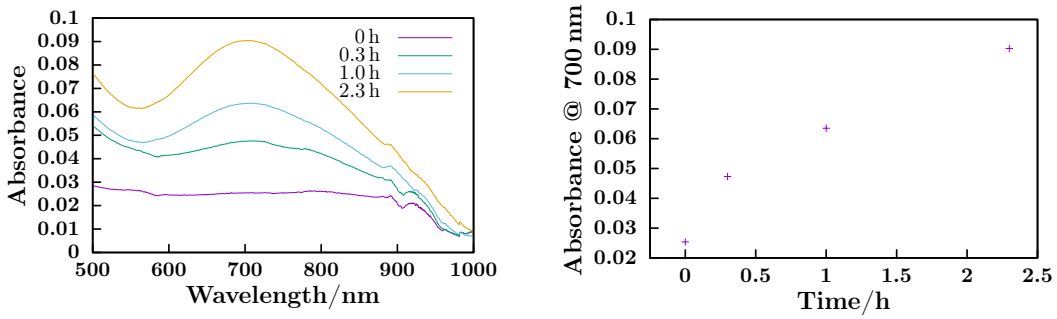
Figure 4.11 – Kinetic mechanism of $A\beta Cu^{2+}$ reduction. A Stopped flow traces showing the reduction of ABCu(II) by ascorbate, dashed lines show the expected traces given the mechanism and rate constants shown in B

Based on the data we presented in Section 4.5, our observations that His6 is not involved in the redox but His13 is, match with either of the most recent structures proposed, Fig. 4.10C & D.

If the redox cycling does go via a pre-organisation step the reaction mechanism could be described as follows,

$$(A\beta Cu^{2+})_{II} \underset{conversion}{\overset{inter-}{\rightleftharpoons}} (A\beta Cu^{2+})_{I} \underset{organisation}{\overset{pre-}{\rightleftharpoons}} (A\beta Cu^{2+})^{*} \xrightarrow{+Asc^{-}} (A\beta Cu^{2+})^{*}Asc^{-} \xrightarrow[-Asc^{\cdot -}]{reduction} (A\beta Cu^{1+}) \tag{4.8}$$

We decided to see if our kinetic data for the reduction of the $A\beta Cu^{2+}$ complex by ascorbate could be fit to a mechanism involving a pre-organisation step. Our data was fit using KinTek Explorer.[110] KinTek Explorer is a program that fits kinetic data based upon numerical integration of rate equations. Fig. 4.11 shows that a good fit of the data to the model can be achieved. The fitted rate constants for the conversion from the main Component I conformation of $A\beta Cu^{2+}$ to the intermediate capable of fast redox show that the equilibrium lies heavily on the side of Component I. Reassuringly, the rate constants determined from the fit for the interconversion between Component I and II species, are within error of values previously reported.[64] Overall, the rate constants determined suggest that the reduction step happens on the ms time scale, with the conformational selection step of the mechanism being the rate limiting step.



(a) UV-Vis spectra

(b) Oxidation of Cu(I) over time

Figure 4.12 – Auto-oxidation of Cu^+ ions. (a) Oxidation of 20 mM $[Cu(MeCN)_4]BF_4$ in (non-degassed) MQ with 10 % MeCN monitored by UV-Vis. (b) Absorbance of (a) at 700 nm as a function of time.

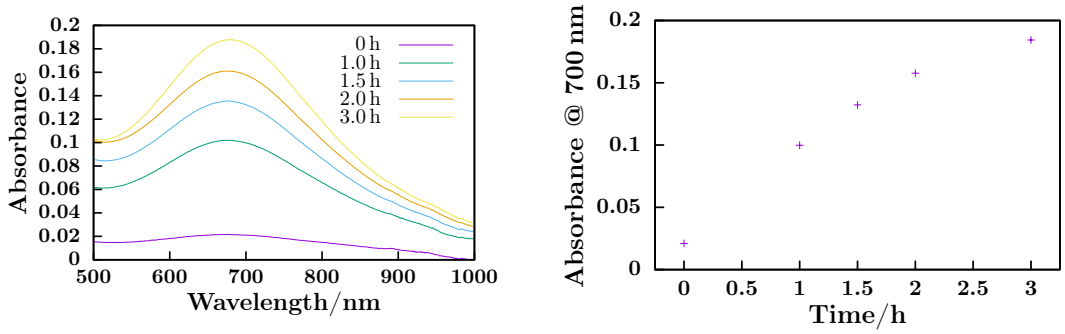
4.7 Oxidation of AβCu$^+$

If we want to understand the redox cycling of the AβCu complex we must investigate the oxidation side of the cycle as well as the reduction. However, experiments for studying the oxidation side of the cycle are much less tractable. Cu^+ salts are unstable in air or solution, either reacting with oxygen or disproportionating to give Cu^0 and Cu^+.

An acetonitrile ligated Cu(I) complex $[Cu(MeCN)_4]BF_4$ has been reported to have an increased stability to air oxidation in acetonitrile solution. As a result, we tested the possibility of generating an AβCu(I) complex using this salt.

While the $[Cu(MeCN)_4]BF_4$ salt shows stability in acetonitrile our experiments should take place in an aqueous solution and not an organic solvent. To test the stability of the Cu(I) salt, the appearance of the Cu^{2+} absorption band (ca. 700 nm) was followed, this is shown in Fig. 4.12. It can be seen that in MilliQ water the Cu(I) is slowly converting to Cu(II) on the hour time scale. For comparison, a 20 mM solution of Cu_2Cl would have a peak absorbance of 0.24 (assuming a peak extinction coefficient of 12 $M^{-1}\,cm^{-1}$). It can be estimated that after 2 h (the typical length of time it would take to complete several stopped flow measurements) ca. 35 % of the Cu(I) would have converted to Cu(II).

Although the oxidation of the Cu(I) salt was relatively slow in MQ water, our experiments should really take place in a buffered aqueous solution. Therefore the formation of the Cu^{2+} absorption band was monitored in a solution of the $[Cu(MeCN)_4]BF_4$ salt in HEPES buffer that had been first degassed with N_2 to try and limit oxidation by dissolved oxygen. The results are shown in Fig. 4.13.



(a) UV-Vis spectra

(b) Oxidation of Cu(I) over time

Figure 4.13 – Auto-oxidation of Cu$^+$ ions. Oxidation of 20 mM $[Cu(MeCN)_4]BF_4$ in (N_2 degassed) HEPES (50 mM) with 10 % MeCN monitored by UV-Vis

The results show that even though attempts were made to remove the oxygen from the solution, the presence of HEPES appears to make the oxidation of the Cu(I) salt to Cu(II) occur more readily. Approximately 60 % was shown to have converted to Cu(II) after 2 h.

The $[Cu(MeCN)_4]BF_4$ salt did not show a high degree of stability in buffered aqueous solution, even when attempts were made to limit the amount of oxygen present. Nevertheless a stopped flow experiment was attempted to monitor the binding of Aβ and Cu^+, while trying to perform the experiment as rapidly as possible to minimise the degradation of the Cu(I) salt to Cu^{2+}. Fig. 4.14 shows the stopped flow fluorescent traces. As Cu(I) is diamagnetic, its binding to the fluorescently labelled Aβ should not result in quenching of the fluorophore, however a quenching of fluorescence is observed. From this result it can be deduced that either: (i) the Cu(I) is binding to the Aβ peptide and is rapidly oxidised to Cu(II) thus resulting in quenching, or (ii) enough of the Cu(I) salt has already oxidised to Cu(II) that when mixed with Aβ the quenching we observe in Fig. 4.14 is simply a result of Cu(II) directly binding.

To decide which possibility is more likely we can consider the kinetics of the process. Each trace in Fig. 4.14 contains multiple phases. The fastest phase (occurring below 0.01 s) is so fast that it is only visible in the 1 µM trace, having mostly already occurred in the dead time of the instrument at higher concentrations. The second phase (occurring between 0.01 s and 0.1 s) is visible in all traces. Plotting this rate against concentration yields a straight line with a forward rate constant of $3.0(1) \times 10^6\,\mathrm{M^{-1}\,s^{-1}}$. This is within one order of magnitude of a previously reported

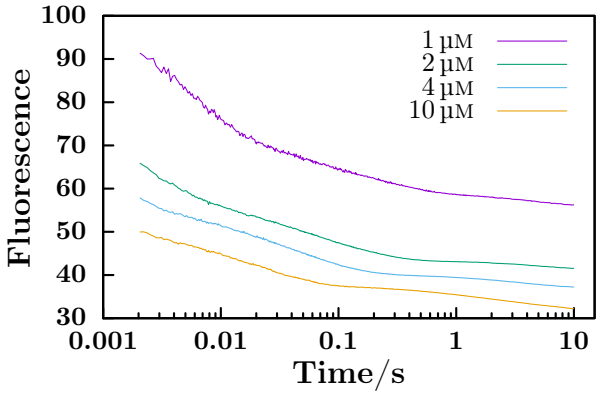


Figure 4.14 – Kinetics of Aβ $[Cu(MeCN)_4]BF_4$ association. Stopped flow traces showing the mixing of 50 nM labelled Aβ with $[Cu(MeCN)_4]BF_4$ (concentrations given in key). Each trace is the average of at least seven repeats, experiment carried out at 298 K.

value for the rate of a second Cu^{2+} binding to Aβ ($4.2(6) \times 10^5\,M^{-1}\,s^{-1}$). It can also be noted that increasing the concentration of $[Cu(MeCN)_4]BF_4$ added causes the rate of fluorescent quenching to increase, which would not be the case for Cu(I) binding to the peptide and then undergoing fast reduction as this reduction step is intramolecular and should not have a dependence on the concentration of Cu(I).

It therefore seems that even when trying to perform the experiment as rapidly as possible, there is still enough Cu(I) that has already oxidised to Cu(II) for it to bind to the Aβ peptide and quench the fluorescence. It should also be noted that in these experiments 50 nM Aβ is used, so only a small proportion of the µM amounts of Cu(I) being mixed has to have degraded to Cu(II) for it to saturate the Aβ peptide.

4.7.1 'In situ' produced $A\beta Cu^+$

To circumvent the problems with trying to use unstable Cu(I) salts to generate the $A\beta Cu^+$ complex I employed a double mixing stopped flow approach. In this approach $A\beta Cu^+$ could be generated in situ via reduction of $A\beta Cu^{2+}$ with ascorbate, then after a short delay oxidised back to $A\beta Cu^{2+}$ by H_2O_2. An example of a stopped flow trace showing both mixing steps can be seen in Fig. 4.15.

A problem with this method is that after the final mixing there will be both ascorbate and H_2O_2 present. Therefore, as the oxidation reaction progresses, both oxidation and reduction will be taking place. At the very beginning of the oxidation reaction however, the concentration of $A\beta Cu^{2+}$ will be effectively zero and so reduction will not be taking place. By limiting the data analysis to just the beginning of the

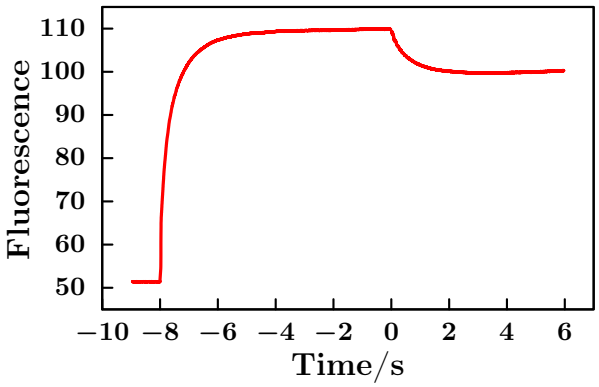


Figure 4.15 – 'In situ' formation of AβCu$^+$ by double mixing. Fluorescent trace of double mixing stopped flow showing both mixing steps. At t=−8 s AβCu^{2+} is mixed with ascorbate and recovery of fluorescence is observed as the complex becomes AβCu$^+$, at t=0 s the freshly formed AβCu$^+$ is mixed with H_2O_2 (50 mM) and quenching of fluorescence is observed as the complex returns to AβCu^{2+}. Note the intensity values have been manually adjusted to account for dilution upon subsequent mixing steps.

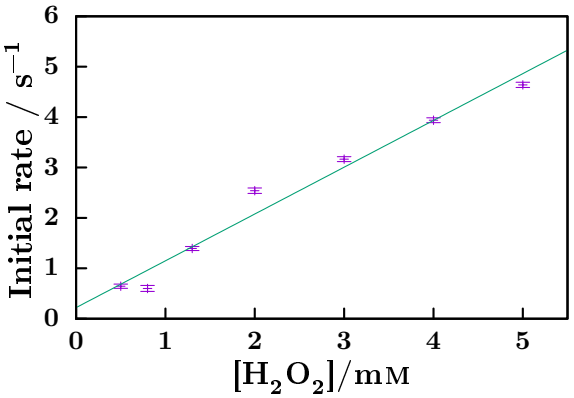


Figure 4.16 – Initial rate of AβCu$^+$ oxidation against H_2O_2. AβCu^{2+} was initially reduced with ascorbate before being re-oxidised by various concentrations of H_2O_2. Initial rates were determined and are shown plotted here.

kinetic trace, the initial rate can be approximated by a straight line. This rate should be the rate of oxidation. Fig. 4.16 shows how the initial rate of oxidation of AβCu$^+$ varies with H_2O_2 concentration. The rate of oxidation varies linearly with increasing H_2O_2 concentration indicating a bimolecular association process, with an apparent second order rate constant of $9.3(6) \times 10^2\,\mathrm{M^{-1}\,s^{-1}}$.

In all the stopped flow experiment presented, the O_2 concentration of the buffers was not measured, but is assumed to be that of air saturated water at 25 °C (∼200 µM). For the oxidation of 'free' Cu$^+$ to Cu^{2+} it has been reported that the rate constant

using O_2 as the oxidant is two orders of magnitude slower than the rate constant for oxidation by H_2O_2.[111] While the values of the oxidation rate constants are likely to change when the Cu is complexed by Aβ, the trend will likely remain, i.e. the oxidation rate of $A\beta Cu^+$ by O_2 is much slower than by H_2O_2. Considering that physiological O_2 concentration is approximately 5-10 % (i.e. tens of µM) and that physiological H_2O_2 concentrations can reach similar levels, it would appear that H_2O_2 might be the more physiological oxidant of the AβCu complex. Regardless, the oxidation of $A\beta Cu^+$ by dissolved O_2 is too slow to be detected on the timescales of the stopped flow experiments.

4.8 Summary

In this chapter the kinetics of reduction and oxidation of the AβCu complex have been investigated. The development of an experimental approach, which exploits the differing fluorescent quenching abilities of paramagnetic Cu^{2+} and diamagnetic Cu^+ ions has been detailed. This gives us a system which can directly report on the oxidation state of the metal ion complexed to the Aβ peptide.

I have shown that of the two major binding modalities of the $A\beta Cu^{2+}$ complex present at neutral pH, it is Component I which undergoes reduction, while Component II appears to be unreactive. Interestingly, metal bridged dimerisation of Aβ (one of the proposed ways that toxic Aβ oligomers can form) has also been described as going via the Component I species and not via Component II.[64] Taken together, these observations on the differing reactivity of the two $A\beta Cu^{2+}$ complexes could have interesting implications for the disease. The Cu^{2+} bound to the Aβ is flexible and dynamic in nature, with the Cu^{2+} able to shuttle between each conformation on the hundreds of millisecond timescale.[64] If, through some intervention, the equilibrium could be biased towards the less reactive Component II, or lock the complex in this conformation entirely we may have a useful therapeutic strategy for Alzheimer's disease. A strategy that is perhaps more subtle than trying to chelate the metal away from the Aβ peptide entirely.

I have shown that the reduction kinetic data can be fit to a conformational selection mechanism,[112] whereby the main $A\beta Cu^{2+}$ Component I complex must first rearrange its coordinating amino acids more favourably for redox to occur, agreeing with literature.[108,109] By studying the reduction kinetics of mutant versions of the Aβ peptide we have provided evidence that in this reactive intermediate histidine 6 does not play a role, while histidine 13 likely does. This matches with two out of the four coordination environments for the reactive intermediate that have been

proposed thus far. Also agreeing with literature, the kinetic parameters derived from our fitting show that the equilibrium between Component I and the reactive intermediate lies heavily towards Component I.

I have shown that the reduction step itself occurs readily on the millisecond timescale. The brain has one of the highest concentrations of ascorbate within the body, with concentrations of one to two mM reported and intracellular neuronal concentrations even higher.[113] Combining this with our rate constants we propose that binding of ascorbate to the AβCu^{2+} complex is not rate limiting in the reduction mechanism, while the pre-organisation of the complex to the minor intermediate state is. Overall, the reduction would occur on the 10 ms timescale, this is much faster than the lifetime of the Component I complex which has a reported dissociation constant $\sim$0.8 s^{-1}.[64].

Through use of a double mixing stopped flow approach, we were able to generate the AβCu^{+} complex 'in situ', allowing us to study the kinetics of oxidation by H_2O_2. In contrast to the reduction kinetics, the oxidation side of the cycle is expected to be much slower. Concentration of H_2O_2 within in the brain is in the low µM regime, peaking at ca. 100 µM after global ischemia in a rat brain.[114]

Taken together the results presented in this chapter suggest that while the reduction step is highly capable of generating damaging radicals, the oxidation step is going to occur less frequently, and it is this oxidation step that is the bottleneck in redox cycling of the AβCu complex.

Chapter 5

Lipid Peroxidation by the AβCu Complex

In Chapter 4 the kinetics of the reduction and oxidation of the AβCu complex was explored. This kinetics underpins the ability of the AβCu complex to generate reactive oxygen species (ROS) such as $O_2^{\bullet -}$, H_2O_2, $^1O_2$ and $OH^{\bullet}$. While we can use the kinetics determined in Chapter 4 to approximate a rate for ROS production, we cannot know how many of these ROS go on to cause damage compared with how many are terminated before damage can occur. To determine the 'damage potential' of the AβCu complex we need a way to measure not just the ROS produced but also the damage that the ROS causes.

5.1 Methods for measuring ROS

There are a variety of fluorescent probes capable of measuring ROS production. The use of fluorescence to detect ROS provides high sensitivity along with straightforward data collection. Data can be acquired rapidly, allowing kinetic data to be more easily obtained compared with using mass spectrometry for example. Many of these fluorescent probes are sensitive to a specific type of reactive oxygen species, with a thorough review having been provided by Gomes et al.[115] Within the field of AβCu ROS production, a very commonly used fluorescent probe for detecting ROS is coumarin-3-carboxylic acid (3-CCA).

3-CCA (Fig. 5.1) is able to detect the presence of hydroxyl radicals ($OH^{\bullet}$) in solution. It is initially a non-fluorescent compound, but upon hydroxylation generates the fluorescent 7-hydroxycoumarin (7-OHC) having an emission maximum around



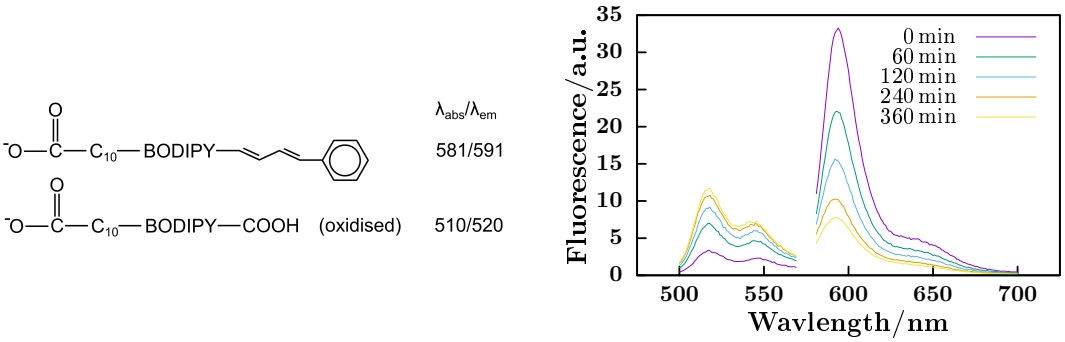
Figure 5.1 – 3-CCA and its major hydroxylation product 7-OHC. Coumarin-3-carboxylic acid (3-CCA) is initially non-fluorescent, following hydroxylation it forms the fluorescent 7-hydroxycoumarin (7-OHC).

450 nm and a quantum yield of ∼0.5. 3-CCA has been used to show that AβCu produces hydroxyl radicals in the presence of ascorbate,[116] and has been used to measure the effect that mutations around the Cu^{2+} binding site have on the ability of the AβCu complex to generate $OH^{\cdot}$.[109].

While using 3-CCA as an indicator of the formation of ROS in solution is a relatively straightforward and highly reproducible approach that gives a useful insight into the ability of AβCu to generate damaging ROS, it is not directly measuring ROS damage. One of the main locations of oxidative damage within the AD brain is to lipid membranes.[117] If one was able to study the oxidative damage to lipid membranes caused by AβCu generated ROS, one might be able to get a better insight into AβCu mediated damage, than just looking at the ability of the complex to form radicals in solution.

As 3-CCA is a charged molecule (at physiological pH) it is not particularly well suited to detecting lipid peroxidation. In order to detect ROS on the lipid membrane a different type of ROS sensitive probe is required. One such probe is C_{11}-BODIPY$^{581/591}$ (Fig. 5.2), which is a lipid like molecule containing a BODIPY based fluorophore.[118] The presence of a phenyl butadiene moiety makes the probe sensitive to oxidation, and this phenyl butadiene being attached to the BODIPY fluorophore results in a drastic change in the fluorophores properties following its loss upon oxidation.

As the C_{11}-BODIPY$^{581/591}$ probe contains a long C_{11} alkane chain it will position itself within a lipid membrane, and has been shown to occupy a position either 18 Å or < 7.5 Å from the center of the bilayer.[118] Importantly, even following oxidation, the C_{11}-BODIPY$^{581/591}$ probe remains lipophilic and does not spontaneously leave the bilayer.[118] Analysis by mass spectrometry showed that upon oxidation of the C_{11}-BODIPY$^{581/591}$ probe two major products were formed, either losing the entire phenyl butadiene moiety (as shown in Fig. 5.2) or with the probe retaining one of



(a) **(b)** Integrated peak area

Figure 5.2 – C_{11}-BODIPY$^{581/591}$ peroxidation probe. (a) Structure of the C_{11}-BODIPY$^{581/591}$ probe and its major oxidation product, along with how oxidation of the molecule changes both the excitation and emission maxima. (b) Fluorescent spectra of the unoxidised and oxidised probe and how they respectively decrease and increase as the dye becomes oxidised.

the double bonds.[119]

Some researchers have expressed concerns about using C_{11}-BODIPY$^{581/591}$ as an indicator of lipid peroxidation; it has been reported that it overestimates lipid damage, and that the probe can itself act as an antioxidant.[120] By measuring the signal from the C_{11}-BODIPY$^{581/591}$ probe under oxidising conditions, and then comparing it to the oxidation of an unsaturated lipid as determined by mass spectrometry they found that, under their experimental conditions, the C_{11}-BODIPY$^{581/591}$ probe showed complete oxidation after 30 min while unoxidised lipids were still detected by mass spec up until 60 min. They also note that at high concentrations of C_{11}-BODIPY$^{581/591}$ probe (0.5 mole%) the rate of unsaturated lipid oxidation (as measured by mass spec) is decreased. They rationalise this by stating that if the C_{11}-BODIPY$^{581/591}$ probe is more sensitive to oxidation than SAPC, the probe will be preferentially oxidised before the lipid undergoes oxidation, and as such they label C_{11}-BODIPY$^{581/591}$ an antioxidant.

While it is entirely plausible that the two C=C double bonds in the C_{11}-BODIPY$^{581/591}$ probe will be more susceptible to oxidation than certain unsaturated lipids, it is also likely that lipids exist which are more sensitive to oxidation than the C_{11}-BODIPY$^{581/591}$ probe. The very method of how the probe reports on reactive oxygen species will of course have implications on the kinetics of lipid oxidation. To be able to quantitatively say how much of a particular lipid had been oxidised by measuring C_{11}-BODIPY$^{581/591}$ fluorescence would not be a facile task. However, (and as the concerned authors concede) C_{11}-BODIPY$^{581/591}$ "is ... a sensitive indicator of

free radical processes that have the potential to oxidize lipids in membranes."[120]

5.2 Measuring lipid peroxidation using BODIPY™581/591 C11

5.2.1 GM1 micellar system

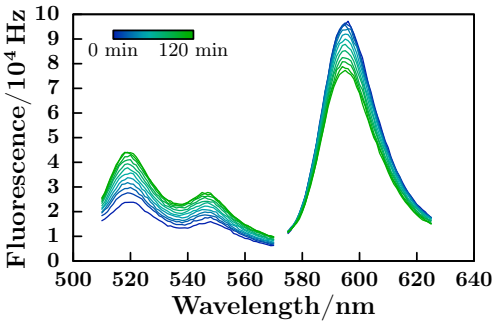
GM1 is a type of glycosphingolipid that contains many sialic acid groups attached to the lipid head group. It is found in the membranes of neuron cells and has been linked to the formation of lipid microdomains. It has been suggested that such lipid microdomains may act as locations for Aβ aggregation with people suggesting that a Aβ-GM1 complex may act as a seed for aggregation.[121,122] GM1 spontaneously forms micelles when above its critical micelle concentration of 20 nM in solution.[123] The micelles typically have a hydrodynamic radius of 5.67(6) nm and are made up of 168(4) GM1 molecules.[124] Using different techniques, several values for the dissociation constant of Aβ to GM1 micelles have been reported, with the K_d in the range of ∼100 nM - 5 µM.[122,125,126]

Because formation of GM1 micelles is easy and reproducible, and because they bind Aβ in the low µM regime the GM1 micelle represents a useful model to begin to study the lipid damage potential of the AβCu complex.

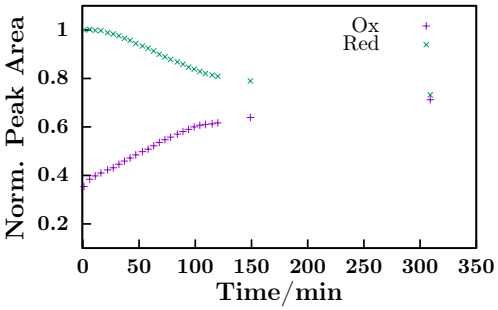
Fig. 5.3 shows how the GM1 membrane is becoming oxidised by the $A\beta Cu^{2+}$ complex in the presence of ascorbate. Oxidation of the membrane is slow but persistent, with changing fluorescence occurring over the whole of the first 120 min of continuous measurement, and even persisting after 5 h.

Fig. 5.4 shows how the GM1 membrane is oxidised by uncomplexed Cu^{2+} in the presence of ascorbate. Uncomplexed Cu^{2+} should be able to undergo redox cycling faster than when complexed with Aβ, as there is no peptide present to hinder the approach of reducing or oxidising agents, thereby generating more ROS. Indeed, Fig. 5.4 shows a faster initial rate of lipid peroxidation caused by free Cu^{2+} compared with $A\beta Cu^{2+}$. However, the lipid peroxidation by free Cu^{2+} plateaus off rather quickly, and does not show the same level of persistent lipid peroxidation as observed with $A\beta Cu^{2+}$.

Fig. 5.5 shows two lipid peroxidation control experiments. One shows that in GM1 micelles the C_{11}-BODIPY$^{581/591}$ probe shows little auto-oxidation when in the presence of ascorbate. The other shows that the persistent damage caused by the $A\beta Cu^{2+}$ complex in the presence of ascorbate does not occur when the copper is

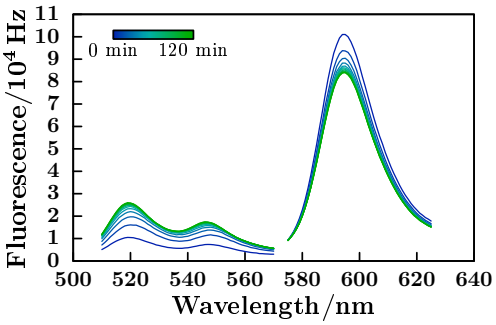


(a) Spectra

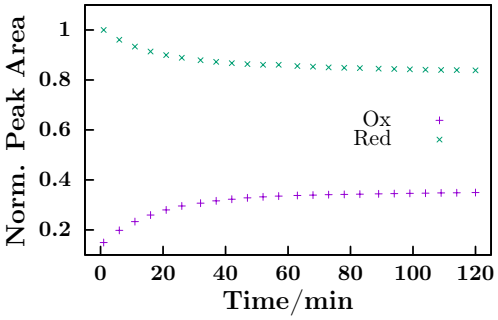


(b) Integrated peak area

Figure 5.3 – Peroxidation of GM1 micelles by AβCu^{2+}. (a) Fluorescent spectra showing oxidation of GM1 (200 µM) containing 0.01 % C_{11}-BODIPY$^{581/591}$ probe induced by Aβ40 (1.3 µM) Cu^{2+} (1 µM) and asc (100 µM) in HEPES/NaCl at 295 K. λ_{Ex} 500 nm, λ_{Em} 510-570 nm and λ_{Ex} 565 nm, λ_{Em} 575-625 nm. (b) Integrated area of peaks shown in (a) for the oxidised and reduced forms of the C11-BODIPY probe over time.



(a) Spectra

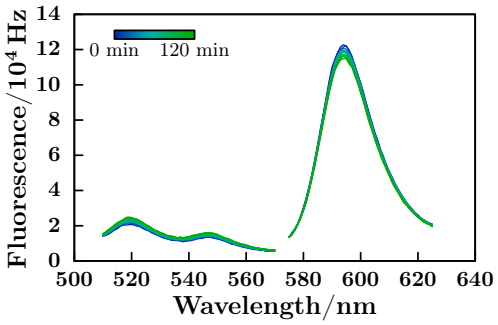


(b) Integrated peak area

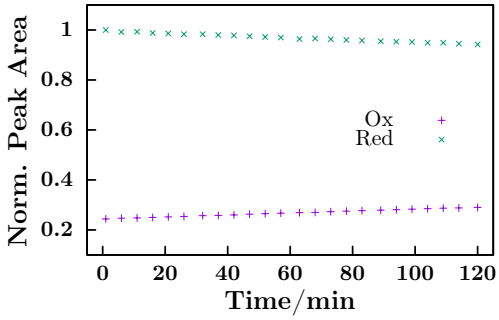
Figure 5.4 – Peroxidation of GM1 micelles by Cu^{2+}. (a) Fluorescent spectra showing oxidation of GM1 (200 µM) containing 0.01 % C_{11}-BODIPY$^{581/591}$ probe induced by Cu^{2+} (1 µM) and asc (100 µM) in HEPES/NaCl at 295 K. (b) Integrated area of peaks shown in (a) for the oxidised and reduced forms of the C11-BODIPY probe over time.

chelated by EDTA.

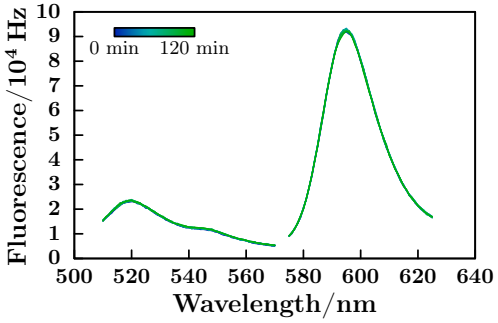
The data for lipid peroxidation of GM1 micelles containing the C_{11}-BODIPY$^{581/591}$ probe is summarised in Fig. 5.6. This figure takes the ratio of the oxidised peak to the reduced peak after 120 min for each of the conditions presented in Figs. 5.3-5.5 and compares them to the amount of peroxidation that occurred when only lipid and ascorbate was present. Fig. 5.6 clearly shows that the lipid membrane is damaged much more when in the presence of AβCu^{2+} than in its absence. And that the increased damage when in the presence of AβCu^{2+} is attenuated when the Cu^{2+} is



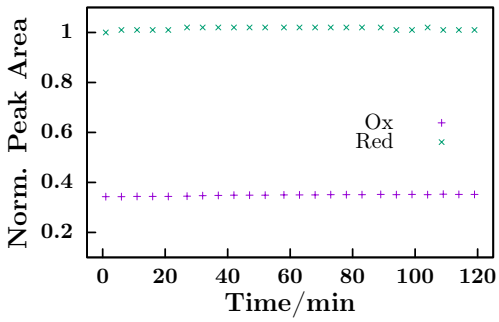
(a) Spectra GM1 auto-oxidation



(b) Integrated peak area



(c) Spectra Oxidation with EDTA present



(d) Integrated peak area

Figure 5.5 – Auto-peroxidation of GM1 micells is low and is inhibited in the presence of EDTA. (a) Fluorescent spectra showing auto-oxidation of GM1 (200 µM) containing 0.01 % C_{11}-BODIPY$^{581/591}$ probe in HEPES/NaCl at 295 K. (b) Integrated area of peaks shown in (a) for the oxidised and reduced forms of the C11-BODIPY probe over time. (c) Fluorescent spectra showing no oxidation of GM1 (200 µM) containing 0.01 % C11-BODIPY probe induced by Aβ40 (1.3 µM) Cu^{2+} (1 µM) and asc (100 µM) when EDTA (100 µM) is also present, in HEPES/NaCl at 295 K. (b) Integrated area of peaks shown in (c) for the oxidised and reduced forms of the C11-BODIPY probe over time.

chelated by EDTA. Crucially when free Cu^{2+} is present, the damage to the lipid membrane is approximately half of that when in the presence of AβCu^{2+}. This observation is particularly interesting as we know that free Cu^{2+} can generate more ROS than when the Cu^{2+} is complexed to Aβ, and yet this increased ROS production is not leading to more lipid damage.

The cause of the increased damage is potentially due to the localisation of the ROS generation. The C-terminal of the Aβ peptide is hydrophobic and has been shown to insert itself into lipid membranes, with the metal binding N-terminus sticking out into solution. The rate constant for Cu^{2+} binding to Aβ on GM1 micelles has been previously measured and was found to be the same order of magnitude as binding to

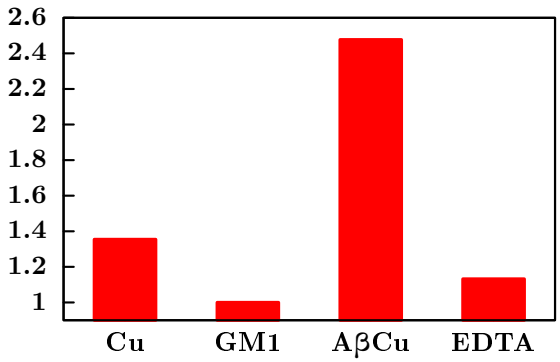


Figure 5.6 – Peroxidation of GM1 micelles is more efficient by $A\beta Cu^{2+}$ than Cu^{2+} alone. Bar chart showing the ratio of the oxidised peak to the reduced peak after 120 min, relative to the amount of auto-oxidation of theC_{11}-$BODIPY^{581/591}$ probe (which was set to a value of 1). In all cases GM1 (200 µM) containing 0.01 % C_{11}-$BODIPY^{581/591}$ probe was present in HEPES/NaCl, and either contained Cu^{2+} (1 µM), Aβ40 (1.3 µM) and/or EDTA (100 µM) in the combinations shown in the bar chart labels. All experiments were done at 298 K.

Aβ further suggesting that the N-terminus of Aβ is freely exposed on the surface of the lipid membrane. If the Aβ is bound to the membrane, any ROS generation would be occurring right on the membrane surface. As such the radicals would not have far to diffuse before they encounter the membrane. In contrast ROS produced from Cu^{2+}, which will be equally distributed throughout the solution, may have further to diffuse before being able to damage the membrane and as such would be more likely to have reacted with something else in solution in that time.

As well as the potential for the ROS to be generated on the surface of the membrane when Aβ is bound to the membrane the lab of Butterfield has also put forward an alternate role for membrane bound Aβ in relation to lipid peroxidation. They posit that a sulfranyl radical could be generated on the vulnerable methionine 35 residue of Aβ via electron transfer to the copper ion.[127] Methionine 35 is located in the hydrophobic region of Aβ and so would be inside the membrane ideally located near unsaturated lipid tails, promoting efficient radical propagation and lipid peroxidation.

Whether the increased efficiency of lipid damage by $A\beta Cu^{2+}$ is due to the ROS being generated locally on the membrane surface, or because radicals are able to be generated inside the membrane through involvement of the Met35 residue is not clear. However, it is clear, that for a GM1 micellar system, the $A\beta Cu^{2+}$ is able to more efficiently damage the membrane than Cu^{2+} alone.

5.2.2 DLPC vesicle system

In this section thus far the model membrane has been GM1 micelles. Micelles are a useful tool as they form spontaneously, provided they are above their critical micelle concentration, and are generally of a similar size. GM1 is also a useful lipid to use as it is present in neuronal membranes, and has been suggested that microdomains formed of GM1 act as the locations of binding for Aβ to the neuronal membrane. Micelles however only contain a single lipid layer, rather than the lipid bilayer that surrounds a cell, and due to the large size of the GM1 headgroup the outer surface of a GM1 micelle would not have as tight packing as a lipid bilayer.

A model lipid system, that more closely mimics a physiological membrane bilayer than the GM1 micelle system employed thus far, would be a unilamellar vesicle.

DLPC (1,2-dilauroyl-*sn*-glycero-3-phosphocholine) is a saturated lipid with two tails, each containing 12 carbon atoms. A saturated lipid was used so that any radicals formed would not be able to damage the lipid vesicle itself, and would only be able to damage the C_{11}-BODIPY$^{581/591}$ probe. Fig. 5.7 shows how the area of the oxidised peak of the C_{11}-BODIPY$^{581/591}$ probe changed under various conditions.

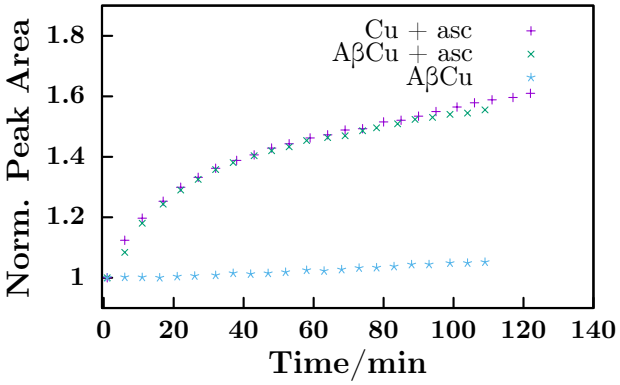


Figure 5.7 – Peroxidation of DLPC SUVs by AβCu^{2+}. DLPC (1 mM) containing 0.1 % C11-BODIPY in HEPES/NaCl at 298 K. Cu^{2+} (1 µM) Aβ (1.3 µM) ascorbate (100 µM)

Similarly, to what was observed for the oxidation of the C_{11}-BODIPY$^{581/591}$ probe in a GM1 micellar system, when there is no ascorbate present, the rate of auto-oxidation is slow. However, unlike with GM1 micelles, there does not appear to be any difference in the oxidation when induced by either the Aβ40Cu^{2+} complex or Cu^{2+} alone.

5.3 Fluorescent correlation spectroscopy of Aβ40 binding to vesicles

One explanation for not observing a difference between the oxidation induced by the Aβ40Cu^{2+} complex and Cu^{2+} alone on vesicles is that the Aβ40 may not be able to bind to the lipid small unilamellar vesicles (SUV). Fluorescence correlation spectroscopy (FCS) is a powerful tool and is particularly useful when trying to determine the diffusion time of a fluorescent species. Compared with an SUV, an Aβ40 monomer would diffuse much more quickly, and so if we observe the diffusion time of labelled Aβ40 in the presence and absence of SUVs we should be able to observe an increase in the diffusion time as the labelled Aβ40 peptides bind to the much slower diffusing SUVs.

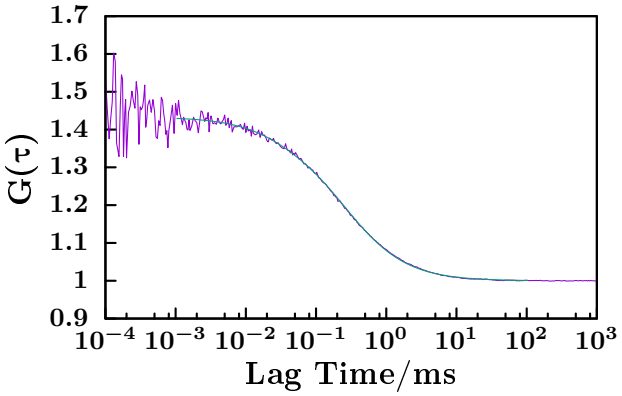


Figure 5.8 – FCS of labelled Aβ monomers. Aβ (3 nM) HEPES NaCl BSA mean diffusion time of three measurements 0.261(6) ms

Before studying the binding of labelled Aβ40 to lipid SUVs, values for the diffusion time of the free peptide and of the SUV need to be determined. Fig. 5.8 shows the FCS trace for Aβ40 monomers which was fit to reveal an average diffusion time of 0.261(6) ms. To determine the diffusion time for an SUV, 100 nm DLPC SUVs were prepared that contained 0.1 % of C_{11}-BODIPY$^{581/591}$ probe, so that they can be observed by FCS.

For an SUV of a given size the number of lipids present in the SUV can be estimated by,

$$\text{no. lipids} = \frac{4\pi r^2 + 4\pi(4-h)^2}{a} \tag{5.1}$$

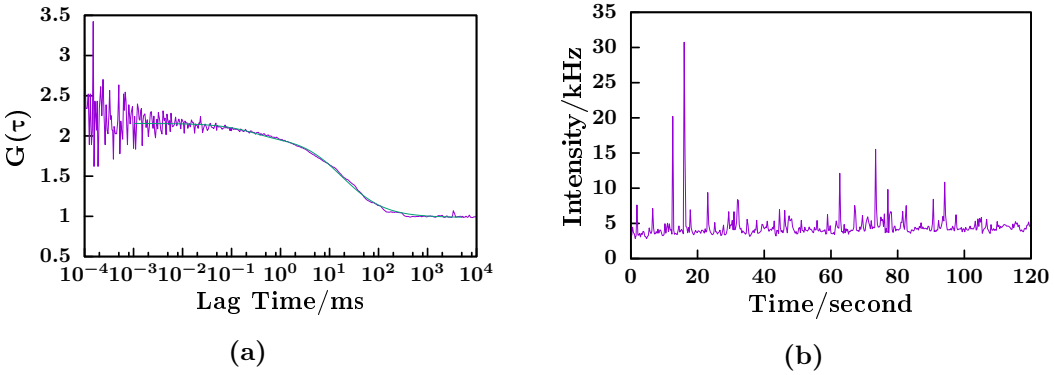


Figure 5.9 – FCS of DLPC SUVs. DLPC 100 nm SUVs with C_{11}-BODIPY$^{581/591}$ (total lipid 1 mM) in HEPES/NaCl. (a) FCS trace showing fitted line. The mean weighted diffusion time was determined to be 15.5(4) ms. (b) Fluorescent intensity fluctuations that generated the FCS trace in (a). Some SUVs appear very bright, likely resulting from multiple fluorophores present.

where r is the radius, h is the bilayer thickness and a is the area occupied by one lipid headgroup. For a DLPC bilayer values for h and a have been reported to be 30.8 Å and 63.2(5) Å^2 respectively.[128] The approximate number of lipid molecules in a 100 nm diameter DLPC SUV can be calculated as $63.6(5) \times 10^3$ lipid molecules. As the total lipid concentration used was 1 mM the concentration of SUVs will be ~16 nM, all of which will contain multiple C_{11}-BODIPY$^{581/591}$ molecules.

The FCS trace for 100 nm SUVs comprised of DLPC is shown in Fig. 5.9(a) with the corresponding intensity trace from which the FCS trace was derived shown in Fig. 5.9(b). The intensity trace shows the presence of some very bright particles, likely containing multiple fluorophores. These rare events have an impact on the longer times scales of the FCS trace and manifest as a less good fit of the data when the fitting function only describes the diffusion of a single species (c.f. Fig. 5.8). As the DLPC SUVs are not all of a single size, but instead are a distribution of sizes centred on 100 nm a FCS equation accounting for two species was used to account for this variation. The fitting revealed that the majority of the FCS amplitude (84 %) is described by a slowly diffusing species, τ_d 18.5(7) ms, with a smaller contribution of a faster diffusing species, τ_d 0.14(3) ms. The mean diffusion time, weighted by the fraction of each species can be calculated to be 15.5(4) ms, for a 100 nm DLPC SUV. This is much greater than the diffusion time of monomeric Aβ40, and so we should be able to use FCS to observe a clear shift in the diffusion time to a slower diffusion when the Aβ40 binds to a DLPC SUV.

Fig. 5.10(a) shows how the FCS of labelled Aβ40 changes over a period of 45 min

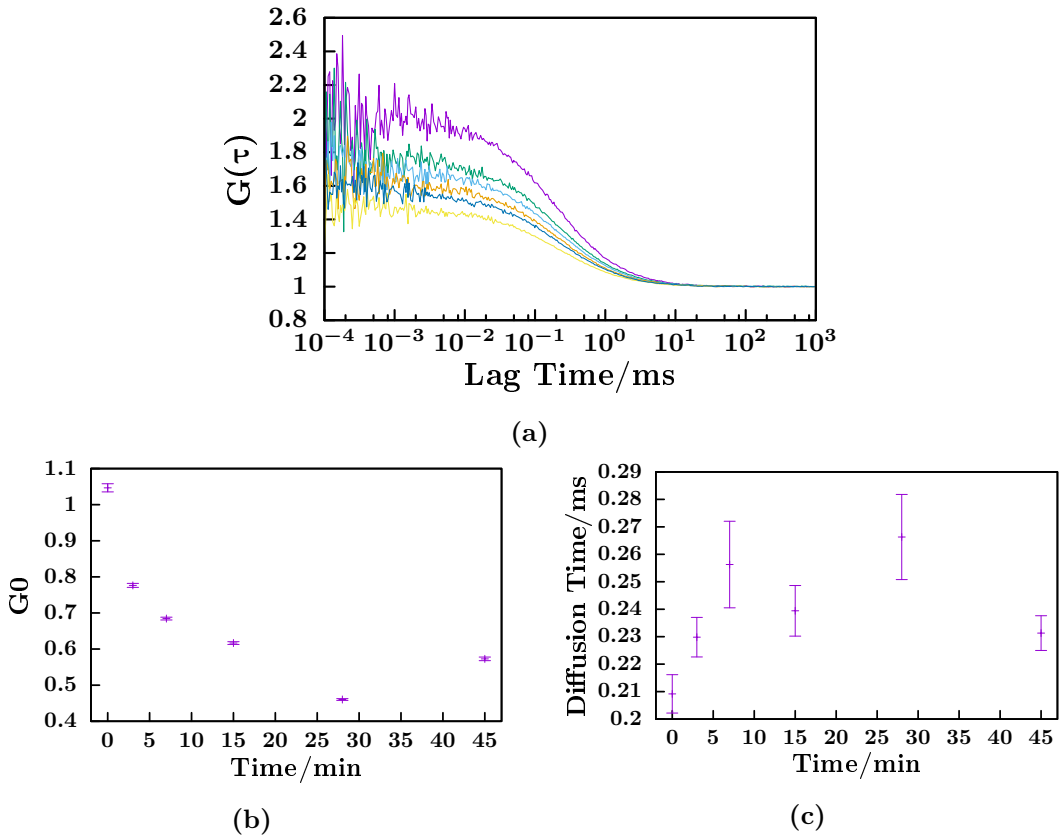


Figure 5.10 – FCS of labelled Aβ binding to DLPC SUVs shows minimal interaction. Fluorescently labelled Aβ40 (3 nM) was mixed with DLPC 100 nm SUVs (total lipid concentration 1 mM) in HEPES/NaCl and FCS traces recorded over time. Data was fit from 1 µs-100 ms.

when added to a solution of 100 nm DLPC SUVs. The change in G0 and diffusion time over the 45 min period are shown in Fig. 5.10(b) and (c) respectively. It can be seen that during the measurement the value of G0 decreases, suggesting that the number of fluorescent particles in solution is increasing. The diffusion time shows a slight increase over the 45 min, which suggests that the labelled Aβ40 molecules may be binding to the lipid SUVs however the increase does not come anywhere close to the 15 ms diffusion time expected for particle bound to a 100 nm SUV.

It has been reported in the literature that lipid microdomains consisting of GM1 can serve as a binding site for the Aβ molecule to a lipid bilayer. For 100 nm SUVs consisting of sphingomyelin, cholesterol and GM1 the K_d has been reported to be ~2 µM.[121]. To try and encourage the binding of Aβ40 to the SUVs the lipid composition was adjusted to containing 10 mole% GM1. Fig. 5.11(a) shows how the FCS of labelled Aβ40 changes over time when added to a solution of 100 nm SUVs

composed of DLPC and GM1. The change in G0 and diffusion time are shown in Fig. 5.11(b) and (c) respectively. The results for Aβ40 binding to DLPC/GM1 SUVs are similar to what was observed for binding to DLPC SUVs, suggesting that the addition of 10 mole% has little effect on the binding of Aβ40, as observed by FCS.

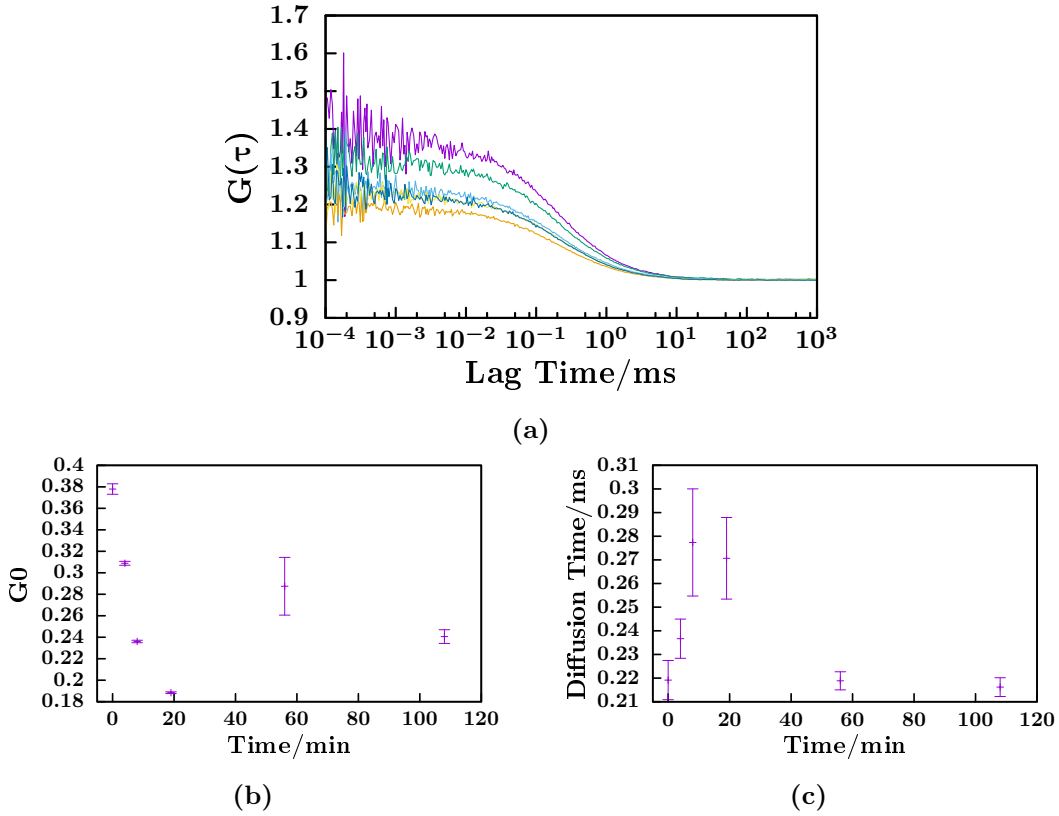


Figure 5.11 – FCS of labelled Aβ binding to mixed DLPC/GM1 SUVs shows minimal interaction. Fluorescently labelled Aβ40 (3 nM) was mixed with DLPC 100 nm SUVs containing 10 mole% GM1 (total lipid 1 mM) in HEPES/NaCl and FCS traces recorded over time. Data was fit from 1 µs-100 ms.

The peroxidation studies of GM1 micelles and DLPC SUVs shown at the beginning of this Chapter were performed with ∼1 µM Aβ40, however concentrations of this magnitude cannot be directly used in FCS experiments, as it would cause the correlation amplitude to be too small for reliable fitting. This is why the above FCS studies were performed with low nM amounts of Aβ40. It could be that at these nM concentrations the Aβ40 is not able to bind to the lipid SUVs. To check this Aβ40 (1 µM) was incubated with DLPC 100 nm SUVs containing 10 mole% GM1 (total lipid 1 mM) in HEPES/NaCl. Samples of the solution were taken and diluted 1000 times before being analysed by FCS. The average of three measurements gave a

diffusion time of 0.211(6) ms, suggesting that the dye was freely diffusing in solution and not bound to the lipid SUVs.

In contrast, when GM1 and labelled Aβ40 are incubated together, (at the concentrations used in the peroxidation measurements) FCS shows that the Aβ40 has become associated with the GM1 micelles, as shown in Fig. 5.12. This figure shows FCS traces (normalised by G0 values determined from fitting of the raw data) for GM1 micelles, freely diffusing labelled Aβ40 and labelled Aβ40 which had been incubated with GM1 micelles for 10 min prior to dilution and measurement.

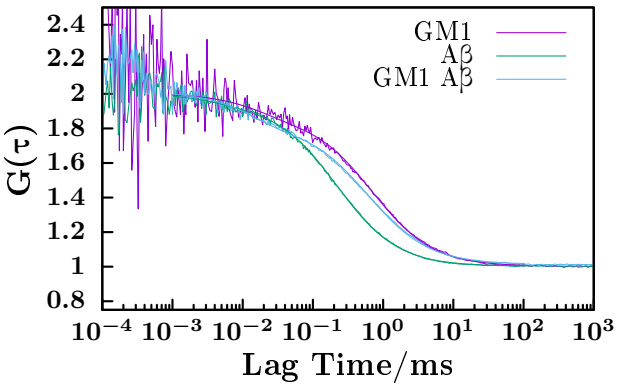


Figure 5.12 – FCS shows that Aβ is able to bind to GM1 micelles. Normalised FCS traces and fitted curves for labelled GM1 micelles, monomeric labelled Aβ40 and labelled Aβ40 that had been incubated with GM1 micelles prior to measurement. Fitting of the data revealed that the diffusion time of the monomeric labelled Aβ40 increased from 0.203(2) ms to 0.418(9) ms when bound to a GM1 micelle. Diffusion time of a GM1 micelle was measured to be 0.54(2) ms.

As FCS has provided no evidence that Aβ40 is able to bind to DLPC SUVs this could explain why the rate of oxidation of DMPC vesicles induced by the Aβ40Cu complex is similar to controls.

5.4 Summary

This chapter attempted to measure the 'damage potential' of the AβCu complex. By using a peroxidation sensitive C_{11}-BODIPY$^{581/591}$ probe, the damage to model lipid membranes caused by redox cycling of the AβCu complex was studied. The disadvantages associated with using a probe which relies on itself being oxidised in order to report on the presence of radicals was discussed. However, the use of a fluorescent probe has its advantages, one being the comparative ease at which peroxidation kinetics can be monitored. Both the total amount of oxidative damage,

and the kinetics of oxidative damage are important parameters to assess.

Initially micelles composed of GM1, a prominent ganglioside found within the brain, where chosen as the model membrane of choice. Lipid peroxidation initiated by AβCu in the presence of ascorbate caused slow but prolonged damage to the lipid membrane. Free Cu in the presence of ascorbate had a higher initial rate of lipid peroxidation, but this was not sustained. Control experiments showed that in GM1 micelles the C_{11}-BODIPY$^{581/591}$ probe suffered from little auto-oxidation, and that by chelating the Cu with EDTA peroxidation was halted.

Interestingly, free Cu in the presence of ascorbate, which can undergo faster redox cycling than if complexed with Aβ showed lower lipid peroxidation compared to AβCu. This points to AβCu being a more effective catalyst of lipid damage than free Cu. This can be explained by localisation. The rapid cycling and radical generation of free copper in solution produces radicals homogeneously throughout the solution. In order to cause damage these radicals must diffuse to the lipid membrane. Aβ was shown to bind to GM1 micelles by FCS. The Aβ molecule will most likely bind through its more hydrophobic C-terminal region, leaving the less hydrophobic N-terminus out in solution, able to bind copper. The copper ions are therefore held next to the lipid membrane, and even though the cycling is slower than free copper, the radicals are being produced right next to the membrane and do not have to diffuse far in order to cause damage.

While the AβCu complex seems to be an effective catalyst of lipid peroxidation when GM1 micelles were used as the model membrane, trying to replicate this in small unilamellar vesicles (SUVs) did not show any effect. In contrast to micelles, which only have one lipid layer, SUVs have a lipid bilayer and so should be a better model for Aβ bound to a synaptic membrane. SUVs can also be made in much larger sizes compared with GM1 micelles and so the lipid packing and curvature are also more similar to what would be found with a cellular lipid membrane. DLPC SUVs of 100 nm were chosen as the model system as DLPC is a fully saturated lipid that has a transition temperature below room temperature. The amount and rate of lipid peroxidation of DLPC SUVs was identical for free copper and the AβCu complex.

This may be explained by the Aβ not being able to bind to the DLPC SUVs. Analysis by FCS gave no clear indication that Aβ can bind to DLPC SUVs at the concentrations used. In contrast, FCS clearly showed that Aβ can bind to GM1 micelles.

Chapter 6

Apolipoprotein E -expression, purification and labelling

The remaining chapters of this thesis switch their primary focus from Amyloid-β to apolipoprotein E (apoE), another protein that is a topic of research in Alzheimer's disease. This chapter first presents a short summary of the research surrounding apolipoprotein E, and then details progress made in the expression, fluorescent labelling, and purification, of apoE.

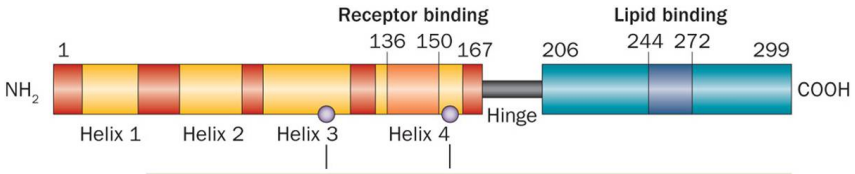
6.1 A Brief Overview of Apolipoprotein E

Apolipoprotein E was introduced in Chapter 1, where it was noted as being the biggest genetic risk factor for developing sporadic Alzheimer's disease. As was discussed, the protein has three isoforms in humans (denoted E2, E3 and E4), differing at two locations within the peptide sequence. The three isoforms are summarised in Fig. 6.1.

6.1.1 Structure and Function

Apolipoprotein E is a ∼34 kDa protein containing 299 amino acids. It functions to transport cholesterol and other lipids throughout the body. ApoE is found in the systemic circulatory system, where it is synthesised primarily by the liver, and the brain, where it is synthesised primarily by astrocytes. Concentrations or apoE have been reported to be ∼1 µM in plasma, and about an order of magnitude lower in the cerebrospinal fluid (∼100 nM).[130,131]

Apolipoprotein E contains two domains, joined together by a flexible, protease sensitive hinge. The N-terminal domain is mostly ∝-helical and contains the region



	Isoform-specific amino acid difference		Allele frequency (%)	
	112	158	General	AD
Apo-E2	Cys	Cys	8.4	3.9
Apo-E3	Cys	Arg	77.9	59.4
Apo-E4	Arg	Arg	13.7	36.7

Figure 6.1 – Schematic of apoE. Diagram showing the locations of the isoform specific amino acid differences. Also illustrated are the two domains present in apoE with the regions responsible for receptor and lipid binding highlighted. Reprinted with permission from Springer Nature. Copyright (2013). [129]

responsible for interacting with its receptors. The C-terminal domain contains the region responsible for lipid binding and has also been implicated in the formation of apoE dimers and tetramers. Due to the predisposition of apoE to form multimers and aggregates at higher concentrations, obtaining structural information about the full-length protein has remained a challenge. The structure of the N-terminal domain however, has been solved by X-ray crystallography and later, solution NMR. A solution NMR structure of a full length 'monomeric' apoE3 was solved by Chen et al. [132] To achieve concentrations high enough to be probed by NMR five hydrophobic residues in the C-terminus were altered (F257A, W264R, V269A, L279Q and V287E), which were shown to produce biologically active, monomeric apoE3. [133]

With structural information in hand, researchers started concluding how a single C112R mutation separating apoE3 from E4 could lead to functional differences through structure. Based on the crystal structure of the N-terminal domain, a salt bridge between Arg61 and Glu255 (spanning the N- and C-domains), was suggested to be present in apoE4. [134] This was proposed to be a direct consequence of the presence of Arg112 in apoE4, and that in apoE3 Arg61 was orientated in such a way as to not be able to form the domain-domain interactions. Later, the Arg61-Glu255 salt bridge was supported by mutational data. [135] The argument was made that apoE4 had stronger domain-domain interactions than apoE3, explaining why altered lipid binding activity was noted between the isoforms. This tighter domain-domain interaction was backed up by several spectroscopic experiments. [136,137]

In contrast to the specific Arg61-Glu255 salt bright identified, the solution NMR structure of monomeric apoE3 revealed the presence of many interactions between the N- and C- domains. [132] Specifically the authors noted that their structures

indicated that Glu225 was instead interacting with Lys95, and not with Arg61. Later, hydrogen-deuterium exchange mass spectrometry data would suggest that all isoforms of apoE have multiple interactions between the N- and C-terminal domains.[138] Using this mass spectrometry data, Frieden et al proposed that lipid binding was governed by intrinsically disordered regions of apoE, although how this mechanism of binding differs for apoE isoform is not clear. Coincidentally, another hydrogen-deuterium exchange mass spectrometry study of apoE was also published in the same year.[139] This study noted that the presence of Arg112 in apoE4 causes a destabilisation of certain helical segments, resulting in apoE4 being less able to form tetramers, and therefore more monomer being present and able to bind lipids.

While structural differences between apoE3 and E4 must govern the differing functions of these isoforms, the search for how one C112R mutation can cause such functional differences is still ongoing.

6.1.2 Apoliporotein E & Amyloid-β Interactions

In an attempt to find where apoE isoform exerts its impact on Alzheimer's disease risk, researchers turned to Aβ. The observation that apoE is found deposited in Aβ plaques gave rise to the idea that apoE could bind to Aβ, and therefore influence AD in this manner.[140] In vitro studies backed up this apoE-Aβ interaction, with a dissociation constant in the tens to hundreds of nM.[141] Many studies have shown that various preparations of Aβ (synthetic, cell derived or purified from CSF) can interact with apoE (recombinant, cell derived or purified from CSF), and that the interaction is apoE isoform specific, although the directionality of this specificity is contested.[142,143] It has been reported that the lipidation status of apoE alters the binding of Aβ with lipid-free apoE having a weaker affinity, and that the oligomeric state of the Aβ can also modulate the binding.[144]

The observation that apoE can bind Aβ led researchers to hypothesise that apoE impacts the progression of AD through altering the clearance of Aβ.[145] It was also suggested that binding of Aβ by apoE might attenuate Aβ oligomerisation,[146] with in vitro evidence showing that as apoE4 prolongs fibrilisation by binding to and stabilising toxic Aβ oligomers.[147] However not everyone agrees that apoE can actually bind Aβ. Using ultracentrifugation, size exclusion chromatography and fluorescence correlation spectroscopy, Verghese et al were unable to observe appreciable binding of Aβ to apoE.[148] They noted that no matter the Aβ or apoE source, only ∼5 % of Aβ was bound to apoE, and argued that prior observations of apoE Aβ complexes were the result of supraphysiological concentrations.

6.1.3 Apolipoprotein E: if not Aβ, then what?

Research has also been directed at identifying Aβ independent roles for apolipoprotein E in Alzheimer's disease.[149] It has been noted that an N-terminal fragment of apoE, consisting of residues 1 - 271, was able to induce the formation of neurofibrillary tangles in neurons.[150] It was also shown that proteolytic cleavage, by this chymotrypsin-like serine protease, was better able to cleave apoE4 than apoE3, and that the apoE4 fragment resulted in greater neurofibrillary tangle formation. This observation was replicated in mice where again, the apoE4 fragment was shown to cause AD-like neurodegeneration, such as abnormally phosphorylated tau.[151] As well as inducing cytoskeletal disruptions, fragments of apoE have also been linked to mitochondrial dysfunction. It has also been argued that (full length) apoE4 can disrupt calcium homeostasis, and that this explains its neurotoxic effect.[152] It is safe to say that the role of apoE in Alzheimer's disease is confusing and often contradictory; the only undisputed fact being the association of apoE4 and increased risk of AD. As every review of this area concludes, apoE clearly plays some role in AD, a role that is likely multifaceted, both dependent and independent of Aβ.

6.2 Purification strategies - a history

The start of every biophysical study of a protein must begin with a reliable source of the protein of interest, in good yields and of high purity. Many strategies for obtaining apolipoprotein E (apoE) have been described including purification of apoE from human plasma,[153] purification from transfected cell lines[142] and bacterial expression systems.[154]

Purification from human plasma represents the most faithful system to study as it is the true wild type protein. However high yields are hard to achieve, and unless the donor is homozygous for APOE isoform, a mixture will be obtained. Furthermore, obtaining protein with mutations present or modifying the protein in some way is difficult if not impossible.

If mutations of the protein are desired, then a recombinant system must be adopted. While there are reports of using transfected mammalian cell lines, by far the most common approach is to use a bacterial system. The first report of a human apoE being expressed in *E. coli* was in 1985.[154] The system simply produced apoE including the leading methionine, with no other modifications or tags to aid purification. This resulted in a multi-step purification being required, lowering the yield obtained, and was further complicated by cell lysis being observed when large

amounts of apoE were present in the cell, resulting in apoE proteolysis.

To overcome cell lysis when large amounts of apoE accumulated within the *E. coli* cell, attempts were made to secrete the protein into the periplasm through the addition of signal peptides being attached to the N-terminus.[155,156] Around the same time attempts were made to aid with the purification of apoE. By adding a simple polyhistidine tag purification was greatly simplified.[157] However the protein aggregated within the cell and without the ability to remove the polyhistidine tag changes to the protein's biological and physical properties may be present.

It was not until 1999 that all of the advantages were combined into one system that allowed the purification of apoE that was non-toxic to *E. coli*, remained soluble at high concentrations and had a tag for easy purification which could be subsequently removed to leave an (almost) wild-type protein.[158,159] The system made use of the fusion protein thioredoxin being added to the N-terminus, which under the vector's T7 promoter, allowed high levels of expression while remaining in the soluble fraction of the bacterial lysate. A polyhistidine tag facilitated easy purification which could then be removed (along with the thioredoxin) by the inclusion of a thrombin cleavage site. Cleavage of protein tags often leaves what is referred to as a 'cleavage scar', which are residues necessary for the cleavage recognition site that are left attached to the N-terminus of the protein. In this case two amino acids (Gly-Ser-) are left appended to apoE.

The addition of a thrombin cleavage step introduced new problems. The flexible hinge region of apoE, joining the N- and C- termini is sensitive to proteolytic cleavage. And thrombin is a promiscuous enough enzyme to cleave this off target site. This was circumvented by protecting the hinge by complexing the protein with lipid, however requiring lipidation and delipidation steps be added to the process. This was improved upon in 2011 by replacing the thrombin cleavage with a much more specific cleavage provided by the human rhinovirus 3C protease.[160] This protease did not have the off target effect that plagued thrombin cleavage, removing the need for lipidation and delipidation steps and greatly streamlining the apoE purification.

6.3 Current purification strategy

ApoE expression in *E. coli*

The purification protocol used within this work is based off the protocol described in 2011 by L. Argyri et al.[160] with minor adaptations. Plasmids for apoE3 & apoE4 (pET32-E33C & pET32-E43C) were obtained as a very generous gift from Dr Angeliki

Chroni (Institute of Biology, National Center for Scientific Research "Demokritos", Agia Paraskevi, Athens 15310 Greece).[160,161] The vectors were sequenced and found to contain either apoE3 or E4 with the thioredoxin fusion protein, a polyhistadine tag and a human rhinovirus 3C protease (3C protease) as described in Section 6.2.

E. coli BL21(DE3)-RIL cells were transformed via heatshock with either the pET32-E33C or pET32-E43C vector and grown on Luria–Bertani (LB) agar plates containing 100 µg ml^{-1} ampicillin and 25 µg ml^{-1} chloramphenicol at 37 °C for 16 h. A single colony was selected and used to inoculate 8 mL of LB containing 100 µg ml^{-1} ampicillin and 25 µg ml^{-1} chloramphenicol which was grown overnight at 37 °C.

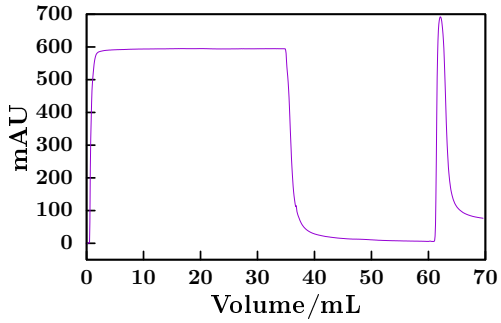
500 µl of this overnight culture was mixed with 500 µl of 50 % autoclaved glycerol to make a glycerol stock and stored at −80 °C. Future overnight cultures were made from these stocks.

An overnight culture of 8 ml was used to inoculate 800 ml of LB containing 100 µg ml^{-1} ampicillin and 25 µg ml^{-1} chloramphenicol. This was grown at 37 °C with agitation until the $A_{@600\,nm} \sim 0.7$. Protein expression was induced by addition of 0.5 mM isopropyl β-d-thiogalactopyranoside (IPTG). The cells were incubated at 37 °C with agitation for a further 2 h before being harvested at 9000 g for 30 min at 4 °C. The cell pellet was frozen and stored at −80 °C.

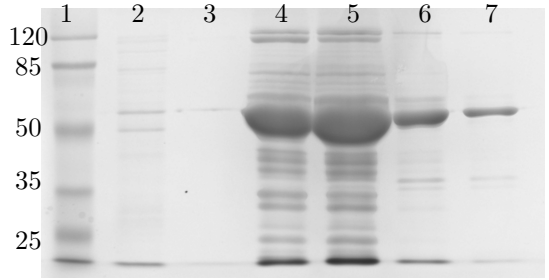
ApoE purification

Pelleted cells containing the apoE3 or E4 fusion protein were thawed on ice and resuspended in Tris-HCl buffer pH 7.5 (50 mM tris, 0.5 M NaCl), containing 10 mM imidazole, to a final volume of 40 ml. A protease inhibitor tablet was added (Pierce Protease inhibitor EDTA free) before the cells were lysed using sonication on ice. Cellular debris was pelleted by centrifugation at 35 000 g and 4 °C for 1 h. The supernatant was filtered through a 0.22 µm syringe filter before being loaded, via a superloop, onto an ÄKTA fast protein liquid chromatography (FPLC) system equipped with a Ni^{2+} affinity column (GE Healthcare HisTrap HP, 1 ml). Sample was loaded and column was washed with 30 ml Tris-HCl pH 7.5 buffer containing 10 mM imidazole followed by elution with 30 ml Tris-HCl pH 7.5 buffer containing 250 mM imidazole, with fractions of 1 ml being collected. Samples of each fraction were analysed by SDS-PAGE to verify purification step before continuing (Fig. 6.2).

The majority of the trx-apoE fusion protein usually eluted within two 1 mL fractions, with lower quantities present in subsequent fractions. The protein was desalted using a PD-10 desalting column (GE Healthcare) loading 2.5 mL of the most concentrated fractions and following the manufactures protocol, obtaining the



(a) UV ÄKTA trace



(b) SDS-PAGE

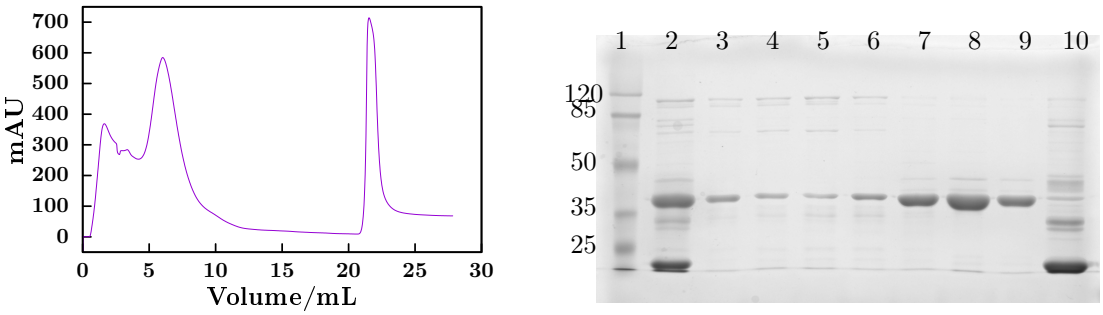
Figure 6.2 – Purification of trx-apoE fusion protein by Ni^{2+} affinity column. (a) UV trace from the ÄKTA FPLC, after loading the protein mixture onto the column the column was washed until no the UV trace reached close to zero at which point the buffer was switched to high imidazole to elute the bound trx-apoE. (b) SDS-PAGE gel of the fractions obtain from (a) lane 1 - molecular weight ladder, lane 2 - flowthrough from column containing cellular proteins that did not bind to the Ni^{2+} column, lanes 3-7 1 mL fractions from the column elution showing large amounts of trx-apoE as well as protein contamination from non specifically bound proteins from the cell lysate.

protein in 3.5 mL Tris-HCl buffer pH 7.5 (50 mM tris, 0.5 M NaCl).

Protein concentration of trx-apoE fusion protein was determined using a PerkinElmer LAMBDA 25 UV-Vis spectrometer and theoretically determined extinction coefficient $\varepsilon_{280\,\mathrm{nm}} = 58\,565\,\mathrm{M}^{-1}\,\mathrm{cm}^{-1}$ as determined by ExPASy, Bioinformatics Resource Portal, ProtParam and the amino acid sequence.

Cleavage of the fusion tag to release apoE was performed on the purified trx-apoE protein. 3C protease (expressed and purified as detailed below) was used at a molar ratio of 1:10 enzyme to substrate (substrate concentration was typically $\sim 40\,\mu\mathrm{M}$) with the addition of 1 mM dithiothreitol. The sample was incubated at 4 °C with rolling for 16 h.

The cleaved protein was then loaded onto an ÄKTA FPLC system equipped with a Ni^{2+} affinity column and purified using the same protocol as outlined previously however this time the cleaved apoE protein (now lacking a polyhistidine tag) was found in the flowthrough while the trx fusion protein was retained on the column. A typical ÄKTA UV trace and SDS-PAGE analysis are shown in Fig 6.3. Fractions containing the apoE fragment were combined and concentrated to 2.5 mL before being buffer exchanged using a PD-10 desalting column (GE Healthcare) equilibrated in 4 M Guinadinium-HCl Tris-HCl buffer pH 7.5 (50 mM tris, 100 mM NaCl). A Centriprep YM-10 (Millipore) centrifugal concentration was used throughout this work. Other devices can concentrate the protein to too high levels right next to



(a) UV ÄKTA trace

(b) SDS-PAGE

Figure 6.3 – Purification of apoE protein by 'inverse' Ni^{2+} affinity column. (a) UV trace from the ÄKTA FPLC. (b) SDS-PAGE gel showing fractions from (a) lane 1 - molecular weight marker, lane 2 - sample after digestion, prior to purification, lanes 3-9 1 mL fractions from the column flow through showing the presence of cleaved apoE, lane 10 - elution from the column showing the presence of the cleaved trx fusion domain. Note that most of the non-specifically bound proteins present in the first Ni^{2+} purification, also bind here as well, as such a highly pure protein can be obtained without the need for further size exclusion chromatography.

the membrane which can promote aggregation. Protein concentration of apoE was determined using a PerkinElmer LAMBDA 25 UV/Vis spectrometer and theoretically determined extinction coefficient $\varepsilon_{280\,\mathrm{nm}} = 44\,460\,\mathrm{M}^{-1}\,\mathrm{cm}^{-1}$ as determined by ExPASy, Bioinformatics Resource Portal, ProtParam and the amino acid sequence. The protein was aliquoted, flash frozen in liquid N_2 and stored at $-80\,^{\circ}\mathrm{C}$.

6.3.1 Recombinant production of 3C protease

A plasmid containing the cDNA for 3C-protease was present in the lab, however the vector encoded for a GST tagged protein and not the 6x His tagged protein that was desired. Upon sequencing it was found that the region encoding for 3C was flanked by BamHI and EcoRI restriction sites and so a double digest of the plasmid using BamHI and EcoRI restriction endonucleases (New England Biolabs) was performed and verified using 1 % agarose gel electrophoresis. An empty plasmid encoding for a 6x His tag and containing BamHI and EcoRI restriction sites, (in frame and in the correct orientation) was similarly cleaved and the 3C fragment ligated in place using T4 ligase (New England Biolabs). The plasmid was first amplified in XL1-Blue *E. coli* as described above and the sequence verified by sequencing.

For 3C-protease expression, amplified plasmid was transformed into BL21(DE3)-RIL in an analogous way to that of apoE with the following differences. The culture was incubated to an absorbance of $A_{@600\,\mathrm{nm}} = 0.5$ ($\sim$6 h) before being induced with

IPTG (0.5 mM). For optimal expression, cells were grown after induction at 20 °C for 16 h before harvesting as before.

3C-protease was purified using Ni^{2+} affinity chromatography in an analogous way to apoE, with the addition of 0.2 % (by volume) Tween-20 added to the buffer. Fractions were analysed by SDS-PAGE and those containing 3C-protease were combined (6 ml) and dialysed using a 10 kDa cutoff membrane against a 200x excess of tris (50 mM), pH 7.5 NaCl (0.5 M) & 10 % by volume glycerol, overnight (16 h) at 4 °C. Protein concentration of 3C-protease was determined using a PerkinElmer LAMBDA 25 UV/Vis spectrometer and theoretically determined extinction coefficient $\varepsilon_{280\,\mathrm{nm}} = 6085\,\mathrm{M}^{-1}\,\mathrm{cm}^{-1}$ as determined by ExPASy, Bioinformatics Resource Portal, ProtParam and the amino acid sequencing results. 3C-protease was aliquoted and snap frozen in liquid N_2 and stored at −80 °C.

6.4 Fluorescent labelling strategies

Many options exist for the addition of a fluorophore to a protein of interest. The most common can loosely be grouped into either those that require the addition of a small fluorescent molecule and those that exploit the intrinsic fluorescence of amino acids.

6.4.1 Intrinsic fluorophores

The three naturally occurring amino acids that display fluorescence are tryptophan, tyrosine and phenylalanine, and while all could be used tryptophan fluorescence is more commonly employed. This is mostly due to tryptophan's higher absorptivity ($5600\,\mathrm{M}^{-1}\,\mathrm{cm}^{-1}$ vs. $1400\,\mathrm{M}^{-1}\,\mathrm{cm}^{-1}$ for tyrosine and $200\,\mathrm{M}^{-1}\,\mathrm{cm}^{-1}$ for phenylalanine), and quantum yield (0.20 vs. 0.14 and 0.04 for tyrosine and phenylalanine respectively). For apoE there are seven tryptophan residues, four tyrosines and three phenylalinines. Tryptophan fluorescence has been employed to study various aspects of apolipoprotein E, such as tetramer dissociation kinetics in the presence of the quencher acrylamide.[162] However due to there being seven tryptophans in apoE you may need to mutate out a number of them to if you want to unambiguously define the location of the fluorophore, for example in a FRET based study. The low absorptivity and quantum yield (relative to a synthetic fluorophore) also limits its usefulness. While single molecule studies using tryptophan fluorescence have been reported, the protein studied contained 156 tryptophan residues, likely chosen in order to produce a strong enough signal to be observed above the instrument

noise.[163] As the majority of proteins do not contain this many tryptophan residues, the use of tryptophan fluorescence for single molecule study remains limited.

The grouping of intrinsic fluorophores can be stretched to include the encoding of fluorescent fusion proteins such as the widely used green fluorescent protein and its chromatic variants. These overcome the weak fluorescence associated with tryptophan as they have an absorptivity of at least an order of magnitude higher and a quantum yield in most cases >0.5. This approach has been utilised in the study of apoE, whereby yellow fluorescent protein and cyan fluorescent protein were fused to the N- and C-termini respectively in a FRET based study.[137] They noticed that neuronal cells expressing the apoE4 variant displayed a FRET signal, while those expressing apoE3 did not, suggesting that apoE4 has a more compact structure displaying domain-domain interactions whereas the apoE3 isoform has a more open structure. The disadvantage of this approach is the relatively large sizes of these fusion proteins, especially when two are added to produce a FRET pair. To put this in context the FRET pair used in the study previously mentioned have a combined mass of ∼57 kDa for the fluorescent parts alone which actually surpasses the mass of apoE (∼36 kDa). To probe a protein by more than doubling its mass may have consequences on the structure of the protein, and must have consequences on its function. Especially regarding the protein's diffusion and internal dynamics of its domains.

6.4.2 Covalent Small molecule fluorophores

Small molecule fluorophores which are covalently attached to a protein of interest overcome both of the disadvantages of intrinsic fluorophores, by being small in size relative to the size of the protein and by being bright fluorophores. The clear disadvantage is that these fluorophores must be attached to the protein of interest via some reactive handle on the protein. A common method is to use amide NHS ester reaction to add a label to either the N-terminal amine or the side chain of lysine resides. This has the disadvantage of lysine being a relatively common amino acid and so many fluorophores may be added to the protein of interest, resulting in not knowing the exact location of the fluorophore or indeed how many fluorophores are on any given molecule. To overcome the frequency of lysine residues hampering it usefulness a cysteine maleimide reaction may be utilised. Cysteine has the advantage of being a much less common amino acid, with many proteins having only few or even no cysteine residues. In the case of apoE the E4 variant has no cysteines while the E3 variant has one cysteine in position 112 and the E2 variant has cysteines in positions 112 and 158.

Studies involving apoE usually replace cysteine 112 in apoE3 with serine and introduce cysteines elsewhere to add fluorophores. When introducing any mutation, one must be certain that the mutation doesn't change the structure or function of the protein. As the difference between the E3 and E4 isomers is a cysteine to arginine mutation at position 112, the protein's function is likely highly sensitive to mutations in this region of the protein. Researchers go to great lengths to confirm that removing the cysteine in position 112 has no impact on the proteins folding or function for example through circular dichroism, or functional assays. However small differences may not be picked up on.

To avoid having to replace the cysteine, but still add a reactive handle to attach a fluorophore, the approach of adding an unnatural amino acid could be utilised. However, while this technique is becoming more prevalent, it still presents technical challenges. This is particularly the case when trying to introduce two unnatural amino acids for a FRET pair, and has not yet been applied to the study of apoE.

When adding a fluorophore to the middle of a protein its impact on the local folding and dynamics of the protein must be considered. Whether the fluorophore is on the surface of the protein or buried in the core can make a huge difference. From the structures of apoE that have been determined, the N- and C-termini appear to be on the surface of the protein and also lack a defined structure. They therefore present an attractive position for which to attach a fluorophore.

Several options exist to add a fluorophore to the N-terminus of a protein, such as native chemical ligation where by a an N-terminal cysteine reacts with a labelled thioester, initially reversibly through the thiol, before undergoing an intramolecular S,N-acyl shift to generate a stable amide bond between the amine of the N-terminal cysteine and the label. Native chemical ligation has been reported as a tool for the fluorescent labelling of proteins however it is not widely employed.[164] Another approach is to use an enzyme to attach a label to the N-terminus of a protein, such as the enzyme sortase A.

6.4.3 Sortase A labelling

Sortases are a class of enzymes found in bacteria. Their function is to permanently anchor proteins to the bacteria's cell surface, which they accomplish through recognition of a specific sequence on the protein's C-terminus, cleavage of this sequence and transpeptidation of the protein to an anchor on the cell membrane.[165] The use of sortases (or 'sortagging') has been widely reported as an efficient means of protein modification including protein labelling.[166,167,167] A commonly used sortase enzyme

(and the one employed in this thesis) is a truncated form of SrtA from *Staphylococcus aureus*, which has been deposited in the Addgene plasmid bank. Depending on the location of the recognition motif, probes can be either attached to the N- or C-terminus of a protein of interest.

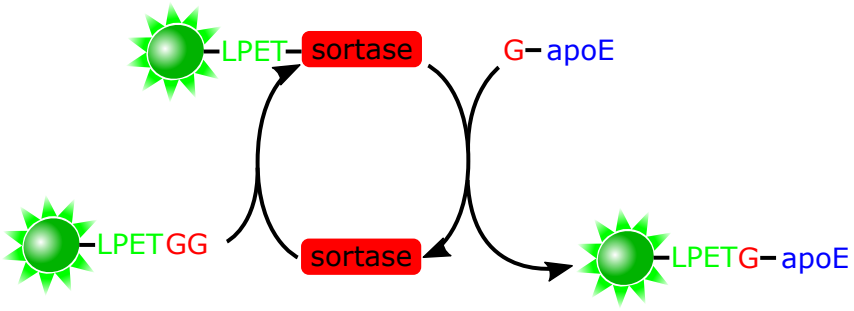


Figure 6.4 – Schematic of labelling via sortase enzyme. Sortase enzyme recognises the LPETG motif which has been attached to a fluorophore (green sphere), and cleaves the recognition motif between the threonine and glycine. The sortase then transfers the labelled peptide onto apoE, which must have a glycine at it N-terminus.

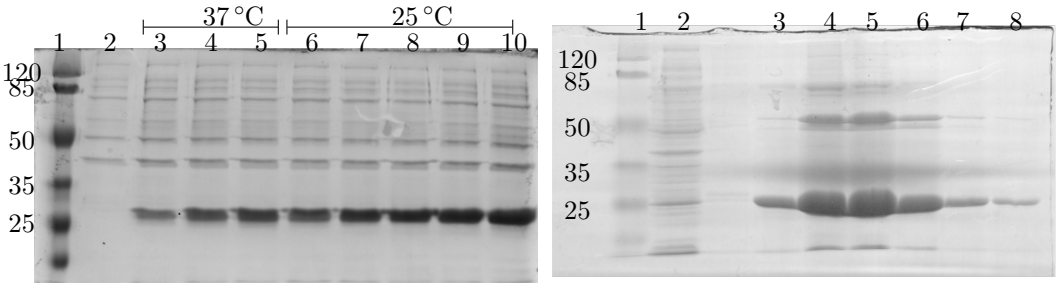
Fig. 6.4 shows a scheme of how enzymatic N-terminal labelling by sortase can occur. This sortase recognises the motif LPXTG (where X can be any amino acid, but is often glutamic acid as it is commonly found in the natural sortase A substrates) and cleaves between the threonine and glycine. The motif is loaded onto the enzyme through a cysteine in its active site, generating an acyl-enzyme intermediate. A protein, containing at least one glycine nucleophile at it's N-terminus, can then attack the acyl-intermediate, releasing the enzyme and ligating the two parts together.

6.5 Fluorescent labelling of the N-terminus of apolipoprotein E

For N-terminal labelling via sortase, the protein to be labelled must have at least one glycine to act as the nucleophile. The current method described in Section 6.3 using 3C-protease to cleave the thioredoxin fusion protein releasing apoE results in the addition of GPGS to the N-terminus, allowing us to use this in sortase labelling.

6.5.1 Recombinant production of Sortase $A_{\Delta 59}$

The plasmid encoding for Sortase $A_{\Delta 59}$ (pET28a-SrtAdelta59) was purchased from Addgene deposited by the Ploegh lab.[168] The plasmid encodes for a N-terminal His



(a) SDS-PAGE of expression trial

(b) SDS-PAGE of purification

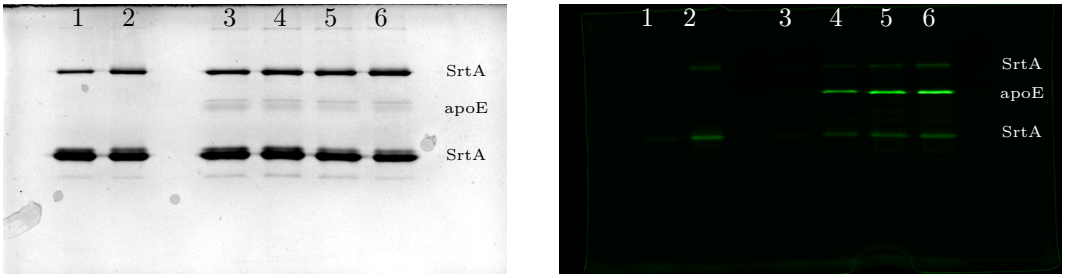
Figure 6.5 – Optimisation of SrtA purification. (a) Lane 1 - molecular weight ladder, lane 2 pre-induction sample, lanes 3-5 incubation at 37 °C at 1, 2 and 3 h post induction, lanes 6-10 incubation at 25 °C at 1, 2, 3, 4 and 20 h post induction. (b) Lane 1 - molecular weight ladder, lane 2 flow through from Ni^{2+} affinity column, lanes 3-8 elution from Ni^{2+} affinity column in 1 ml fractions.

tagged version of SrtA with kanamycin selection. The pET28a-SrtAdelta59 plasmid was transformed into BL21(DE3)-RIL via heatshock. A culture was grown at 37 °C with agitation until a $A_{@600\,nm}$= 0.8 (∼3 h) was reached, at which point the culture was induced by the addition of IPTG (0.5 mM). To determine the optimum expression conditions cultures were incubated after induction at 37 °C for 3 h and 25 °C for 20 h (Fig. 6.5). Expression at 25 °C gave the optimum yield, however there was not much added benefit for incubating for times longer then 4 h at this temperature.

Harvested cells from a 1 l culture were resuspended in 25 ml of 50 mM Tris pH 7.5 containing 150 mM NaCl, 10 mM imidazole and 10 % glycerol (by volume) with a protease inhibitor tablet (Pierce Protease inhibitor EDTA free). Cells were lysed by sonication before being purified by affinity chromatography using an ÄKTA (FPLC) system equipped with a Ni^{2+} affinity column (GE Healthcare HisTrap HP, 1 ml). The column was washed with the same buffer as used for resuspension, and eluted in the same buffer but containing 500 mM imidazole. Fractions containing SrtA were combined and dialysed twice against a 200x excess of resuspension buffer without the addition of any imidazole. The second band at ∼ 50 kDa is likely a disulphide dimer of SrtA as it was not present on SDS PAGE when samples were reduced prior to analysis. The concentration of SrtA was determined using UV-Vis spectroscopy using an extinction coefficient of $\varepsilon_{280\,nm} = 17\,420\,M^{-1}\,cm^{-1}$. The protein was aliquoted, flash frozen in liquid N_2 and stored at −80 °C.

6.5.2 Labelling trial with fluorescein

In order to optimise the labelling, and further purification conditions the cheaper fluorescein (FAM) dye was used in place of the more expensive, bright and photostable dyes typically needed for single molecule spectroscopy. The labelling reactions were carried out at 37 °C in sortase labelling buffer (50 mM Tris, pH 7.5 containing 150 mM NaCl and 10 mM $CaCl_2$).



(a) SDS-PAGE stained for protein **(b)** SDS-PAGE fluorescently scanned

Figure 6.6 – Labelling of apoE by sortase. (a) & (b) display the same gel stained for total protein or fluorescently scanned. Lanes 1 & 2 show a control labelling reaction without the addition of apoE at time points t = 0 & 5 h respectively. Lanes 3-6 show a labelling reaction at time points t = 0, 1, 3 & 5 h. Labelling conditions, final concentrations: apoE4 (4.7 µM), SrtA (20 µM), FAM-peptide (0.5 mM) in sortase labelling buffer.

Fig 6.6 shows time points from a labelling reaction analysed by SDS-PAGE and then stained for total protein and fluorescently scanned. Lanes 1 & 2 in both figures show that in the absence of any apoE no fluorescent band is detected at the expected molecular weight. The sortase enzyme is present as a mixture of monomer and dimer, presumably a disulphide bridged dimer as upon reduction the higher molecular weight band disappears (data not shown). But more interestingly, the sortase enzyme itself also appears to undergo a degree of labelling. This labelling is unlikely to be a result of non-specific binding as the addition of SDS to the samples prior to analysis should remove non-specific interactions, and as the enzyme does not have an N-terminal glycine, it cannot act as a nucleophile in the labelling reaction. It is possible that the labelling being observed is the acyl-enzyme intermediate, with the dye attached to the active site cysteine, but how labelling of the dimer is also present when the cysteine is conjugated to the dye is unclear. Lanes 3 - 6 in both figures show that when apoE is present a fluorescent band at the anticipated molecular weight is observed. The degree of labelling increases in a time dependant manor and appears to be complete within ca. 3h. Reassuringly the intensity of the labelled apoE is greater than the

background labelling of the sortase, even though the sortase concentration is ca. 5 times greater than the concentration of apoE. However, it can be seen that even when ca. 100 times excess of fluorescent probe is used the reaction has not resulted in complete labelling of apoE as unlabelled apoE can still be detected on the gel.

Following purification, analysis by UV-Vis showed that only 30 % labelling efficiency had been obtained for the FAM-apoE.

6.5.3 Purification of the labelled apoE

Following labelling, the SrtA enzyme and unreacted probe must be removed from the newly labelled apoE. As SrtA has a His tag and the apoE protein does not, affinity chromatography was chosen. As the labelling reaction was typically only a few hundred microliters, trying to use a Ni^{2+} column attached to an ÄKTA FPLC system resulted in no recovery of the labelled apoE. Small scale affinity purification was carried out in an eppendorf by incubating a 100 µl reaction with 200 µl of Chelating Sepharose Fast Flow (GE Healthcare) beads charged with $NiCl_2$ at room temperature for ∼1 h. The supernatant was removed and the beads washed three times with 100 µl 10 mM Tris pH 7.5, 150 mM NaCl, 10 mM imidazole, and then eluted with the same buffer but with 500 mM imidazole. An example of this purification is shown in Fig. 6.7. It can be seen that while the small scale affinity purification is effective in removing the SrtA , a high proportion of the FAM-apoE is also non-specifically binding to the Ni^{2+} beads. In order to recover all of the labelled apoE concentrations of imidazole in the wash buffer had to be increased to 100 mM however at this concentration a portion of the SrtA would also be eluted. 50 mM imidazole in the wash buffer was found to be the highest that could be used while still removing all of the SrtA.

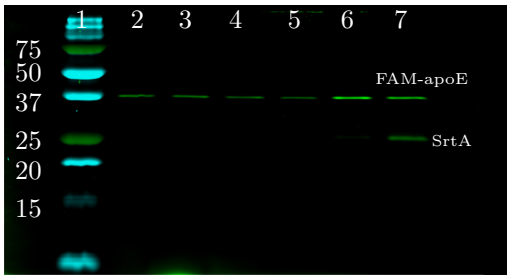


Figure 6.7 – Purification of labelled apoE. Fluorescently scanned gel showing Ni^{2+} purification of the labelling reaction. Lane 1 - molecular weight ladder, lane 2 supernatant after incubation with Ni^{2+} containing beads, lanes 3-5 beads being washed, lanes 6 & 7 sample elution.

Recovery of the labelled apoE from the Ni^{2+} purification beads was further

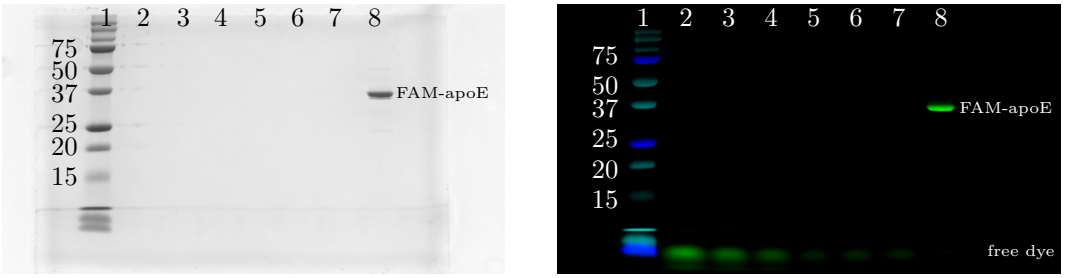
enhanced by the use of a home made His spin column. By placing ∼200 µl of Chelating Sepharose Fast Flow (GE Healthcare) beads charged with $NiCl_2$ into an empty Micro Bio-Spin column (Bio-Rad), the beads could be incubated, washed and eluted as before but using centrifugation (rather than pipetting) to recover all of the sample.

To remove the excess of unreacted probe a Micro Bio-Spin P-6 column (Bio-Rad) was trialled. While the amount of free probe did decrease, even after two consecutive Micro Bio-Spin P-6 (size exclusion) columns there was still a substantial amount of free dye remaining in the sample. Further Micro Bio-Spin P-6 columns were not attempted as not all of the FAM-apoE was being recovered after each size exclusion step. PD10 desalting columns (GE Healthcare) were also trialled and found to be ineffective at removing the free unreacted dye, however the weight of the dye peptide is approaching the molecular weight cut off of these devices (∼1 kDa), and so perhaps should not be expected to work.

Dialysis using a Pur-A-Lyser Mini dialysis tube (25 kDa MWCO) (Sigma Aldrich) was also attempted, however the dialysis was very slow. Even with a 2,500x excess of buffer the concentration of free probe only dropped by a factor of four over a 20 h dialysis at room temperature. The addition of detergents such as Tween-20 (0.1-1 %) or denaturation (by adjusting to 6 M urea) did not increase the rate of dialysis.

Size exclusion chromatography using a TSK-GEL g3000 PWxl (TOSOH BIOSCIENCE) on an HPLC instrument was trialled as a possible way to remove the free dye from the small labelling reaction volume. Following removal of SrtA using the home made His spin column the samples was injected onto the column. This column is typically used for the chromatography of water-soluble polymers up to 50 kDa. The use of an ÄKTA FPLC equipped with a Sephacryl 200HR size exclusion column was also trialled. While both of these methods separated the labelled protein from the free dye, the vast excess of free dye resulted in large amounts of peak broadening for the free dye and only the leading edge of the FAM-apoE peak was found to not contain any trace of free dye. As such a pure protein could be obtained but at a greatly reduced yield.

The most optimal method found for effective removal of the unreacted dye peptide was to use a centrifugal concentrator. As mentioned in Section 6.3 concentration of apoE should ideally be done in a Centriprep YM-10 (millipore) concentrator, as other devices cause concentrations beside the membrane to become too high and aggregation of apoE. Ideally the protein should also be denatured while concentrating. Denaturation of the sample can be achieved by adjusting the buffer to 4 M guinadinium-HCl or 6 M urea. While either can be used if SDS-PAGE analysis is



(a) SDS-PAGE stained for protein **(b)** SDS-PAGE fluorescently scanned

Figure 6.8 – Optimised purification of labelled apoE. (a) & (b) display the same gel stained for total protein or fluorescently scanned. Lane 1 - molecular weight marker, lanes 2-7 filtrate from consecutive buffer exchanges by Centriprep YM-10 spin concentration, showing decreasing amounts of free dye, lane 8 - retentate from Centriprep YM-10 spin concentration showing labelled apoE in the absence of any free dye.

intended urea is best used as guinadinium-HCl precipitates in the presence of SDS and makes gel loading difficult.

The flowthrough from the Centriprep YM-10 devices can be replaced with buffer containing denaturant several times while monitoring the absorbance at 505 nm until the reading is constant suggesting that all unreacted peptide has been removed (Fig. 6.8).

It should also be noted that the SrtA enzyme should be removed before the free dye is removed as the enzyme can catalyse the reverse reaction which will become dominant if the free dye concentration decreases. Denaturation of the sample immediately following the labelling reaction can prevent this and is recommended.

6.5.4 Labelling with Atto-488

Labelling with the Atto-488 dye was carried out in a similar manner to labelling with fluorescein. Typically a 100-600 µl reaction containing apoE4 (10 µM), SrtA (20 µM), Atto488-peptide (0.5 mM), in sortase labelling buffer (50 mM Tris, pH 7.5 containing 150 mM NaCl and 10 mM $CaCl_2$) was incubated at 37 °C for 3 h. Following purification the labelling efficiency was determined by UV-Vis spectroscopy and was typically between 15-30 % labelled peptide.

6.5.5 Improving the labelling efficiency

A disadvantage of using an enzymatic labelling reaction is that the enzyme is capable of catalysing the reverse reaction as well as the forward. The equilibrium (and

maximum labelling efficiency) therefore depend on the relative apparent rates of the forward and backward reactions. Even when using a large excess of dye to try and drive the equilibrium more towards the labelled protein side of the reaction, the labelling efficiency was never greater that ∼30 %. This suggests that the forward reaction is highly inefficient and that the protein molecule is simply not a very good nucleophile. Every time the sortase successfully recognises and cleaves a probe molecule it generates a peptide fragment consisting of two glycine molecules. This dipeptide is able to act as a nucleophile in the labelling reaction, and due to its small size would be a very fast diffusing and sterically unhindered nucleophile. Therefore, to improve the labelling efficiency we must make the N-terminal glycine on our protein of interest a more competitive nucleophile.

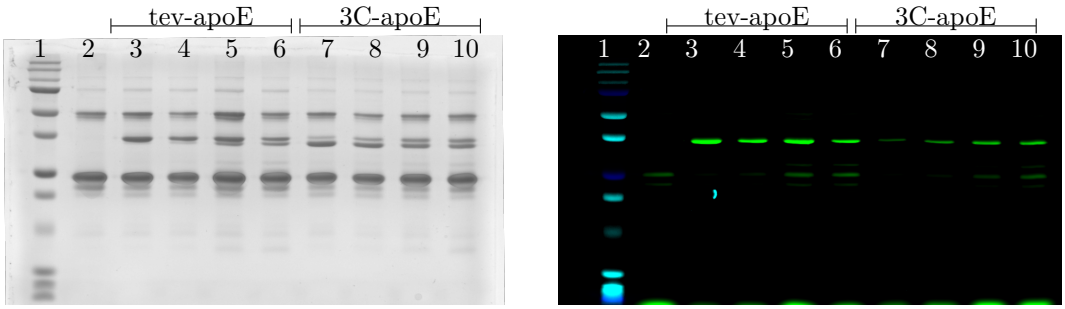
Increasing the number of N-terminal glycines

There is evidence in the literature that varying the number of glycine amino acids at the N-terminus can have an effect on the labelling reaction.[169] Although the rationale behind this is unclear, some proteins appear to 'prefer' between 1 & 5 glycine amino acids, with this preference having to be determined empirically for each protein.

As discussed in Section 6.3 the current method for producing apoE utilised the cleavage of the fusion protein by the human rhinovirus 3C protease. This leaves a 'protease scar' of Gly-Pro-Gly-Ser- immediately preceding the leading methionine of apoE. However, the proline in the P2' position is a requirement for 3C protease activity and so cannot simply be replaced with a glycine in order to increase the number of N-terminal glycines. Further, the unusual side chain bonding of a proline amino acid, which confers an exceptional conformational rigidity to the surrounding structure, could also be having an impact of the ability of the glycine nucleophile to adopt a conformation that favours the approach towards the probe-enzyme intermediate.

In order to remove the proline a new enzyme will need to be used, one which remains as specific as 3C but which has flexibility in the amino acids downstream of the cleavage site. The protease from Tobacco Etch Virus (TEV) has an optimal consensus sequence of ENLYFQ↓S, however it is known that it does have more substrate promiscuity than 3C protease. The serine in the P1' position can be replaced with any small hydrophobic or polar residue. Even though glycine is not polar, or particularly hydrophobic, its small size allows it to be used in this position.

The cleavage site was changed from 3C to TEV using site directed mutagenesis and confirmed by sequencing. The use of TEV produced a 'protease scar' of Gly-



(a) SDS-PAGE stained for protein **(b)** SDS-PAGE fluorescently scanned

Figure 6.9 – Making apoE a better nucleophile. (a) & (b) display the same gel stained for total protein or fluorescently scanned. Lane 1 - molecular weight marker, lane 2 - control reaction without apoE, lanes 3-6 - labelling reaction using tev-apoE at time points 0.25, 1, 3 & 6 h, lanes 7-10 - labelling reaction using 3C-apoE at time points 0.25, 1, 3 & 6 h. Labelling conditions, final concentrations: apoE4 (50 µM), SrtA (100 µM), Atto488-peptide (1 mM)

Gly-Gly-Ser-, thereby increase the number of N-terminal glycines from 1 to 3 and simultaneously getting rid of the proline. A comparison of the labelling of the two apoE constructs was carried out and analysed using SDS-PAGE stained for total protein and fluorescently scanned Fig 6.9 a and b respectively.

Lanes 3-6 and 7-10 on both gels show time points in the labelling of TEV cleaved apoE and 3C cleaved apoE respectively. The results for 3C cleaved apoE are analogous to that shown in Fig 6.6, namely that labelling increases over time for the first 3 h, where an equilibrium is reached leaving at least ca. 50 % unlabelled protein. The situation for the TEV cleaved apoE is very different. In this case the labelling seems to occur very fast with quantitative labelling occurring within ca. 1 h. After this point the labelling efficiency actually decreases, evidenced by the reappearance of the unlabelled band and the decrease in fluorescent intensity.

This decrease in labelling efficiency is likely caused by a build-up of the glycine dipeptide, which causes the reverse reaction to become more favourable. However if the reaction is stopped after 1 h and purified, labelling efficiencies >90 % can be attained. This represents a major improvement upon the previous labelling, which was at most ∼30 %. This suggests that either increasing the number of glycines and/or increasing the conformational flexibility (by the removal of proline) of the N-terminus leads to much better labelling efficiency for apoE. Interestingly, while much of the literature surrounding the use of sortase to functionalise proteins does point out that the N-terminal glycine should not be too near highly structured parts of the protein, which is usually solved by having some -Gly-Ser- repeats as a short

linker, no reference to the presence of proline being detrimental could be found. This is somewhat surprising given the wide use of 3C protease in protein purification as an efficient, and highly specific protease for the removal of affinity/fusion tags, commonly employed in recombinant protein production.

Making the dipeptide side product a worse nucleophile

While the side product of a successfully labelled protein is itself an efficient nucleophile, the labelling will always be plagued by the problems of the reverse reaction. In order to overcome this large excesses of probe are added to drive the equilibrium to the labelled product. But as seen in the preceding section, even when the efficiency of the forward reaction is improved the reverse reaction can still prove problematic. Furthermore, a large amount of probe (which is either expensive or time consuming to make) is wasted during each reaction, before you even consider how to successfully purify your labelled protein swamped beneath a vast excess of probe.

The solution to this problem is to make the reverse reaction less efficient, that is to make the product of the labelling reaction a worse nucleophile. In the literature the use of depsipeptides have been reported for this use. A depsipeptide is a peptide where instead of having an amide bond linking two amino acids, the corresponding ester is used instead. If this ester bond is placed in the correct position in the probe molecule the cleavage of the probe and release of the Gly-Gly dipeptide will now have an HO- at its 'N-terminus' instead of the amine. This is illustrated in the scheme in Fig. 6.10.

Compared with an amine, an hydroxyl is a much weaker nucleophile and should not be able to participate in the reverse reaction to as great an extent. To test this a depsipeptide, analogous to the Atto488-LPETGG probe but with an ester between the threonine and glycine (Atto488-LPET(C−O)GG) was purchased. A comparison labelling reaction between the depsipeptide and normal peptide probes is shown in Fig. 6.11.

Surprisingly Fig. 6.11 shows that the labelling with the depsipeptide is slightly slower compared to the peptide probe, and disappointingly the labelling efficiency does not seen to be any better. It should be pointed out that the ratio of fluorescent peptide to enzyme was 10:1, which is the same ratio that was used in Fig. 6.9. This ratio was preserved because if there was more enzyme than fluorescent peptide, the reverse reaction would be favoured. As a result of keeping the ratio the same, there is 10 times less enzyme in this reaction and so it was expected to require a longer

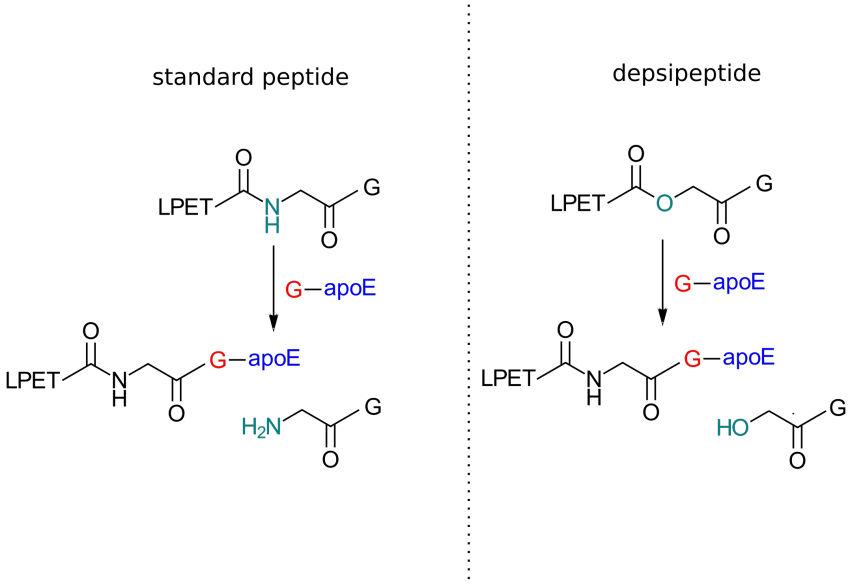
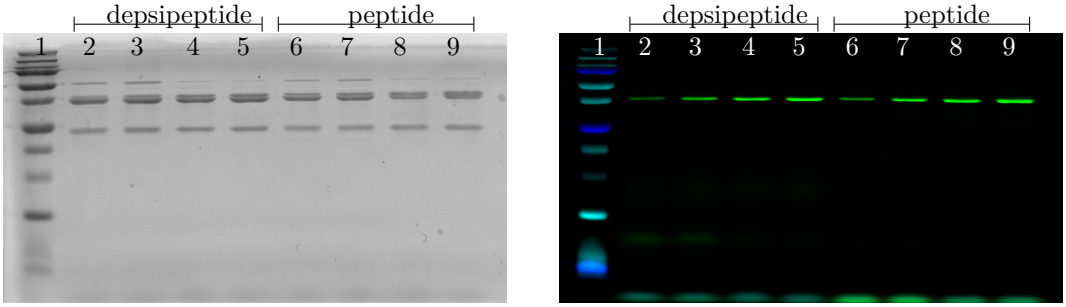


Figure 6.10 – Depsipeptide substrate. Sortase enzyme labelling with standard peptide and depsipeptide.



(a) SDS-PAGE stained for protein

(b) SDS-PAGE fluorescently scanned

Figure 6.11 – Making the side product a worse nucleophile. (a) & (b) display the same gel stained for total protein or fluorescently scanned. Lane 1 - molecular weight marker, lanes 2-5 - labelling reaction using Atto488-depsipeptide at time points 0.5, 1, 2.25 & 4 h, lanes 6-9 - labelling reaction using Atto488-peptide at time points 0.5, 1, 2.25 & 4 h. Labelling conditions, final concentrations: tev-apoE4 (50 µM), SrtA (10 µM), Atto488-depsi/peptide (100 µM)

incubation period.

In general, depsipeptides are not as stable as standard peptides as the ester will hydrolyse to yield a carboxylic acid. This would lower the concentration of depsipeptide that can be utilised by the sortase enzyme and might go some way as to why a higher labelling efficiency wasn't achieved. It may be that by increasing the depsipeptide concentration to 3 or 5 times the protein concentration (which is

still vastly lower than the 20 times used in Fig. 6.9) may yield a higher degree of labelling.

6.6 Summary

In this chapter, the expression, labelling and purification of apolipoprotein E was discussed. The method of expression employed is based off a previously described protocol with only minor adaptions.[160] Various fluorescent methods by which apolipoprotein E has already been studied were highlighted. Alternative methods to introduce a fluorescent label into apolipoprotein E were put forward with eventually settling on enzymatic labelling of the N-terminus by Sortase A. The N-terminus was chosen as we predict it would have minimal affect on the protein's structure or function. This is evidenced by many of the partial and (highly mutated) full length structures currently available for apolipoprotein E, showing that the N-terminus is on the surface of the protein in a region that lacks defined structure.

Many methods of purifying the labelled apoE were trialled, with most showing unsatisfactory results. After much method development the most effective purification for the small volume labelling reactions was to perform the purification under denaturing conditions, first using a home made His spin column to remove the sortase A enzyme followed by many buffer exchanges using a centrifugal concentrator.

The percentage labelling efficiency achieved after purification was initially 15-30 %. After optimising the enzymatic reaction, by making the apoE a better nucleophile, labelling efficiencies of >90 % were attainable. Further attempts at optimising the enzymatic reaction, by making the side products worse nucleophiles (i.e. unable to take part in the reverse reaction), did not show any benefit.

Overall, a new method for the fluorescent labelling of apoE on its N-terminus has been presented. While this protocol likely introduces some extra steps over previously reported methods for introducing fluorescent labels to apoE, it is potentially a more faithful representation of the native protein as it doesn't require mutagenesis of key residues, and adds the label to a region of the protein not expected to be involved in the formation of secondary structure.

Chapter 7

Apolipoprotein E Lipid Interactions

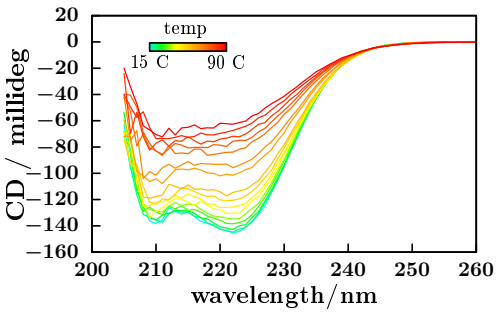
Having obtained a source of recombinant apoE3 and E4, and having optimised a methodology for introducing a label on the N-terminus, (as described in Chapter.6) this chapter puts these proteins to use. This chapter explores the structure of apoE, its interaction with lipid membranes, and potential roles in lipid peroxidation, trying to identify isoform specific differences between apoE3 and E4 that may hint towards the role of apoE in Alzheimer's disease.

7.1 Circular dichroism

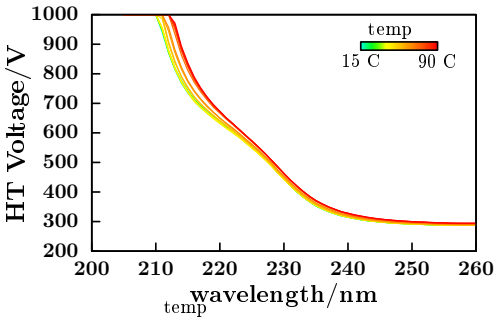
To verify that apoE can be refolded following the purification by denaturation detailed in Chapter 6 circular dichroism (CD) was performed. Fig. 7.1 shows the CD spectra for apolipoprotein E (apoE) containing two distinct negative peaks at 210 nm and 220 nm. Negative peaks at this wavelength are characteristic of a protein containing α helical secondary structure. Apolipoprotein E contains many α helicies in its structure and so the protein appears to have refolded correctly, the spectral shape and intensity also matches a reported CD spectra for delipidated apoE3 purrified from plasma.[170] The spectra below 205 nm has been truncated as the signal to noise was not acceptable. This poor signal to noise can be explained by looking at Fig. 7.1(b) which shows that the HT voltage has reached it maximum value, i.e. not enough photons are hitting the detector as the sample is too highly absorbing at these lower wavelengths. This suggests that 30 µM is too high a concentration to acquire CD spectra in the far UV region.

Fig. 7.1(a) also shows how the CD spectra of apoE changes as the temperature is increased, indicated by the colour scale bar. As the temperature is increased the protein is thermally denatured, resulting in a loss of secondary structure and a

decrease in the intensity of the CD peaks.



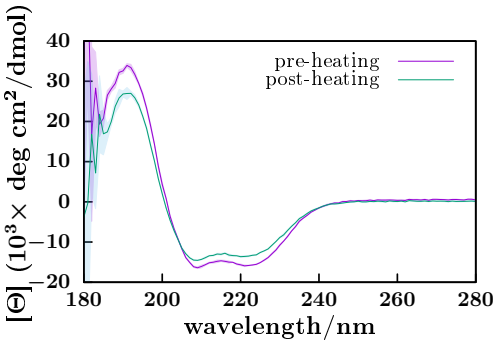
(a) CD thermal denaturing spectra



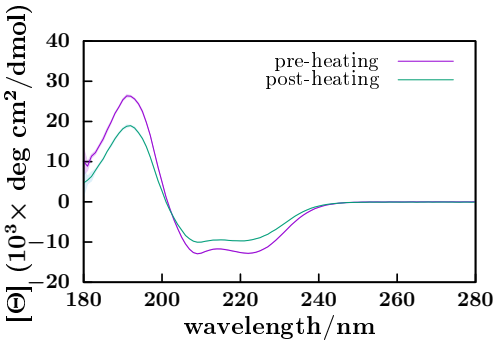
(b) High tension voltage (HV)

Figure 7.1 – Circular dichroism of apoE. 30 µM (∼ 1 mg mL^{-1}) apoE in 1 mm cuvette. Scanned in 5 °C steps between 15 °C and 90 °C, indicated by the colour bar. 0.5 s integration time per point.

Fig. 7.2 shows the CD spectra for apoE3 and E4, at a concentration amenable to far UV CD. Each plot shows the spectra for the respective protein both prior to and following thermal denaturation and subsequent cooling to the original temperature. The fact that a CD signal is present after thermal denaturation of apoE suggests that the protein spontaneously refolds back into its original secondary structure. This provides further evidence that chemical denaturation is also a reversible process that will produce a correctly folded protein following removal of the denaturant by dialysis.



(a) apoE3



(b) apoE4

Figure 7.2 – apoE refolds following thermal denaturation and cooling. 1 µM apoE in 2 mm cuvette scanned at 15 °C and then following heating to 90 °C and subsequent cooling to 15 °C. Spectra shown are the mean of 5 repeat measurements, shaded region is the standard deviation. Each point had an integration time of 1 s.

Although the pre- and post-heating CD spectra show a similar shape, the intensity of the peaks has been reduced following thermal denaturation. This suggests that the concentration after denaturation is lower than before. This could be due to a small proportion of the protein having become irreversibly aggregated during the cooling process. An equally likely explanation could be that the full refolding of the protein takes longer than the time it takes to rapidly cool the sample from 90 °C to 15 °C, or that the temperature of the solution had not fully reached 15 °C. The temperature reported is that of the cuvette holder and not of the solution itself (although the temperature is held for 0.5 min at each temperature to try and ensure that the solution temperature has reached equilibrium).

Comparing the CD spectra of apoE3 and E4, it can be seen that E3 displays a stronger signal. The signal is calculated as the molar elipticity of the repeating peptide bond, and as the peptides have the same number of amino acids one would expect the CD spectra to have the same intensity.

Fig. 7.3(a) shows the mean residue molar ellipticity for apoE3 and E4 at 222 nm as a function of temperature. This wavelength is typically used to monitor thermal denaturation of proteins because it represents the unfolding of α-helices and typically gives better signal to noise than lower wavelengths. Both apoE3 and E4 show similar melting curves, with a highly sloped transition between the folded and unfolded states. This suggests a high degree of cooperativity in the melting of apoE which is unsurprising as at the concentrations used the protein is expected to exist as a tetramer. Approximating the unfolding with a Hill equation reveals the midpoint of the melting transition to be 64.5(4) °C and 56.8(2) °C for apoE3 and E4 respectively. This matches the reported trend in thermal stability for the N-terminal domain of apoE (residues 1-191), with the N-terminal domain of apoE3 being more thermally stable than the N-terminal of apoE4.[171]

Fig. 7.3(b) shows that diluting the sample by a factor of 10 does not change the melting temperature, (64.2(4) °C cf. 64.5(7) °C). This suggests that even at 1 µM, apoE3 still exists predominantly as tetramers.

7.2 FCS of apoE with lipids

To study the interaction of apoE with lipids one can use fluorescence correlation spectroscopy (FCS) in a similar way as was used to study the binding of Aβ to lipids detailed in Chapter 5. It is known that a solution of apoE will be in equilibrium between monomers, dimers and tetramers and that at µM concentrations the equilib-

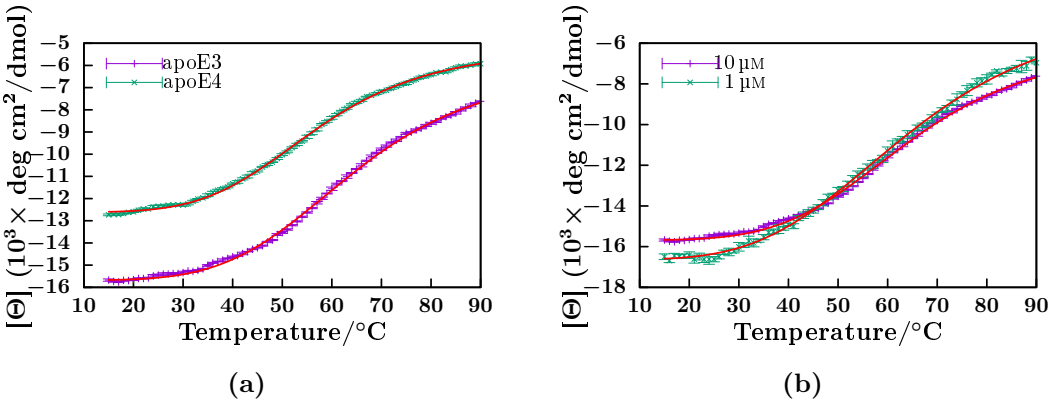


Figure 7.3 – Thermal denaturation of apoE. Mean residue molar ellipticity at 222 nm as a function of temperature of; (a) 10 µM apoE3 or E4 in a 1 mm cuvette, (b) 10 µM and 1 µM in a 1 mm and 2 mm cuvette respectively. Temperature was ramped from 15 °C to 90 °C in 1 °C steps, with 30 s of settling time at each temperature before measurement was taken. Points shown are the mean and standard deviation of five repeat measurements, each with an integration time of 1 s.

rium will favour tetramers.[162] If we rapidly dilute a sample of fluorescently labelled apoE from µM concentrations to nM concentrations required for FCS, we can follow the dissociation process. This is shown in Fig. 7.4. The plot shows that upon dilution the diffusion time decreases, i.e. the particles are now diffusing more quickly. This is likely due to the dissociation from tetramers to monomers (which dominate at nM concentrations. The decrease in the diffusion time can be approximated to a single exponential with an observed rate of $0.05(2)\,\mathrm{min}^{-1}$.

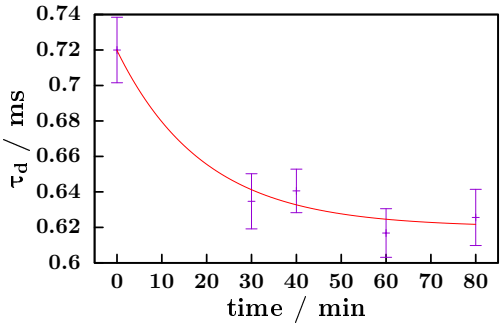


Figure 7.4 – apoE4 dissociation upon dilution. FCS diffusion time of atto488-apoE4 which was rapidly diluted from µM to nM concentrations. Tris NaCl with $0.3\,\mathrm{mg\,mL}^{-1}$ BSA. Laser power $\sim 80\,\mu\mathrm{W}$ data acquired over 120 s acquisition.

The initial model lipid system used for apoE binding was GM1 micelles. Fig. 7.5 shows how the diffusion time of labelled atto488-apoE4 changes upon mixing with

GM1 micelles (GM1 micelles were added at time t = 0 min). Initially the labelled apoE was diluted to nM concentrations for the FCS experiment and left for ∼ 30 min (as determined from Fig. 7.4) so that the sample could dissociate to monomers. The initial diffusion time of the labelled apoE was measured showing a diffusion time typical of an apoE monomer. At t=0 min GM1 micelles were added and it can be seen that the diffusion time becomes larger, indicating that the apoE is associated with the GM1 micelles. The diffusion time for the apoE:GM1 complex measured here is larger than what was measured for a labelled GM1 micelle in Chapter 5 (apoE:GM1 τ_d 0.93(8) ms cf. τ_d 0.54(2) ms for labelled GM1 micelle). Interestingly the reaction seems to be rather rapid, with the apoE becoming bound to the GM1 micelles before the first FCS curve could be acquired.

Using the dye AlexaFlour488 as a standard with a reported hydrodynamic radius R_H 5.6 Å we can calibrate our system. The AlexaFlour488 dye has a diffusion time of 0.128(8) ms which allows us to calculate the hydrodynamic radius of monomeric apoE as R_H 28 Å and in the presence of GM1 micelles as R_H 41 Å.

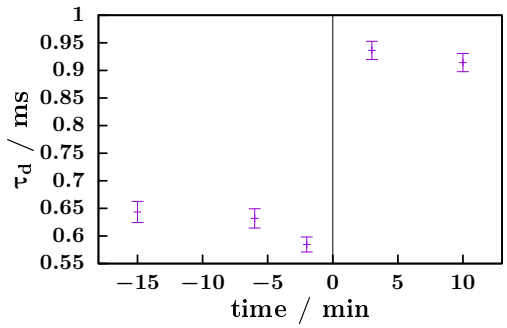


Figure 7.5 – apoE binds to GM1 micelles. FCS diffusion time of atto488-apoE4 which is then mixed with GM1 (final concentration 100 µM lipid). Buffer Tris NaCl with 0.3 mg mL^{-1} BSA. Laser power ∼ 80 µW data acquired over 120 s acquisition.

It has been reported that apoE can interact with a multilamellar lipid suspension of DMPC vesicles, and can 'solubilise' the lipid suspension by forming lipoprotein particles. This 'solubilisation' is the basis of the turbidity measurements that are used to characterise the function of many different kinds of apolipoproteins. These turbidity measurements are carried out as follows- A concentrated suspension of DMPC lipid vesicles, of uncontrolled size and lamellarity is prepared. Such a solution appears turbid, scattering light. apoE is added to the lipid suspension and as it converts the suspension to lipoprotein particles the turbidity of the solution is reduced. This can be followed with UV-Vis.

To try and improve upon this method, FCS could potentially be employed. As FCS uses fluorescence and not scattered light, the solution no longer needs to be turbid and so the concentrations of both lipid and protein can be reduced. The size and lamellarity of the vesicles can also be more finely controlled so that one can have a better idea of the species present undergoing reaction.

Fig. 7.6(a) shows how the FCS trace of a fluorescently labelled 100 nm DMPC small unilamellar vesicle (SUV) changes upon addition of (unlabelled) apoE4. It can be clearly seen that G0 decreases over the course of the reaction, indicating that there is an increase in the number of fluorescent particles in solution. The diffusion time also decreases, although it is harder to see by eye because of the concurrent decrease in G0, suggesting that the particles are diffusing faster.

For the FCS trace at 0 min, the curve can be fit well to the standard single diffusing species FCS equation, with the contribution from the triplet relaxation process being able to be ignored. Ignoring the triplet contribution is possible as the diffusion of the 100 nm SUVs is sufficiently slow as to be easily separated from the faster triplet lifetime by limiting the fitting to times >1 µs. In contrast to the trace at 0 min, the FCS trace at 85 min did not give a satisfactory fitting to the standard single species diffusion. Instead an equation allowing for two diffusing species was required for adequate fitting. In order to fit the dataset a global fitting approach was employed using an equation for two species while sharing the diffusion time of the faster of the two species across all traces. The fitted lines are shown in Fig. 7.6(a) as red lines. The diffusion time for the slow species was in the ms regime, as expected for a 100 nm SUV. The diffusion time of the fast species that was shared between all traces was 74(5) µs. This diffusion time is unusually fast, given that the diffusion time for free AlexaFlour488 dye is 128(8) µs, but is also at least an order of magnitude slower than what would be expected for triplet lifetime.

Fig. 7.6(b) shows how the total G0 (sum of the contributions from the fast and slow diffusing species) varies over time after apoE4 is added to DMPC SUVs. The data can be approximated with a single exponential yielding an observed rate of 0.04(1) min^{-1}. This observed rate in the increase of the number of fluorescent particles is within error of the rate measured for the dissociation of labelled apoE tetramers to monomers (Fig. 7.4), suggesting that the limiting step in the interaction of apoE with DMPC SUVs is dissociation. This observation matches with prior literature.[172]

Fig. 7.6(c) shows how the fractions of the fast and slow species' contributions evolve over time. At the beginning of the reaction the system is almost entirely slow

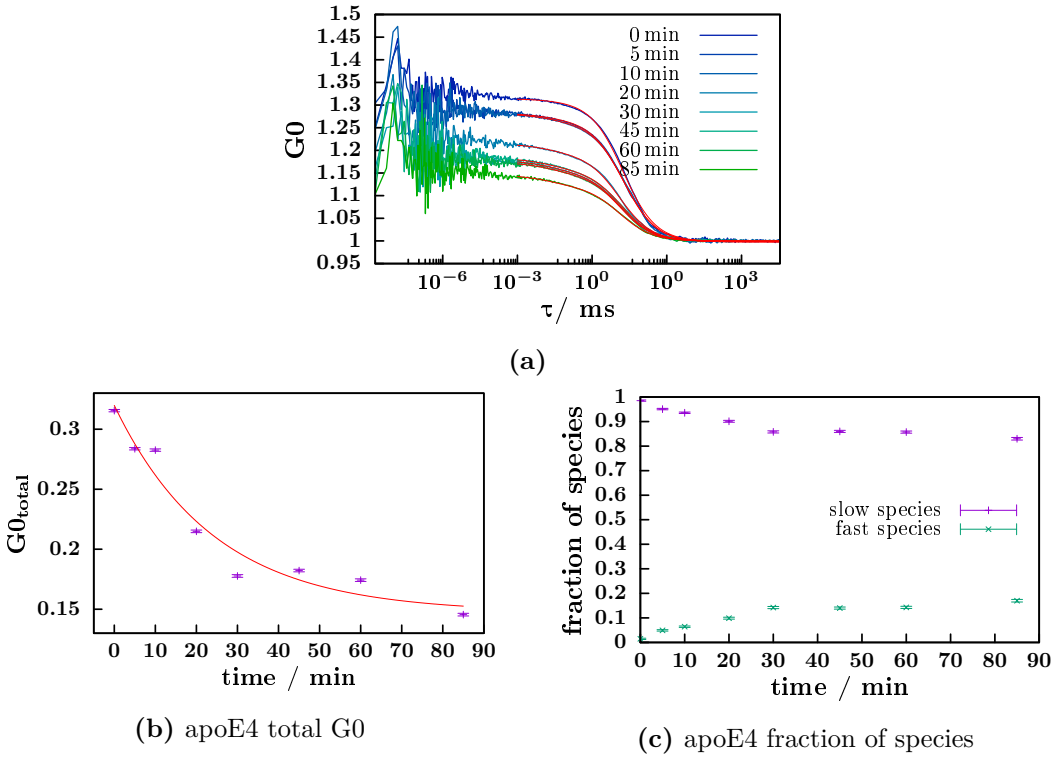


Figure 7.6 – apoE4 binds to and disrupts labelled DMPC SUVs. FCS of 100 nm DMPC SUVs labelled with 0.05 mol% BODIPY-GM1 (total lipid concentration 295 µM) which is then mixed with apoE4 (1 µM). (a) FCS traces recorded over time following mixing, shown fitted to a two species FCS diffusion equation. (b) Decrease of total G0 from fitting of (a) against time. (c) relative fraction of the two species from the fitting of (a) against time. Experiment performed in HEPES/NaCl, laser power ~150 µW data acquired over 120 s acquisition.

diffusing, (which explains why a single diffusing species equation can describe the FCS trace at this time point). Over time the contribution from the fast diffusing species increases until it accounts for approximately 20 % of the total G0. This could represent the conversion of the slowly diffusing DMPC SUVs to a much faster diffusing species upon reaction with apoE.

Taken together, analysis by FCS shows that when apoE is added to fluorescently labelled 100 nm DMPC SUVs it increases the number of fluorescent particles, and that the fluorescent particles now diffuse more quickly (i.e. they are smaller). This could represent apoE binding to the lipid SUV and disrupting the vesicle by forming a smaller lipoprotein particle.

Fig. 7.7 shows the same FCS experiment discussed above but with apoE3. In general there is a similar trend as with apoE4, the value of G0 decreases as does the

diffusion time. However there is a higher variability in the FCS measurements and the trend is not as clear as apoE4.

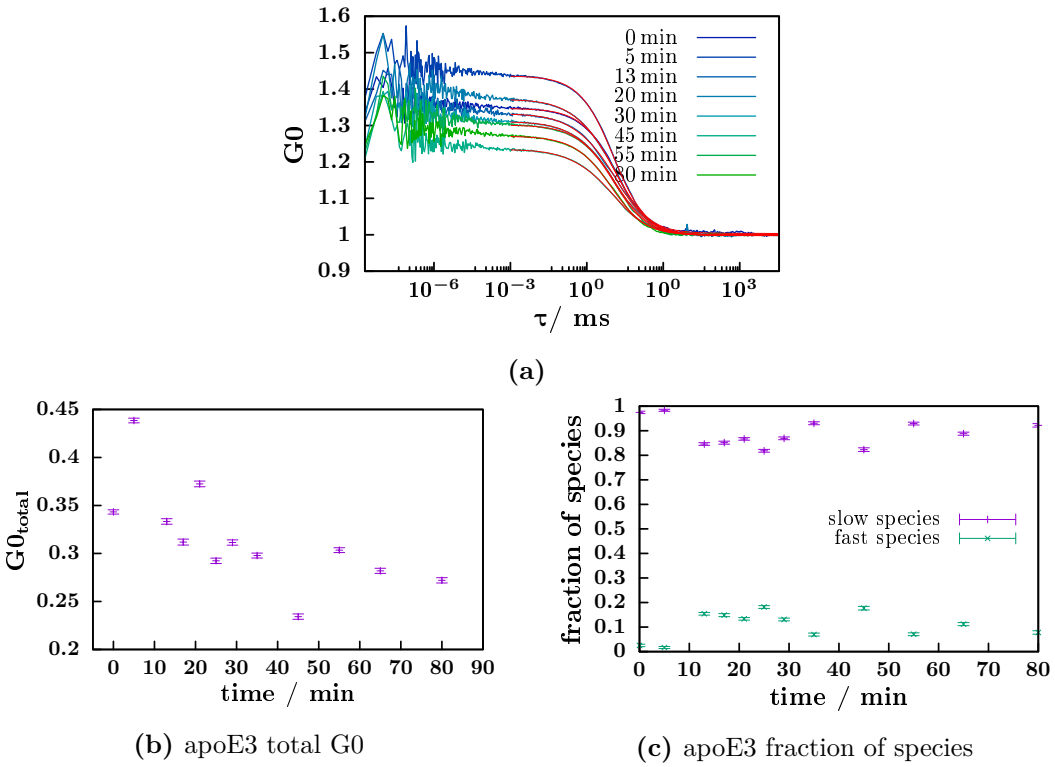


Figure 7.7 – apoE3 binds to DMPC SUVs. FCS of 100 nm DMPC SUVs labelled with 0.05 mol% BODIPY-GM1 (total lipid concentration 295 µM) which is then mixed with apoE3 (1 µM). (a) FCS traces recorded over time following mixing, shown fitted to a two species FCS diffusion equation. (b) Decrease of total G0 from fitting of (a) against time. (c) relative fraction of the two species from the fitting of (a) against time. Experiment performed in HEPES/NaCl, laser power ∼150 µW data acquired over 120 s acquisition.

7.3 Lipid peroxidation of apoE-lipid particles

In the preceding section it was shown that apolipoprotein E can bind to lipids and evidence was presented showing that apoE can disrupt SUVs potentially forming lipoprotein particles. While there is plenty of evidence trying to find out where apoE exerts its influence on Alzheimer's disease, such as: binding Aβ [142] and aiding clearance, [173], not directly binding to Aβ but still aiding clearance, [148], increasing Aβ production though interactions with an apoE receptor, [174] binding to Aβ and slowing its oligomerisation, [147,175] or being a chaperone for Aβ metal induced aggregation, [176]

many reviews on apoE neurobiology spend little time considering the potential for apolipoprotein E to play a role in oxidative damage.

Some research has however been pointed in this direction, looking at whether apoE could play a role in lipid peroxidation. It has been noted that apoE deficient mice show increased lipid peroxidation,[177] and that apoE is able to protect a B12 cell line from hydrogen peroxide damage.[178] This latter cell line study showed isoform specific effects, with E3 being more protective than E4. They also showed that apoE can bind metal ions, leading them to postulate that metal binding is responsible for the antioxidant effect of apoE. Some have challenged a metal binding explanation, instead proposing that it is the radical scavenging ability of the region of apoE responsible for receptor binding (residues 141-155).[179] Other research looking into the mechanism of how apolipoprotein E prevents lipid peroxidation has shown that apoE can be modified by 4-hydroxynonenal (a lipid peroxidation product), and that apoE3 can bind more 4-hydroxynonenal than apoE4.[180] While the evidence for a link between apolipoprotein E and lipid peroxidation exists, the mechanism of this interaction is still not clear.

To probe the possible effect of apoE on lipid peroxidation, experiments similar to what are described in Chapter 5 were carried out in the presence of apoE. Fig. 7.8 shows how the lipid peroxidation as detected by the C_{11}-BODIPY$^{581/591}$ probe is reduced when apoE is present. In these experiments apoE3 or E4 was incubated with 100 nm DMPC SUVs for 30 min (as determined from Fig. 7.6) before oxidation was initiated. In Fig. 7.8 oxidation was initiated by $H_2O_2/CuCl_2$ and not AβCu and ascorbate that was used throughout Chapter 5. This was because experiments from Chapter 5 did not provide conclusive evidence that Aβ could bind to SUVs and initiate lipid peroxidation.

The lipid peroxidation in the presence of apoE appears to increase linearly and is shown in Fig. 7.8 with a line of best fit. The lipid peroxidation caused by $H_2O_2/CuCl_2$ in the absence of apoE is better fit with an exponential function.

Although Fig. 7.8 shows clear evidence that addition of apoE decreases the rate of lipid peroxidation, it is unclear how relevant lipid peroxidation caused by $H_2O_2/CuCl_2$ is to Alzheimer's disease. Fig. 7.9 shows how apoE effects lipid peroxidation initiated by AβCu and ascorbate. In order to try and circumvent some of the problems encountered in Chapter 5 with Aβ being able to bind to SUVs and initiate peroxidation, in Fig. 7.9 the Aβ40 was directly incorporated into the lipid film. Upon hydration and formation of vesicles the Aβ should remain within the lipid membrane. After formation of SUVs, Cu^{2+} and ascorbate can be added to initiate

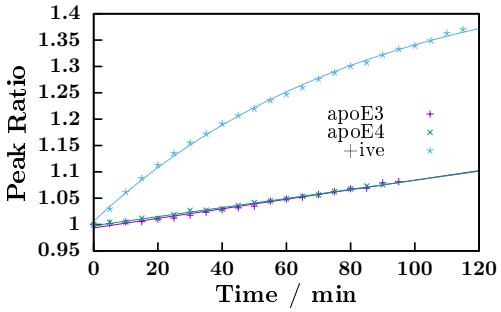


Figure 7.8 – Lipid peroxidation of DMPC:apoE particles. DMPC 100 nm SUVs containing 0.1 mol% C_{11}-BODIPY$^{581/591}$ (total lipid concentration 0.8 mM) were incubated with 2 µM apoE for 30 min before oxidation being initiated by addition of 2 mM H_2O_2 and 2 µM $CuCl_2$. The lipid peroxidation in the absence of apoE is also shown (+ive). Plotted on the y-axis is the ratio of the areas of the two peaks from the C_{11}-BODIPY$^{581/591}$ dye.

redox cycling and lipid peroxidation. It is assumed that the Aβ with orientate itself so that the polar N-terminus will be exposed out of the lipid bilayer, and that Aβ molecules will be equally distributed on either side of the lipid bilayer (as such the Cu^{2+} concentration is reduced by half).

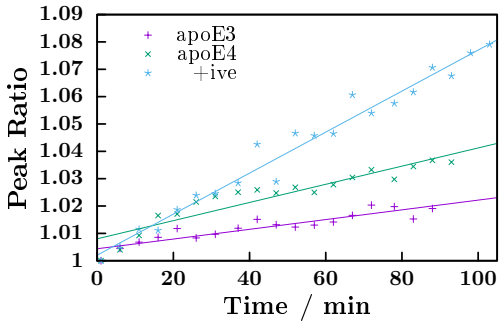


Figure 7.9 – Lipid peroxidation of DMPC:apoE particles by AβCu. A lipid film containing DMPC, Aβ40 (0.1 mol%) and C_{11}-BODIPY$^{581/591}$ probe (0.1 mol%) was hydrated, resuspended and extruded to form 100 nm SUVs (total lipid concentration 1 mM). 2 µM apoE was added and incubated for 30 min before oxidation was initiated by addition of 0.5 µM $CuCl_2$ and 100 µM ascprbate. The peroxidation of SUVs in the absence of apoE is also shown (+ive). Plotted on the y-axis is the ratio of the areas of the two peaks from the C_{11}-BODIPY$^{581/591}$ dye.

Fig. 7.9 shows that when peroxidation is initiated by AβCu and ascorbate, addition of apoE also reduces the rate of peroxidation observed. Interestingly the peroxidation in the absence of apoE increases linearly, as opposed to the exponential increase observed in Fig. 7.8. By fitting the data shown in Fig. 7.9 with a straight line, it can

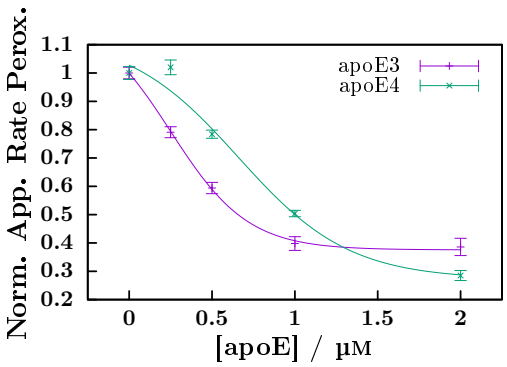


Figure 7.10 – apoE reduces apparent rate of lipid peroxidation in an isoform dependant manner. 1 mM DMPC 100 nm SUVs containing 0.1 mol% C_{11}-BODIPY$^{581/591}$ probe were incubated with various concentrations of apoE3 or E4 for 30 min. Peroxidation was initiated by adding $CuCl_2$ (1 µM) and H_2O_2 (1 mM) and the change in C_{11}-BODIPY$^{581/591}$ fluorescence recorded in a plate reader. Shown plotted is the apparent rate of peroxidation against apoE concentration.

be calculated that apoE3 and E4 reduce the rate of lipid peroxidation by 76(3) % and 56(5) % respectively. However, it should be noted that the total amount of lipid peroxidation observed, even in the absence of apoE, was small.

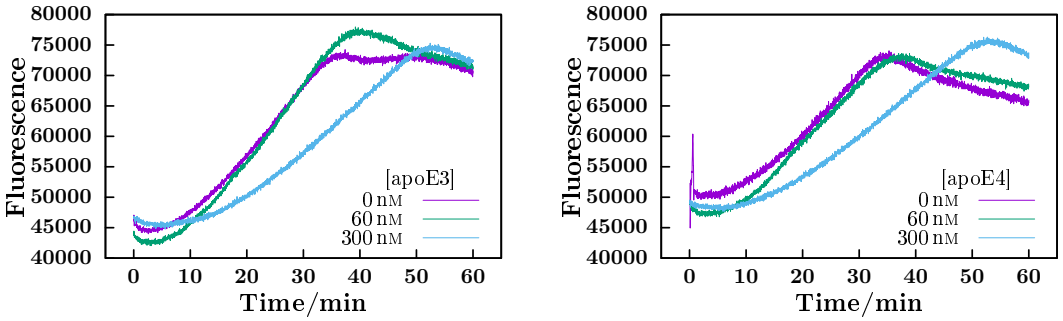
It is interesting to observe that apoE3 reduces the peroxidation to a greater extent than apoE4. This could suggest that the protection that apoE offers against lipid peroxidation is isoform specific, and correlates with apoE4 being a less good antioxidation, and carrying a greater risk of developing AD. To explore this further the lipid peroxidation was measured for different concentrations of apoE added, (Fig. 7.10). Because doing so many measurements in a fluorometer one after the other would be laborious and take many hours of data collection, the methodology was transferred to be able to be carried out in a 98 well plate reader. While the signal to noise of the plate reader is inferior to using a fluorimeter, being able to run different concentrations in parallel is a major advantage.

Fig. 7.10 shows how the rate of lipid peroxidation changes for different concentrations of apoE3 or E4 added. It can be seen that the rate of peroxidation decreases as more apoE is added. Fitting the data with a sigmoid allows the extraction of the midpoints of the curves as being 0.25(6) µM and 0.7(2) µM for apoE3 and E4 respectively. This suggests that in order to get a similar reduction in lipid peroxidation, more apoE4 is needed than apoE3. This difference in concentration required is further evidence of an isoform specific effect.

While the results presented so far are supportive of apoE having a role in

preventing lipid peroxidation, it is not clear if this antioxidative effect is a result of apoE remodelling the lipids into lipoprotein particles. Even at the highest concentrations of apoE used (2 µM) it is not certain that this concentration is high enough to convert all of the SUVs into lipoprotein particles. It is therefore likely that the lipid peroxidation observed is a mixture of peroxidation occurring in SUVs and lipoprotein particles.

It is also possible that apoE is simply acting as an antioxidant and is being preferentially oxidised rather than the C_{11}-BODIPY$^{581/591}$ probe. To try and shed light on this mechanism of antioxidant effect, oxidation of apoE was carried out without any lipid present. 3-coumarin-carboxylic acid (3CCA), (which is discussed in Chapter 5) was used to detect hydroxyl radicals in solution, in the presence or absence of apoE3 and E4, (Fig. 7.11).



(a) apoE3 **(b)** apoE4

Figure 7.11 – apoE reduces solution hydroxyl radical production. Detection of hydroxyl radical in solution by 3-CCA. Oxidation of 3-CCA (100 µM) in the presence of apoE3 or E4 (concentrations shown in the figure legends), initiated by $CuCl_2$ (1 µM) and ascorbate (100 µM). Experiment performed in HEPES/NaCl, λ_{Ex} 395/5 nm, λ_{Em} 450/5 nm with an integration time of 1 s.

From Fig. 7.11 it can be seen that addition of 300 nM apoE3 or E4 reduces the rate of solution OH$^{\cdot}$ formation. This reduction in rate does not seem to occur when only 60 nM apoE is present. All of the kinetic traces show some anomalous behaviour, such as an initial dip before increasing fluorescence, and an addition decrease in the fluorescence at longer timescales. This decrease in fluorescence could be due to effects such as photobleaching, or (more probably) further oxidation of the probe to a new non-fluorescent state.

Regardless of these anomalies, it is clear that apoE reduces the rate of solution OH$^{\cdot}$ formation in the absence of any lipid present. This suggests that the antioxidant properties of apoE are not solely due to it remodelling lipid SUVs into lipoprotein

particles, and that it is more likely that apoE is simply being preferentially oxidised.

7.4 Summary

In this chapter apolipoprotein E3 and E4 were studied. Circular dichroism showed that following the purification detailed in Chapter 6 the protein was in a folded state. ApoE was shown to spontaneously refold following thermal denaturation, which might not be surprising saying this protein is expected to bridge the gap between aqueous and hydrophobic environments. The melting temperature of full length apoE3 and E4, as determined by CD, was obtained. ApoE3 was shown to be more thermally stable than apoE4, which matches previously reported stabilities for the N-terminal domains of apoE3 and E4.[171]

By using fluorescence correlation spectroscopy, apoE was shown to be able to bind to model lipid membranes, and disrupt lipid SUVs potentially forming lipoprotein particles. The timescales for this process were noted to be similar to the timescales of apoE dissociation.

The influence of apoE on lipid peroxidation was explored, making use of similar experiments that were used in Chapter 5. Apolipoprotein E was shown to reduce the rate of lipid peroxidation, as determined by the fluorescent C_{11}-BODIPY$^{581/591}$ lipid peroxidation sensitive probe. The ability of apoE to protect against lipid peroxidation was shown to be isoform dependant, with apoE3 being more protective than apoE4. Apolipoprotein E was also shown to reduce the rate of formation of hydroxyl radicals in solution, as determined by the 3-coumarin-carboxylic acid probe. This hints at the mechanism of apoE, suggesting that its antioxidant effect is as a radical scavenger, and not specifically limited to preventing lipid peroxidation.

Chapter 8

Conclusions & Further Work

The main aim of this thesis was to study, from a kinetic point of view, molecular interactions that are potentially of relevance in Alzheimer's disease. While much may be known about the thermodynamics of such molecular interactions, their kinetics are less well described. Only when we know both the thermodynamics and kinetics can we begin to understand the system, allowing us to make inferences on the roles such interactions may play in disease.

Amyloid-β, Cu and the metals hypothesis

This thesis began by focusing on Amyloid-β and the so called 'metals hypothesis'. Building upon the thorough kinetic description of the interaction between Aβ and Cu by Branch (2015),[86] this thesis extended the research to study the kinetics of Cu with Aβ containing Familial Alzheimer's disease (FAD) mutations. The FAD substitution mutations studied (H6R and D7N), occurred within the Cu binding region of Aβ. As such we hypothesised that these mutations would show altered copper interactions, and so would allow us to draw conclusions about the role of Cu in AD based on these 'disease prone' FAD mutations. Surprisingly, neither mutation had much impact on the Aβ Cu^{2+} association rate, while they had differing effects on the dissociation rate. Compared with wt-Aβ, H6R showed a lower affinity for Cu^{2+} while D7N had a higher affinity. By studying the AβCu^{2+}Aβ ternary complex formation, as an indication of the Aβ dimerisation rate, we showed that both mutants had an increased rate of dimerisation compared with the wild type. It is interesting to note that this increased rate of ternary complex formation better correlates with risk of developing AD, compared to the equilibrium dissociation constants.

One of the main elements of the metals hypothesis in Alzheimer's disease is the proposal that Aβ bound to redox active metals can undergo redox cycling, causing

the oxidative damage that is observed in AD brains. While the ability of the AβCu complex to produce reactive oxygen species (ROS) has been demonstrated in vitro, a kinetic understanding of the timescales on which this process may occur, has yet to be described.

In an attempt to address this issue, we directly probed the oxidation state of the Cu ion in the AβCu complex. We showed that reduction of $A\beta Cu^{2+}$ primarily goes via the Component I conformation, and not via Component II. This increased reactivity for Component I mirrors others' observations that metal assisted dimerisation is also more likely to go via Component I rather than Component II. If increased reactivity of the Component I $A\beta Cu^{2+}$ complex is a common feature of different aspects of Aβ biology, altering the ratio of Components I & II to lie more on the 'inert' Component II side might be an interesting therapeutic approach.

Our kinetic data for the reduction of $A\beta Cu^{2+}$ was able to be fit to a conformational selection model. This is in agreement with other research which proposed the existence of a 'catalytic in-between-state' which is able to undergo redox cycling, and is distinct from the coordination of the $A\beta Cu^{2+}$ Component I & II coordinations. The reduction kinetics of Aβ containing histidine substitutions suggests that this in-between-state likely has His13 as a coordinating amino acid, and not His6. Taking the rate constants obtained with the concentrations of ascorbate present in the cell, it appears that the rate liming step for reduction is the preorganisation step and not the binding of ascorbate.

In contrast to the relatively fast reduction the oxidation of $A\beta Cu^{+}$ is much slower. While the reduction would occur on the 10 ms timescale, the oxidation will take orders of magnitude longer. While it should be noted that the reduction alone is capable of generating damaging radicals, generation of ROS via redox cycling of AβCu would likely be a more infrequent event.

One caveat of the work on Aβ in this thesis, is that it describes the kinetics of monomeric Aβ. For example, the redox cycling of AβCu might be very different in an Aβ oligomer or fibril compared with a monomer. One very recent manuscript, that indirectly measures redox cycling, found that Aβ monomers and fibrils were less prone to redox cycling than Aβ 'oligomers' (which the manuscript noted as being ∼10-12 mers).[181] Regardless, the study of the AβCu monomer is still of importance. For example redox cycling of the AβCu monomer could lead to damage of the Aβ itself, including potential formation of dityrosine cross linked Aβ dimers. It has been postulated that such cross linked Aβ dimers could form the initial templates for Aβ oligomerisation.

If such a cross linked Aβ dimer could be synthesised and purified, it would indeed

be interesting to study the kinetics of its interactions with Cu and redox cycling. Such an avenue would likely yield interesting insights into the comparisons of monomeric Aβ and (a well-defined and stable model for) Aβ small oligomers.

Lipid peroxidation

Using a fluorescent lipid peroxidation probe we showed that, in GM1 micelles, AβCu redox cycling is much more efficient at causing lipid peroxidation than free Cu in solution. This observation is made all the more interesting considering that free Cu is able to generate ROS much faster than AβCu. We rationalised this by explaining that even though AβCu will be generating ROS more slowly, because the complex can insert itself into the membrane, the ROS that is generated is best placed for localised lipid peroxidation.

It would be interesting to confirm our localisation argument, perhaps by monitoring formation of solution ROS via coumarin-3-carboxylic acid (3-CCA) for example. If our argument is correct, free Cu would show a higher signal using 3-CCA compared with AβCu bound to the membrane, while the membrane specific probe would show the opposite.

Attempts at observing AβCu ROS generation in a SUV system composed of the lipid DLPC were unsuccessful. This was explained by the Aβ not being able to bind to the membrane. DLPC was chosen as it is a completely saturated lipid that is in the fluid phase at room temperature. For DLPC it has not been explicitly shown in the literature that Aβ can or cannot bind to SUVs composed of this lipid. To overcome this, one could reconstitute the Aβ peptide into the lipid mixture as the vesicles are formed, or alternatively use SUVs composed of lipids where the Aβ K_d is known.

It should be noted that over the time course of the AβCu lipid peroxidation experiments ($\sim$2 h), the AβCu complex would be undergoing multiple turnovers. It is therefore possible that the Aβ peptide itself is being damaged as well as the lipid. It would be interesting to know how the Aβ species has changed over the course of the experiment, for example, has the Cu binding site been compromised or enhanced, has the peptide oligomerised or become cross linked? It may be possible to address some of these questions through the use of mass spectrometry.

Apolipoprotein E

A method for the introduction of a fluorophore to apoE has been reported. The main criterion for the labelling approach, was to minimise any perturbation to the protein's

structure and function. While methods for the introduction of a fluorophore to apoE have been reported, I contend that these methods (which require mutation of the (crucial) Cys112, or the creation of large fluorescent fusion proteins), are not likely to be representative of the wild-type structure. The method reported in this thesis involves the selective, enzymatic addition of a fluorescent label to the N-terminus. This method therefore avoids the potential problems of previously reported methods. Labelling efficacies >90 % were achieved.

It would also be of use to have a doubly fluorescent labelled apoE peptide. The sortase enzyme used is capable of introducing labels at either the N- or C-terminus of a protein. It has been reported that by using orthogonal sortase enzymes, distinct fluorophores can be added to each end of a protein. This approach however, was not explored in this thesis.

As apoE is a lipoprotein its influence on lipid peroxidation was also explored. ApoE was shown to have antioxidant effects, reducing the damage to lipid membranes caused by AβCu, as well as other oxidants. Interestingly, the antioxidant effect was shown to be isoform specific, with apoE3 being more protective than apoE4.

What this means for Alzheimer's disease

Combining the research presented in this thesis with the prior research in this field suggests that the metals hypothesis of AD cannot be ignored. Using disease prone Aβ mutants, evidence was presented linking altered copper assisted dimerisation kinetics with the disease. The kinetics of redox cycling of the AβCu complex was measured and shown not to be unfeasible within a biological system, although it will be a very slow process. The damage to lipid membranes by such AβCu redox cycling was shown to be very efficient, and links were drawn between the biggest genetic risk factor for AD (apoE), and ROS generation.

Bibliography

[1] A Alzhelmer. Uber eine eigenartige erkrankung der hirnrinde. *Allg. Z. Psychiatr.*, 64:146–148, 1907.

[2] Martin Strassnig and Mary Ganguli. About a peculiar disease of the cerebral cortex: Alzheimer's original case revisited. *Psychiatry (Edgmont)*, 2(9):30, 2005.

[3] Mary E Tinetti, Gail J McAvay, Terrence E Murphy, Cary P Gross, Haiqun Lin, and Heather G Allore. Contribution of individual diseases to death in older adults with multiple diseases. *Journal of the American Geriatrics Society*, 60(8):1448–1456, 2012.

[4] Alison Abbott. A problem for our age. *Nature*, 475(7355):S2, 2011.

[5] Eric Karran, Marc Mercken, and Bart De Strooper. The amyloid cascade hypothesis for alzheimer's disease: an appraisal for the development of therapeutics. *Nature reviews Drug discovery*, 10(9):698, 2011.

[6] Martin Prince. World alzheimer report 2016. *Alzheimer's Disease International*, 2016.

[7] Alzheimer's Association et al. 2018 alzheimer's disease facts and figures. *Alzheimer's & Dementia*, 14(3):367–429, 2018.

[8] John A Hardy and Gerald A Higgins. Alzheimer's disease: the amyloid cascade hypothesis. *Science*, 256(5054):184, 1992.

[9] Gary P Morris, Ian A Clark, and Bryce Vissel. Inconsistencies and controversies surrounding the amyloid hypothesis of alzheimer's disease. *Acta neuropathologica communications*, 2(1):135, 2014.

[10] Sergio T Ferreira and William L Klein. The aβ oligomer hypothesis for synapse failure and memory loss in alzheimer's disease. *Neurobiology of learning and memory*, 96(4):529–543, 2011.

[11] John Hardy. Alzheimer's disease: the amyloid cascade hypothesis: an update and reappraisal. *Journal of Alzheimer's disease*, 9(s3):151–153, 2006.

[12] S Kawabata, GA Higgins, and JW Gordon. Alzheimer's retraction. *Nature*, 356(6364):23–23, 1992.

[13] Frank M LaFerla. Calcium dyshomeostasis and intracellular signalling in alzheimer's disease. *Nature Reviews Neuroscience*, 3(11):862, 2002.

[14] Nelson Arispe, Eduardo Rojas, and Harvey B Pollard. Alzheimer disease amyloid beta protein forms calcium channels in bilayer membranes: blockade by tromethamine and aluminum. *Proceedings of the National Academy of Sciences*, 90(2):567–571, 1993.

[15] Rakez Kayed, Yuri Sokolov, Brian Edmonds, Theresa M McIntire, Saskia C Milton, James E Hall, and Charles G Glabe. Permeabilization of lipid bilayers is a common conformation-dependent activity of soluble amyloid oligomers in protein misfolding diseases. *Journal of Biological Chemistry*, 279(45):46363–46366, 2004.

[16] Priyanka Narayan, Kristina A Ganzinger, James McColl, Laura Weimann, Sarah Meehan, Seema Qamar, John A Carver, Mark R Wilson, Peter St. George-Hyslop, Christopher M Dobson, et al. Single molecule characterization of the interactions between amyloid-β peptides and the membranes of hippocampal cells. *Journal of the American Chemical Society*, 135(4):1491–1498, 2013.

[17] Akihiko Takashima, Kaori Noguchi, Kazuki Sato, Toshimitsu Hoshino, and Kazutomo Imahori. Tau protein kinase i is essential for amyloid beta-protein-induced neurotoxicity. *Proceedings of the National Academy of Sciences*, 90(16):7789–7793, 1993.

[18] Priyanka Narayan, Kira M Holmström, Dong-Hyun Kim, Daniel J Whitcomb,

Mark R Wilson, Peter St. George-Hyslop, Nicholas W Wood, Christopher M Dobson, Kwangwook Cho, Andrey Y Abramov, et al. Rare individual amyloid-β oligomers act on astrocytes to initiate neuronal damage. *Biochemistry*, 53(15):2442–2453, 2014.

[19] C Cheignon, M Tomas, D Bonnefont-Rousselot, P Faller, Christelle Hureau, and F Collin. Oxidative stress and the amyloid beta peptide in alzheimer's disease. *Redox biology*, 14:450–464, 2018.

[20] Carlo Ballatore, Virginia M-Y Lee, and John Q Trojanowski. Tau-mediated neurodegeneration in alzheimer's disease and related disorders. *Nature Reviews Neuroscience*, 8(9):663, 2007.

[21] Lars M Ittner and Jürgen Götz. Amyloid-β and tau—a toxic pas de deux in alzheimer's disease. *Nature Reviews Neuroscience*, 12(2):67, 2011.

[22] Anthony WP Fitzpatrick, Benjamin Falcon, Shaoda He, Alexey G Murzin, Garib Murshudov, Holly J Garringer, R Anthony Crowther, Bernardino Ghetti, Michel Goedert, and Sjors HW Scheres. Cryo-em structures of tau filaments from alzheimer's disease. *Nature*, 547(7662):185, 2017.

[23] Sarah L Shammas, Gonzalo A Garcia, Satish Kumar, Magnus Kjaergaard, Mathew H Horrocks, Nadia Shivji, Eva Mandelkow, Tuomas PJ Knowles, Eckhard Mandelkow, and David Klenerman. A mechanistic model of tau amyloid aggregation based on direct observation of oligomers. *Nature communications*, 6:7025, 2015.

[24] Franziska Kundel, Liu Hong, Benjamin Falcon, William A McEwan, Thomas CT Michaels, Georg Meisl, Noemi Esteras, Andrey Y Abramov, Tuomas JP Knowles, Michel Goedert, and David Klenerman. Measurement of tau filament fragmentation provides insights into prion-like spreading. *ACS chemical neuroscience*, 2018.

[25] Christian Haass, Michael G Schlossmacher, Albert Y Hung, Carmen Vigo-Pelfrey, Angela Mellon, Beth L Ostaszewski, Ivan Lieberburg, Edward H Koo, Dale Schenk, David B Teplow, et al. Amyloid β-peptide is produced by cultured cells during normal metabolism. *Nature*, 359(6393):322, 1992.

[26] Hui Zheng, Minghao Jiang, Myrna E Trumbauer, Dalip JS Sirinathsinghji, Ruth Hopkins, David W Smith, Robert P Heavens, Gerard R Dawson, Susan Boyce, Michael W Conner, et al. β-amyloid precursor protein-deficient mice show reactive gliosis and decreased locomotor activity. *Cell*, 81(4):525–531, 1995.

[27] Yann Senechal, Peter H Kelly, and Kumlesh K Dev. Amyloid precursor protein knockout mice show age-dependent deficits in passive avoidance learning. *Behavioural brain research*, 186(1):126–132, 2008.

[28] Maya A Koike, Alexander J Lin, Jonathan Pham, Elaine Nguyen, James J Yeh, Rombod Rahimian, Bruce J Tromberg, Bernard Choi, Kim N Green, and Frank M LaFerla. App knockout mice experience acute mortality as the result of ischemia. *PLoS One*, 7(8):e42665, 2012.

[29] Natalia N Nalivaeva and Anthony J Turner. The amyloid precursor protein: a biochemical enigma in brain development, function and disease. *FEBS letters*, 587(13):2046–2054, 2013.

[30] M Paul Murphy and Harry LeVine III. Alzheimer's disease and the amyloid-β peptide. *Journal of Alzheimer's Disease*, 19(1):311–323, 2010.

[31] Masha G Savelieff, Sanghyun Lee, Yuzhong Liu, and Mi Hee Lim. Untangling amyloid-β, tau, and metals in alzheimer's disease. *ACS chemical biology*, 8(5):856–865, 2013.

[32] David R Taylor and Nigel M Hooper. Role of lipid rafts in the processing of the pathogenic prion and alzheimer's amyloid-β proteins. In *Seminars in cell & developmental biology*, volume 18, pages 638–648. Elsevier, 2007.

[33] Jo V Rushworth and Nigel M Hooper. Lipid rafts: linking alzheimer's amyloid-β production, aggregation, and toxicity at neuronal membranes. *International journal of Alzheimer's disease*, 2011, 2011.

[34] David A Hicks, Natalia N Nalivaeva, and Anthony J Turner. Lipid rafts and alzheimer's disease: protein-lipid interactions and perturbation of signaling. *Frontiers in physiology*, 3:189, 2012.

[35] Lucie Kalvodova, Nicoletta Kahya, Petra Schwille, Robert Ehehalt, Paul Verkade, David Drechsel, and Kai Simons. Lipids as modulators of proteolytic activity of bace involvement of cholesterol, glycosphingolipids, and anionic phospholipids in vitro. *Journal of Biological Chemistry*, 280(44):36815–36823, 2005.

[36] Joanna M Cordy, Ishrut Hussain, Colin Dingwall, Nigel M Hooper, and Anthony J Turner. Exclusively targeting β-secretase to lipid rafts by gpi-anchor addition up-regulates β-site processing of the amyloid precursor protein. *Proceedings of the National Academy of Sciences*, 100(20):11735–11740, 2003.

[37] Han Tun, Laura Marlow, Inga Pinnix, Rachel Kinsey, and Kumar Sambamurti. Lipid rafts play an important role in aβ biogenesis by regulating the β-secretase pathway. *Journal of Molecular Neuroscience*, 19(1-2):31–35, 2002.

[38] Jo V Rushworth and Nigel M Hooper. Lipid rafts: linking alzheimer's amyloid-β production, aggregation, and toxicity at neuronal membranes. *International journal of Alzheimer's disease*, 2010.

[39] Yan-Jiang Wang, Hua-Dong Zhou, and Xin-Fu Zhou. Clearance of amyloid-beta in alzheimer's disease: progress, problems and perspectives. *Drug discovery today*, 11(19-20):931–938, 2006.

[40] Kristin R Wildsmith, Monica Holley, Julie C Savage, Rebecca Skerrett, and Gary E Landreth. Evidence for impaired amyloid β clearance in alzheimer's disease. *Alzheimer's research & therapy*, 5(4):33, 2013.

[41] Rashid Deane, Zhenhua Wu, Abhay Sagare, Judianne Davis, Shi Du Yan, Katie Hamm, Feng Xu, Margaret Parisi, Barbra LaRue, Hong Wei Hu, et al. Lrp/amyloid β-peptide interaction mediates differential brain efflux of aβ isoforms. *Neuron*, 43(3):333–344, 2004.

[42] Axel Montagne, Zhen Zhao, and Berislav V Zlokovic. Alzheimer's disease: A matter of blood–brain barrier dysfunction? *Journal of Experimental Medicine*, 214(11):3151–3169, 2017.

[43] Mélanie Carpentier, Yves Robitaille, Luc DesGroseillers, Guy Boileau, and Mieczyslaw Marcinkiewicz. Declining expression of neprilysin in alzheimer disease vasculature: possible involvement in cerebral amyloid angiopathy. *Journal of Neuropathology & Experimental Neurology*, 61(10):849–856, 2002.

[44] Wesley Farris, Stefan Mansourian, Yang Chang, Loren Lindsley, Elizabeth A Eckman, Matthew P Frosch, Christopher B Eckman, Rudolph E Tanzi, Dennis J Selkoe, and Suzanne Guénette. Insulin-degrading enzyme regulates the levels of insulin, amyloid β-protein, and the β-amyloid precursor protein intracellular domain in vivo. *Proceedings of the National Academy of Sciences*, 100(7):4162–4167, 2003.

[45] Christiane Reitz and Richard Mayeux. Alzheimer disease: epidemiology, diagnostic criteria, risk factors and biomarkers. *Biochemical pharmacology*, 88(4):640–651, 2014.

[46] Celeste M Karch and Alison M Goate. Alzheimer's disease risk genes and mechanisms of disease pathogenesis. *Biological psychiatry*, 77(1):43–51, 2015.

[47] Sascha Weggen and Dirk Beher. Molecular consequences of amyloid precursor protein and presenilin mutations causing autosomal-dominant alzheimer's disease. *Alzheimer's research & therapy*, 4(2):9, 2012.

[48] Lars Bertram and Rudolph E Tanzi. Thirty years of alzheimer's disease genetics: the implications of systematic meta-analyses. *Nature Reviews Neuroscience*, 9(10):768, 2008.

[49] Jeffrey Cummings, Garam Lee, Aaron Ritter, and Kate Zhong. Alzheimer's disease drug development pipeline: 2018. *Alzheimer's & Dementia: Translational Research & Clinical Interventions*, 2018.

[50] Michael A Castello, John David Jeppson, and Salvador Soriano. Moving beyond anti-amyloid therapy for the prevention and treatment of alzheimer's disease. *BMC neurology*, 14(1):169, 2014.

[51] Ezio Giacobini and Gabriel Gold. Alzheimer disease therapy—moving from amyloid-β to tau. *Nature Reviews Neurology*, 9(12):677, 2013.

[52] Simon C Drew. The case for abandoning therapeutic chelation of copper ions in alzheimer's disease. *Frontiers in neuroscience*, 11:317, 2017.

[53] Rosanna Squitti, Carlo Salustri, Mauro Rongioletti, and Mariacristina Siotto. Commentary: the case for abandoning therapeutic chelation of copper ions in alzheimer's disease. *Frontiers in neurology*, 8:503, 2017.

[54] Joseph R. Lakowicz. *Principles of Fluorescence Spectroscopy*. Springer, third edition, 2006.

[55] Petra Schwille. Fluorescence correlation spectroscopy. In *Encyclopedic Reference of Genomics and Proteomics in Molecular Medicine*, pages 576–578. Springer, 2005.

[56] Francisco Molina-Holgado, Robert C Hider, Alessandra Gaeta, Robert Williams, and Paul Francis. Metals ions and neurodegeneration. *Biometals*, 20(3-4):639–654, 2007.

[57] Masha G Savelieff, Sanghyun Lee, Yuzhong Liu, and Mi Hee Lim. Untangling amyloid-β, tau, and metals in alzheimer's disease. *ACS chemical biology*, 8(5):856–865, 2013.

[58] Harry Levine. Thioflavine t interaction with synthetic alzheimer's disease β-amyloid peptides: Detection of amyloid aggregation in solution. *Protein Science*, 2(3):404–410, 1993.

[59] Matthew Biancalana and Shohei Koide. Molecular mechanism of thioflavin-t binding to amyloid fibrils. *Biochimica et Biophysica Acta (BBA)-Proteins and Proteomics*, 1804(7):1405–1412, 2010.

[60] Paolo Arosio, Tuomas PJ Knowles, and Sara Linse. On the lag phase in amyloid fibril formation. *Physical Chemistry Chemical Physics*, 17(12):7606–7618, 2015.

[61] Samuel IA Cohen, Sara Linse, Leila M Luheshi, Erik Hellstrand, Duncan A White, Luke Rajah, Daniel E Otzen, Michele Vendruscolo, Christopher M Dobson, and Tuomas PJ Knowles. Proliferation of amyloid-β42 aggregates occurs through a secondary nucleation mechanism. *Proceedings of the National Academy of Sciences*, 110(24):9758–9763, 2013.

[62] Rafaa Zeineddine and Justin J Yerbury. The role of macropinocytosis in the propagation of protein aggregation associated with neurodegenerative diseases. *Frontiers in physiology*, 6:277, 2015.

[63] Kanchan Garai and Carl Frieden. Quantitative analysis of the time course of aβ oligomerization and subsequent growth steps using tetramethylrhodamine-labeled aβ. *Proceedings of the National Academy of Sciences*, 110(9):3321–3326, 2013.

[64] Thomas Branch, Paul Girvan, Mauricio Barahona, and Liming Ying. Introduction of a fluorescent probe to amyloid-β to reveal kinetic insights into its interactions with copper (ii). *Angewandte Chemie International Edition*, 54(4):1227–1230, 2015.

[65] Zhiguang Xiao and Anthony G Wedd. The challenges of determining metal–protein affinities. *Natural product reports*, 27(5):768–789, 2010.

[66] Elena Gaggelli, Henryk Kozlowski, Daniela Valensin, and Gianni Valensin. Copper homeostasis and neurodegenerative disorders (alzheimer's, prion, and parkinson's diseases and amyotrophic lateral sclerosis). *Chemical reviews*, 106(6):1995–2044, 2006.

[67] Pierre Dorlet, Serge Gambarelli, Peter Faller, and Christelle Hureau. Pulse epr spectroscopy reveals the coordination sphere of copper (ii) ions in the 1–16 amyloid-β peptide: A key role of the first two n-terminus residues. *Angewandte Chemie*, 121(49):9437–9440, 2009.

[68] Peter Faller and Christelle Hureau. Bioinorganic chemistry of copper and zinc ions coordinated to amyloid-β peptide. *Dalton Transactions*, pages 1080–1094, 2009.

[69] Amandine Conte-Daban, Valentina Borghesani, Stéphanie Sayen, Emmanuel Guillon, Yves Journaux, Geoffrey Gontard, Laurent Lisnard, and Christelle Hureau. Link between affinity and cu (ii) binding sites to amyloid-β peptides evaluated by a new water-soluble uv–visible ratiometric dye with a moderate cu (ii) affinity. *Analytical chemistry*, 89(3):2155–2162, 2017.

[70] Simona Catalani, Matteo Paganelli, Maria Enrica Gilberti, Luca Rozzini, Francesco Lanfranchi, Alessandro Padovani, and Pietro Apostoli. Free copper in serum: An analytical challenge and its possible applications. *Journal of Trace Elements in Medicine and Biology*, 45:176–180, 2018.

[71] David L Huffman and Thomas V O'Halloran. Function, structure, and mechanism of intracellular copper trafficking proteins. *Annual review of biochemistry*, 70(1):677–701, 2001.

[72] Mario Manto. Abnormal copper homeostasis: mechanisms and roles in neurodegeneration. *Toxics*, 2(2):327–345, 2014.

[73] Alexander Hopt, Stefan Korte, Herbert Fink, Ulrich Panne, Reinhard Niessner, Reinhard Jahn, Hans Kretzschmar, and Jochen Herms. Methods for studying synaptosomal copper release. *Journal of neuroscience methods*, 128(1-2):159–172, 2003.

[74] Sanah Sadiq, Zena Ghazala, Arnab Chowdhury, and Dietrich Büsselberg. Metal toxicity at the synapse: presynaptic, postsynaptic, and long-term effects. *Journal of toxicology*, 2012, 2012.

[75] Hélène Eury, Christian Bijani, Peter Faller, and Christelle Hureau. Copper (ii) coordination to amyloid β: murine versus human peptide. *Angewandte Chemie International Edition*, 50(4):901–905, 2011.

[76] Sergey Vyazovkin. On the phenomenon of variable activation energy for condensed phase reactions. *New Journal of Chemistry*, 24(11):913–917, 2000.

[77] JC Janssen, JA Beck, TA Campbell, A Dickinson, NC Fox, RJ Harvey, H Houlden, MN Rossor, and J Collinge. Early onset familial alzheimer's disease mutation frequency in 31 families. *Neurology*, 60(2):235–239, 2003.

[78] Y Wakutani, K Watanabe, Y Adachi, K Wada-Isoe, K Urakami, H Ninomiya, TC Saido, T Hashimoto, T Iwatsubo, and K Nakashima. Novel amyloid precursor protein gene missense mutation (d678n) in probable familial alzheimer's disease. *Journal of Neurology, Neurosurgery & Psychiatry*, 75(7):1039–1042, 2004.

[79] Yukiko Hori, Tadafumi Hashimoto, Yosuke Wakutani, Katsuya Urakami, Kenji Nakashima, Margaret M Condron, Satoshi Tsubuki, Takaomi C Saido, David B Teplow, and Takeshi Iwatsubo. The tottori (d7n) and english (h6r) familial alzheimer disease mutations accelerate aβ fibril formation without increasing protofibril formation. *Journal of biological chemistry*, 282(7):4916–4923, 2007.

[80] Kenjiro Ono, Margaret M Condron, and David B Teplow. Effects of the english (h6r) and tottori (d7n) familial alzheimer disease mutations on amyloid β-protein assembly and toxicity. *Journal of Biological Chemistry*, 285(30):23186–23197, 2010.

[81] Megan Murray Gessel, Summer Bernstein, Martin Kemper, David B Teplow, and Michael T Bowers. Familial alzheimer's disease mutations differentially alter amyloid β-protein oligomerization. *ACS chemical neuroscience*, 3(11):909–918, 2012.

[82] Man Hoang Viet, Phuong H Nguyen, Philippe Derreumaux, and Mai Suan Li. Effect of the english familial disease mutation (h6r) on the monomers and dimers of aβ40 and aβ42. *ACS chemical neuroscience*, 5(8):646–657, 2014.

[83] Man Hoang Viet, Phuong H Nguyen, Son Tung Ngo, Mai Suan Li, and Philippe Derreumaux. Effect of the tottori familial disease mutation (d7n) on the monomers and dimers of aβ40 and aβ42. *ACS chemical neuroscience*, 4(11):1446–1457, 2013.

[84] Liang Xu, Yonggang Chen, and Xiaojuan Wang. Dual effects of familial alzheimer's disease mutations (d7h, d7n, and h6r) on amyloid β peptide: Correlation dynamics and zinc binding. *Proteins: Structure, Function, and Bioinformatics*, 82(12):3286–3297, 2014.

[85] Bruno Alies, Hélene Eury, Christian Bijani, Lionel Rechignat, Peter Faller, and Christelle Hureau. ph-dependent cu (ii) coordination to amyloid-β peptide: impact of sequence alterations, including the h6r and d7n familial mutations. *Inorganic chemistry*, 50(21):11192–11201, 2011.

[86] Thomas Branch. *Fluorescence Studies of the Interactions of Amyloid-β with Metal Ions and Lipids*. PhD thesis, Imperial College London, 2015.

[87] Brian A Gordon, Tyler M Blazey, Yi Su, Amrita Hari-Raj, Aylin Dincer, Shaney Flores, Jon Christensen, Eric McDade, Guoqiao Wang, Chengjie Xiong, et al. Spatial patterns of neuroimaging biomarker change in individuals from families with autosomal dominant alzheimer's disease: a longitudinal study. *The Lancet Neurology*, 17(3):241–250, 2018.

[88] Jeppe T Pedersen, Kaare Teilum, Niels HH Heegaard, Jesper Østergaard, Hans-Werner Adolph, and Lars Hemmingsen. Rapid formation of a preoligomeric peptide–metal–peptide complex following copper (ii) binding to amyloid β peptides. *Angewandte Chemie International Edition*, 50(11):2532–2535, 2011.

[89] Jeppe T Pedersen, Christian B Borg, Thomas CT Michaels, Tuomas PJ Knowles, Peter Faller, Kaare Teilum, and Lars Hemmingsen. Aggregation-prone amyloid-β cuii species formed on the millisecond timescale under mildly acidic conditions. *ChemBioChem*, 16(9):1293–1297, 2015.

[90] Peter Faller. Copper and zinc binding to amyloid-β: Coordination, dynamics, aggregation, reactivity and metal-ion transfer. *ChemBioChem*, 10(18):2837–2845, 2009.

[91] Francis Hane, Gary Tran, Simon J Attwood, and Zoya Leonenko. Cu2+ affects amyloid-β (1–42) aggregation by increasing peptide-peptide binding forces. *PloS one*, 8(3):e59005, 2013.

[92] Danielle G Smith, Roberto Cappai, and Kevin J Barnham. The redox chemistry of the alzheimer's disease amyloid β peptide. *Biochimica et Biophysica Acta (BBA)-Biomembranes*, 1768(8):1976–1990, 2007.

[93] Xudong Huang, Craig S Atwood, Mariana A Hartshorn, Gerd Multhaup, Lee E Goldstein, Richard C Scarpa, Math P Cuajungco, Danielle N Gray, James Lim, Robert D Moir, et al. The aβ peptide of alzheimer's disease directly produces hydrogen peroxide through metal ion reduction. *Biochemistry*, 38(24):7609–7616, 1999.

[94] Jason Shearer and Veronika A Szalai. The amyloid-β peptide of alzheimer's disease binds cui in a linear bis-his coordination environment: Insight into a possible neuroprotective mechanism for the amyloid-β peptide. *Journal of the American Chemical Society*, 130(52):17826–17835, 2008.

[95] Tessa R Young, Angie Kirchner, Anthony G Wedd, and Zhiguang Xiao. An integrated study of the affinities of the aβ16 peptide for cu (i) and cu (ii): implications for the catalytic production of reactive oxygen species. *Metallomics*, 6(3):505–517, 2014.

[96] Carlos Opazo, Xudong Huang, Robert A Cherny, Robert D Moir, Alex E Roher, Anthony R White, Roberto Cappai, Colin L Masters, Rudolph E Tanzi, Nibaldo C Inestrosa, et al. Metalloenzyme-like activity of alzheimer's disease β-amyloid cu-dependent catalytic conversion of dopamine, cholesterol, and biological reducing agents to neurotoxic h2o2. *Journal of Biological Chemistry*, 277(43):40302–40308, 2002.

[97] CD Smith, J Ml Carney, PE Starke-Reed, CN Oliver, ER Stadtman, RA Floyd, and WR Markesbery. Excess brain protein oxidation and enzyme dysfunction in normal aging and in alzheimer disease. *Proceedings of the National Academy of Sciences*, 88(23):10540–10543, 1991.

[98] D Allan Butterfield, Jennifer Drake, Chava Pocernich, and Alessandra Castegna. Evidence of oxidative damage in alzheimer's disease brain: central role for amyloid β-peptide. *Trends in molecular medicine*, 7(12):548–554, 2001.

[99] Jianquan Wang, William R Markesbery, and Mark A Lovell. Increased oxidative damage in nuclear and mitochondrial dna in mild cognitive impairment. *Journal of neurochemistry*, 96(3):825–832, 2006.

[100] Craig S Atwood, George Perry, Hong Zeng, Yoji Kato, Walton D Jones, Ke-Qing Ling, Xudong Huang, Robert D Moir, Dandan Wang, Lawrence M Sayre, et al. Copper mediates dityrosine cross-linking of alzheimer's amyloid-β. *Biochemistry*, 43(2):560–568, 2004.

[101] Youssra K Al-Hilaly, Thomas L Williams, Maris Stewart-Parker, Lenzie Ford, Eldhose Skaria, Michael Cole, William Grant Bucher, Kyle L Morris, Alaa Abdul Sada, Julian R Thorpe, et al. A central role for dityrosine crosslinking of amyloid-β in alzheimer's disease. *Acta neuropathologica communications*, 1(1):83, 2013.

[102] Aurelio Vazquez de la Torre, Marina Gay, Sílvia Vilaprinyó-Pascual, Roberta Mazzucato, Montserrat Serra-Batiste, Marta Vilaseca, and Natalia Carulla. Direct evidence of the presence of cross-linked aβ dimers in the brains of alzheimer's disease patients. *Analytical chemistry*, 2018.

[103] Jeppe T Pedersen, Serene W Chen, Christian B Borg, Samuel Ness, Justyna M Bahl, Niels HH Heegaard, Christopher M Dobson, Lars Hemmingsen, Nunilo Cremades, and Kaare Teilum. Amyloid-β and α-synuclein decrease the level of metal-catalyzed reactive oxygen species by radical scavenging and redox silencing. *Journal of the American Chemical Society*, 138(12):3966–3969, 2016.

[104] Nineveh Yako, Tessa R Young, Jade M Cottam Jones, Craig A Hutton, Anthony G Wedd, and Zhiguang Xiao. Copper binding and redox chemistry of the aβ16 peptide and its variants: insights into determinants of copper-dependent reactivity. *Metallomics*, 9(3):278–291, 2017.

[105] Paul Girvan, Toru Miyake, Xiangyu Teng, Thomas Branch, and Liming Ying. Kinetics of the interactions between copper and amyloid-β with fad mutations and phosphorylation at the n terminus. *ChemBioChem*, 17(18):1732–1737, 2016.

[106] Véronique Balland, Christelle Hureau, and Jean-Michel Savéant. Electrochemical and homogeneous electron transfers to the

alzheimer amyloid-β copper complex follow a preorganization mechanism. *Proceedings of the National Academy of Sciences*, 107(40):17113–17118, 2010.

[107] Sara Furlan, Christelle Hureau, Peter Faller, and Giovanni La Penna. Modeling copper binding to the amyloid-β peptide at different ph: toward a molecular mechanism for cu reduction. *The Journal of Physical Chemistry B*, 116(39):11899–11910, 2012.

[108] Laure-Estelle Cassagnes, Vincent Hervé, Françoise Nepveu, Christelle Hureau, Peter Faller, and Fabrice Collin. The catalytically active copper-amyloid-beta state: Coordination site responsible for reactive oxygen species production. *Angewandte Chemie International Edition*, 52(42):11110–11113, 2013.

[109] Clémence Cheignon, Megan Jones, Elena Atrián-Blasco, Isabelle Kieffer, Peter Faller, Fabrice Collin, and Christelle Hureau. Identification of key structural features of the elusive cu–aβ complex that generates ros in alzheimer's disease. *Chemical Science*, 2017.

[110] Kenneth A Johnson, Zachary B Simpson, and Thomas Blom. Global kinetic explorer: a new computer program for dynamic simulation and fitting of kinetic data. *Analytical biochemistry*, 387(1):20–29, 2009.

[111] Norma Pérez-Almeida, Melchor González-Dávila, J Magdalena Santana-Casiano, Aridane G González, and Miguel Suárez de Tangil. Oxidation of cu(i) in seawater at low oxygen concentrations. *Environmental science & technology*, 47(3):1239–1247, 2013.

[112] David D Boehr, Ruth Nussinov, and Peter E Wright. The role of dynamic conformational ensembles in biomolecular recognition. *Nature chemical biology*, 5(11):789–796, 2009.

[113] Margaret E Rice. Ascorbate regulation and its neuroprotective role in the brain. *Trends in neurosciences*, 23(5):209–216, 2000.

[114] Paul A Hyslop, Zhiyuan Zhang, Donavan V Pearson, and Lee A Phebus. Measurement of striatal h 2 o 2 by microdialysis following global forebrain ischemia and reperfusion in the rat: correlation with the cytotoxic potential of h 2 o 2 in vitro. *Brain research*, 671(2):181–186, 1995.

[115] Ana Gomes, Eduarda Fernandes, and José LFC Lima. Fluorescence probes used for detection of reactive oxygen species. *Journal of biochemical and biophysical methods*, 65(2-3):45–80, 2005.

[116] Luc Guilloreau, Sarah Combalbert, Alix Sournia-Saquet, Honoré Mazarguil, and Peter Faller. Redox chemistry of copper–amyloid-β: The generation of hydroxyl radical in the presence of ascorbate is linked to redox-potentials and aggregation state. *ChemBioChem*, 8(11):1317–1325, 2007.

[117] D Allan Butterfield, Alessandra Castegna, Christopher M Lauderback, and Jennifer Drake. Evidence that amyloid beta-peptide-induced lipid peroxidation and its sequelae in alzheimer's disease brain contribute to neuronal death. *Neurobiology of aging*, 23(5):655–664, 2002.

[118] Gregor PC Drummen, Lydia CM van Liebergen, Jos AF Op den Kamp, and Jan A Post. C11-bodipy581/591, an oxidation-sensitive fluorescent lipid peroxidation probe:(micro) spectroscopic characterization and validation of methodology. *Free Radical Biology and Medicine*, 33(4):473–490, 2002.

[119] Gregor PC Drummen, Barend M Gadella, Jan A Post, and Jos F Brouwers. Mass spectrometric characterization of the oxidation of the fluorescent lipid peroxidation reporter molecule c11-bodipy581/591. *Free Radical Biology and Medicine*, 36(12):1635–1644, 2004.

[120] Matthew L MacDonald, Ian VJ Murray, and Paul H Axelsen. Mass spectrometric analysis demonstrates that bodipy 581/591 c11 overestimates and inhibits oxidative lipid damage. *Free Radical Biology and Medicine*, 42(9):1392–1397, 2007.

[121] Atsuko Kakio, Sei-ichi Nishimoto, Katsuhiko Yanagisawa, Yasunori Kozutsumi, and Katsumi Matsuzaki. Cholesterol-dependent formation of gm1 ganglioside-bound amyloid β-protein, an endogenous seed for alzheimer amyloid. *Journal of Biological Chemistry*, 276(27):24985–24990, 2001.

[122] Atsuko Kakio, Sei-ichi Nishimoto, Katsuhiko Yanagisawa, Yasunori Kozutsumi, and Katsumi Matsuzaki. Interactions of amyloid β-protein with various gangliosides in raft-like membranes: importance of gm1 ganglioside-bound form as an endogenous

seed for alzheimer amyloid. *Biochemistry*, 41(23):7385–7390, 2002.

[123] William Curatolo. The physical properties of glycolipids. *Biochimica et Biophysica Acta (BBA)-Reviews on Biomembranes*, 906(2):111–136, 1987.

[124] Radek Šachl, Ilya Mikhalyov, Martin Hof, and Lennart BÅ Johansson. A comparative study on ganglioside micelles using electronic energy transfer, fluorescence correlation spectroscopy and light scattering techniques. *Physical Chemistry Chemical Physics*, 11(21):4335–4343, 2009.

[125] William Garzon-Rodriguez, Charles G Glabe, Witold K Surewicz, et al. Acceleration of amyloid fibril formation by specific binding of aβ-(1–40) peptide to ganglioside-containing membrane vesicles. *Journal of Biological Chemistry*, 272(37):22987–22990, 1997.

[126] Mike P Williamson, YU Suzuki, Nathan T Bourne, and Tetsuo Asakura. Binding of amyloid β-peptide to ganglioside micelles is dependent on histidine-13. *Biochemical Journal*, 397(3):483–490, 2006.

[127] D Allan Butterfield and Debra Boyd-Kimball. The critical role of methionine 35 in alzheimer's amyloid β-peptide (1–42)-induced oxidative stress and neurotoxicity. *Biochimica et Biophysica Acta (BBA)-Proteins and Proteomics*, 1703(2):149–156, 2005.

[128] Norbert Kučerka, Yufeng Liu, Nanjun Chu, Horia I Petrache, Stephanie Tristram-Nagle, and John F Nagle. Structure of fully hydrated fluid phase dmpc and dlpc lipid bilayers using x-ray scattering from oriented multilamellar arrays and from unilamellar vesicles. *Biophysical journal*, 88(4):2626–2637, 2005.

[129] Chia-Chen Liu, Takahisa Kanekiyo, Huaxi Xu, and Guojun Bu. Apolipoprotein e and alzheimer disease: risk, mechanisms and therapy. *Nature Reviews Neurology*, 9(2):106, 2013.

[130] RE Pitas, JK Boyles, SH Lee, D Hui, and KH Weisgraber. Lipoproteins and their receptors in the central nervous system. characterization of the lipoproteins in cerebrospinal fluid and identification of apolipoprotein b, e (ldl) receptors in the brain. *Journal of Biological Chemistry*, 262(29):14352–14360, 1987.

[131] Robert W Mahley, Karl H Weisgraber, and Yadong Huang. Apolipoprotein e: structure determines function, from atherosclerosis to alzheimer's disease to aids. *Journal of lipid research*, 50(Supplement):S183–S188, 2009.

[132] Jianglei Chen, Qianqian Li, and Jianjun Wang. Topology of human apolipoprotein e3 uniquely regulates its diverse biological functions. *Proceedings of the National Academy of Sciences*, 2011.

[133] Yonghong Zhang, Sheeja Vasudevan, Radiya Sojitrawala, Wentao Zhao, Chunxian Cui, Chao Xu, Daping Fan, Yvonne Newhouse, Reeny Balestra, W Gray Jerome, et al. A monomeric, biologically active, full-length human apolipoprotein e. *Biochemistry*, 46(37):10722–10732, 2007.

[134] Li-Ming Dong, Charles Wilson, Mark R Wardell, Trey Simmons, Robert W Mahley, Karl H Weisgraber, and David A Agard. Human apolipoprotein e. role of arginine 61 in mediating the lipoprotein preferences of the e3 and e4 isoforms. *Journal of Biological Chemistry*, 269(35):22358–22365, 1994.

[135] Li-Ming Dong and Karl H Weisgraber. Human apolipoprotein e4 domain interaction arginine 61 and glutamic acid 255 interact to direct the preference for very low density lipoproteins. *Journal of Biological Chemistry*, 271(32):19053–19057, 1996.

[136] Danny M Hatters, Madhu S Budamagunta, John C Voss, and Karl H Weisgraber. Modulation of apolipoprotein e structure by domain interaction differences in lipid-bound and lipid-free forms. *Journal of Biological Chemistry*, 280(40):34288–34295, 2005.

[137] Qin Xu, Walter J Brecht, Karl H Weisgraber, Robert W Mahley, and Yadong Huang. Apolipoprotein e4 domain interaction occurs in living neuronal cells as determined by fluorescence resonance energy transfer. *Journal of Biological Chemistry*, 279(24):25511–25516, 2004.

[138] Carl Frieden, Hanliu Wang, and Chris MW Ho. A mechanism for lipid binding to apoe and the role of intrinsically disordered regions coupled to domain–domain interactions. *Proceedings of the National Academy of Sciences*, 114(24):6292–6297, 2017.

[139] Palaniappan S Chetty, Leland Mayne, Sissel Lund-Katz, S Walter Englander, and

Michael C Phillips. Helical structure, stability, and dynamics in human apolipoprotein e3 and e4 by hydrogen exchange and mass spectrometry. *Proceedings of the National Academy of Sciences*, 114(5):968–973, 2017.

[140] Yoshio Namba, Masanori Tomonaga, Hiroshi Kawasaki, Eiichi Otomo, and Kazuhiko Ikeda. Apolipoprotein e immunoreactivity in cerebral amyloid deposits and neurofibrillary tangles in alzheimer's disease and kuru plaque amyloid in creutzfeldt-jakob disease. *Brain research*, 541(1):163–166, 1991.

[141] Jurgita Zekonyte, Kenji Sakai, James AR Nicoll, Roy O Weller, and Roxana O Carare. Quantification of molecular interactions between apoe, amyloid-beta (aβ) and laminin: relevance to accumulation of aβ in alzheimer's disease. *Biochimica et Biophysica Acta (BBA)-Molecular Basis of Disease*, 1862(5):1047–1053, 2016.

[142] Mary Jo LaDu, Michael T Falduto, Arlene M Manelli, Catherine A Reardon, Godfrey S Getz, and Donald E Frail. Isoform-specific binding of apolipoprotein e to beta-amyloid. *Journal of Biological Chemistry*, 269(38):23403–23406, 1994.

[143] Eleanna Kara, Jordan D Marks, Allyson D Roe, Caitlin Commins, Zhanyun Fan, Maria Calvo-Rodriguez, Susanne Wegmann, Eloise Hudry, and Bradley T Hyman. A flow cytometry–based in vitro assay reveals that formation of apolipoprotein e (apoe)–amyloid beta complexes depends on apoe isoform and cell type. *Journal of Biological Chemistry*, 293(34):13247–13256, 2018.

[144] Takahiko Tokuda, Miguel Calero, Etsuro Matsubara, Ruben Vidal, Asok Kumar, Bruno Permanne, Berislav Zlokovic, Jonathan D Smith, Mary Jo Ladu, Agueda Rostagno, et al. Lipidation of apolipoprotein e influences its isoform-specific interaction with alzheimer's amyloid β peptides. *Biochemical Journal*, 348(2):359–365, 2000.

[145] Joseph M Castellano, Jungsu Kim, Floy R Stewart, Hong Jiang, Ronald B DeMattos, Bruce W Patterson, Anne M Fagan, John C Morris, Kwasi G Mawuenyega, Carlos Cruchaga, et al. Human apoe isoforms differentially regulate brain amyloid-β peptide clearance. *Science translational medicine*, 3(89):89ra57–89ra57, 2011.

[146] Krista C Evans, Elizabeth P Berger, Cheon-Gyu Cho, Karl H Weisgraber, and Peter T Lansbury. Apolipoprotein e is a kinetic but not a thermodynamic inhibitor of amyloid formation: implications for the pathogenesis and treatment of alzheimer disease. *Proceedings of the National Academy of Sciences*, 92(3):763–767, 1995.

[147] Kanchan Garai, Philip B Verghese, Berevan Baban, David M Holtzman, and Carl Frieden. The binding of apolipoprotein e to oligomers and fibrils of amyloid-β alters the kinetics of amyloid aggregation. *Biochemistry*, 53(40):6323–6331, 2014.

[148] Philip B Verghese, Joseph M Castellano, Kanchan Garai, Yinong Wang, Hong Jiang, Aarti Shah, Guojun Bu, Carl Frieden, and David M Holtzman. Apoe influences amyloid-β (aβ) clearance despite minimal apoe/aβ association in physiological conditions. *Proceedings of the National Academy of Sciences*, page 201220484, 2013.

[149] Yadong Huang. Aβ-independent roles of apolipoprotein e4 in the pathogenesis of alzheimer's disease. *Trends in molecular medicine*, 16(6):287–294, 2010.

[150] Yadong Huang, Xiao Qin Liu, Tony Wyss-Coray, Walter J Brecht, David A Sanan, and Robert W Mahley. Apolipoprotein e fragments present in alzheimer's disease brains induce neurofibrillary tangle-like intracellular inclusions in neurons. *Proceedings of the National Academy of Sciences*, 98(15):8838–8843, 2001.

[151] Faith M Harris, Walter J Brecht, Qin Xu, Ina Tesseur, Lisa Kekonius, Tony Wyss-Coray, Jo Dee Fish, Eliezer Masliah, Paul C Hopkins, Kimberly Scearce-Levie, et al. Carboxyl-terminal-truncated apolipoprotein e4 causes alzheimer's disease-like neurodegeneration and behavioral deficits in transgenic mice. *Proceedings of the National Academy of Sciences*, 100(19):10966–10971, 2003.

[152] Isaac Veinbergs, Analisa Everson, Yutaka Sagara, and Eliezer Masliah. Neurotoxic effects of apolipoprotein e4 are mediated via dysregulation of calcium homeostasis. *Journal of neuroscience research*, 67(3):379–387, 2002.

[153] Stanley C Rall Jr, Karl H Weisgraber, and Robert W Mahley. [13] isolation and characterization of apolipoprotein e. In *Methods in enzymology*, volume 128, pages 273–287. Elsevier, 1986.

[154] Tikva Vogel, Karl H Weisgraber, Menachem I Zeevi, Hanna Ben-Artzi, Avigdor Z Levanon, Stanley C Rall, Thomas L Innerarity, David Y Hui, John M Taylor, and Dov Kanner. Human apolipoprotein e expression in escherichia coli: structural and functional identity of the bacterially produced protein with plasma apolipoprotein e. *Proceedings of the National Academy of Sciences*, 82(24):8696–8700, 1985.

[155] Tatsurou Shibui, Michiru Uchida-Kamizono, Hiroko Okazaki, Jun Kondo, Satoru Murayama, Yuuki Morimoto, Kenji Nagahari, and Yutaka Teranishi. High-level secretion of human apolipoprotein e produced in escherichia coli: use of a secretion plasmid containing tandemly polymerized ompf-hybrid gene. *Journal of biotechnology*, 17(2):109–120, 1991.

[156] Claude Monteilhet, Nicole Lachacinski, and Lawrence P Aggerbeck. Cytoplasmic and periplasmic production of human apolipoprotein e in escherichia coli using natural and bacterial signal peptides. *Gene*, 125(2):223–228, 1993.

[157] Thierry Pillot, Anne Barbier, Athanase Visvikis, Karine Lozac'h, Maryvonne Rosseneu, Joel Vandekerckhove, and Gérard Siest. Single-step purification of two functional human apolipoprotein e variants hyperexpressed inescherichia coli. *Protein expression and purification*, 7(4):407–414, 1996.

[158] Julie A Morrow, Kay S Arnold, and Karl H Weisgraber. Functional characterization of apolipoprotein e isoforms overexpressed in escherichia coli. *Protein expression and purification*, 16(2):224–230, 1999.

[159] Yvonne Newhouse and Karl H Weisgraber. Apolipoprotein e expression and purification. In *Alzheimer's Disease and Frontotemporal Dementia*, pages 127–140. Humana Press, Totowa, NJ, 2010.

[160] Letta Argyri, Vassiliki Skamnaki, Efstratios Stratikos, and Angeliki Chroni. A simple approach for human recombinant apolipoprotein e4 expression and purification. *Protein expression and purification*, 79(2):251–257, 2011.

[161] Letta Argyri, Ioannis Dafnis, Theodossis A Theodossiou, Donald Gantz, Efstratios Stratikos, and Angeliki Chroni. Molecular basis for increased risk for late-onset alzheimer disease due to the naturally occurring l28p mutation in apolipoprotein e4. *Journal of Biological Chemistry*, 289(18):12931–12945, 2014.

[162] Kanchan Garai and Carl Frieden. The association- dissociation behavior of the apoe proteins: Kinetic and equilibrium studies. *Biochemistry*, 49(44):9533–9541, 2010.

[163] Qiang Li and Stefan Seeger. Label-free detection of protein interactions using deep uv fluorescence lifetime microscopy. *Analytical biochemistry*, 367(1):104–110, 2007.

[164] Benjamin Schuler and Lewis K Pannell. Specific labeling of polypeptides at amino-terminal cysteine residues using cy5-benzyl thioester. *Bioconjugate chemistry*, 13(5):1039–1043, 2002.

[165] Sarkis K Mazmanian, Gwen Liu, Hung Ton-That, and Olaf Schneewind. Staphylococcus aureus sortase, an enzyme that anchors surface proteins to the cell wall. *Science*, 285(5428):760–763, 1999.

[166] Maximilian W Popp, John M Antos, Gijsbert M Grotenbreg, Eric Spooner, and Hidde L Ploegh. Sortagging: a versatile method for protein labeling. *Nature chemical biology*, 3(11):707, 2007.

[167] John M Antos, Guo-Liang Chew, Carla P Guimaraes, Nicholas C Yoder, Gijsbert M Grotenbreg, Maximilian Wei-Lin Popp, and Hidde L Ploegh. Site-specific n- and c-terminal labeling of a single polypeptide using sortases of different specificity. *Journal of the American Chemical Society*, 131(31):10800–10801, 2009.

[168] Carla P Guimaraes, Martin D Witte, Christopher S Theile, Gunes Bozkurt, Lenka Kundrat, Annet EM Blom, and Hidde L Ploegh. Site-specific c-terminal and internal loop labeling of proteins using sortase-mediated reactions. *Nature protocols*, 8(9):1787, 2013.

[169] Christopher S Theile, Martin D Witte, Annet EM Blom, Lenka Kundrat, Hidde L Ploegh, and Carla P Guimaraes. Site-specific n-terminal labeling of proteins using sortase-mediated reactions. *Nature protocols*, 8(9):1800, 2013.

[170] G Chi Chen, Luke SS Guo, Robert L Hamilton, Virginia Gordon, E Glen Richards, and John P Kane. Circular dichroic spectra of apolipoprotein e in

model complexes and cholesterol-rich lipoproteins: lipid contribution. *Biochemistry*, 23(26):6530–6538, 1984.

[171] Julie A Morrow, Mark L Segall, Sissel Lund-Katz, Michael C Phillips, Mark Knapp, Bernhard Rupp, and Karl H Weisgraber. Differences in stability among the human apolipoprotein e isoforms determined by the amino-terminal domain. *Biochemistry*, 39(38):11657–11666, 2000.

[172] Kanchan Garai, Berevan Baban, and Carl Frieden. Dissociation of apolipoprotein e oligomers to monomer is required for high-affinity binding to phospholipid vesicles. *Biochemistry*, 50(13):2550–2558, 2011.

[173] Milla Koistinaho, Suizhen Lin, XIN Wu, Michail Esterman, Deanna Koger, Jeffrey Hanson, Richard Higgs, Feng Liu, Seema Malkani, Kelly R Bales, et al. Apolipoprotein e promotes astrocyte colocalization and degradation of deposited amyloid-β peptides. *Nature medicine*, 10(7):719, 2004.

[174] Paula G Ulery, Jeanette Beers, Irina Mikhailenko, Rudolph E Tanzi, G William Rebeck, Bradley T Hyman, and Dudley K Strickland. Modulation of β-amyloid precursor protein processing by the low density lipoprotein receptor-related protein (lrp) evidence that lrp contributes to the pathogenesis of alzheimer's disease. *Journal of Biological Chemistry*, 275(10):7410–7415, 2000.

[175] Sonny Ly, Robin Altman, Jitka Petrlova, Yu Lin, Silvia Hilt, Thomas Huser, Ted A Laurence, and John C Voss. Binding of apolipoprotein e inhibits the oligomer growth of amyloid-β peptide in solution as determined by fluorescence cross-correlation spectroscopy. *Journal of Biological Chemistry*, 288(17):11628–11635, 2013.

[176] Robert D Moir, Craig S Atwood, Donna M Romano, Maxwell H Laurans, Xudong Huang, Ashley I Bush, Jonathan D Smith, and Rudolph E Tanzi. Differential effects of apolipoprotein e isoforms on metal-induced aggregation of aβ using physiological concentrations. *Biochemistry*, 38(14):4595–4603, 1999.

[177] Tony Hayek, Judith Oiknine, J Gerald Brook, and Michael Aviram. Increased plasma and lipoprotein lipid peroxidation in apo e-deficient mice. *Biochemical and biophysical research communications*, 201(3):1567–1574, 1994.

[178] Masaaki Miyata and Jonathan D Smith. Apolipoprotein e allele–specific antioxidant activity and effects on cytotoxicity by oxidative insults and β–amyloid peptides. *Nature genetics*, 14(1):55, 1996.

[179] Thomas Pham, Ahmer Kodvawala, and David Y Hui. The receptor binding domain of apolipoprotein e is responsible for its antioxidant activity. *Biochemistry*, 44(20):7577–7582, 2005.

[180] Ward A Pedersen, Sic L Chan, and Mark P Mattson. A mechanism for the neuroprotective effect of apolipoprotein e: isoform-specific modification by the lipid peroxidation product 4-hydroxynonenal. *Journal of neurochemistry*, 74(4):1426–1433, 2000.

[181] Suchitra Mitra, Pallavi Prasad, and Saumen Chakraborty. A unified view of assessing the pro-oxidant vs antioxidant nature of amyloid beta conformers. *ChemBioChem*, 2018. Accepted Article.

Appendices

Appendix A

Copyright Permission Documents

Fig. 1.1 [5]

License Number	4422570743065
License date	Sep 05, 2018
Licensed Content Publisher	LicSpringer Nature
Licensed Content Publication	Nature Reviews Drug Discovery
Licensed Content Title	The amyloid cascade hypothesis for Alzheimer's disease: an appraisal for the development of therapeutics
Licensed Content Author	Eric Karran, Marc Mercken, Bart De Strooper
Licensed Content Date	Aug 19, 2011
Licensed Content Volume	10
Licensed Content Issue	9
Type of Use	Thesis/Dissertation
Requestor type	academic/university or research institute
Format	print and electronic
Portion	figures/tables/illustrations
Number of figures/tables/illustrations	1
High-res required	no
Will you be translating?	no
Circulation/distribution	<501
Author of this Springer Nature content	no
Title	Reactive oxygen species in Alzheimer's disease: studies of amyloid beta-copper and apolipoprotein E
Instructor name	n/a
Institution name	n/a
Expected presentation date	Sep-18
Portions	Figure 1
Requestor Location	Mr. Paul Girvan 133 Murray Road London, W5 4DD United Kingdom Attn: Mr. Paul Gi rvan
Billing Type	Invoice
Billing Address	Mr. Paul Girvan 133 Murray Road London, United Kingdom W5 4DD Attn: Mr. Paul Girvan
Total	0.00 USD

Fig. 1.4[31]

8/21/2018 Rightslink® by Copyright Clearance Center

Copyright Clearance Center RightsLink® Home Account Info Help

ACS Publications Most Trusted. Most Cited. Most Read.

Title: Untangling Amyloid-β, Tau, and Metals in Alzheimer's Disease
Author: Masha G. Savelieff, Sanghyun Lee, Yuzhong Liu, et al
Publication: ACS Chemical Biology
Publisher: American Chemical Society
Date: May 1, 2013
Copyright © 2013, American Chemical Society

Logged in as:
Paul Girvan
LOGOUT

PERMISSION/LICENSE IS GRANTED FOR YOUR ORDER AT NO CHARGE

This type of permission/license, instead of the standard Terms & Conditions, is sent to you because no fee is being charged for your order. Please note the following:

- Permission is granted for your request in both print and electronic formats, and translations.
- If figures and/or tables were requested, they may be adapted or used in part.
- Please print this page for your records and send a copy of it to your publisher/graduate school.
- Appropriate credit for the requested material should be given as follows: "Reprinted (adapted) with permission from (COMPLETE REFERENCE CITATION). Copyright (YEAR) American Chemical Society." Insert appropriate information in place of the capitalized words.
- One-time permission is granted only for the use specified in your request. No additional uses are granted (such as derivative works or other editions). For any other uses, please submit a new request.

If credit is given to another source for the material you requested, permission must be obtained from that source.

BACK CLOSE WINDOW

Copyright © 2018 Copyright Clearance Center, Inc. All Rights Reserved. Privacy statement. Terms and Conditions.
Comments? We would like to hear from you. E-mail us at customercare@copyright.com

https://s100.copyright.com/AppDispatchServlet 1/1

Fig. 1.5 [46]

License Number	4413590673856
License date	Aug 21, 2018
Licensed Content Publisher	Elseviere
Licensed Content Publication	Biological Psychiatry
Licensed Content Title	Alzheimer's Disease Risk Genes and Mechanisms of Disease Pathogenesis
Licensed Content Author	Celeste M. Karch,Alison M. Goate
Licensed Content Date	JJan 1, 2015
Licensed Content Volume	77
Licensed Content Issue	1
Type of Use	Thesis/Dissertation
Requestor type	academic/university or research institute
Portion	figures/tables/illustrations
Number of figures/tables/illustrations	1
Format	print and electronic
Author of this Elsevier article?	no
Will you be translating?	no
Original figure numbers	figure 1
Title	Reactive oxygen species in Alzheimer's disease: studies of amyloid beta-copper and apolipoprotein E
Expected completion date	Sep 2018
Estimated size	150
Requestor Location	Mr. Paul Girvan 133 Murray Road London, W5 4DD United Kingdom Attn: Mr. Paul Gi rvan
Pblisher Tax ID	GB 494 6272 12
Total	0.00 GBP

Fig. 6.1 [129]

License Number	4422571347268
License date	Sep 05, 2018
Licensed Content Publisher	Springer Nature
Licensed Content Publication	Nature Reviews Neurology
Licensed Content Title	Apolipoprotein E and Alzheimer disease: risk, mechanisms and therapy
Licensed Content Author	Chia-Chen Liu, Takahisa Kanekiyo, Huaxi Xu, Guojun Bu
Licensed Content Date	Jan 8, 2013
Licensed Content Volume	9
Licensed Content Issue	2
Type of Use	Thesis/Dissertation
Requestor type	academic/university or research institute
Format	print and electronic
Portion	figures/tables/illustrations
Number of figures/tables/illustrations	1
High-res required	no
Will you be translating?	no
Circulation/distribution	<501
Author of this Springer Nature content	no
Title	Reactive oxygen species in Alzheimer's disease: studies of amyloid beta-copper and apolipoprotein E
Instructor name	n/a
Institution name	n/a
Expected presentation date	Sep-18
Portions	Figure 1
Requestor Location	Mr. Paul Girvan 133 Murray Road London, W5 4DD United Kingdom Attn: Mr. Paul Gi rvan
Billing Type	Invoice
Billing Address	Mr. Paul Girvan 133 Murray Road London, United Kingdom W5 4DD Attn: Mr. Paul Girvan
Total	0.00 USD